The Moment Rotation Characteristics of Reinforced Concrete Beams. An application of the Photostress Technique.

J. C. Mamet

Department of Civil Engineering and Applied Mechanics.

Master of Engineering
September, 1968.

ABSTRACT

A computer program was developed in order to obtain the deflections and rotations of members up to ultimate load.

Further, a method of recording the fringe patterns in normal and oblique incidences by means of a large oblique incidence attachment was used with good success.

It is proposed that such a method can be used for the determination of strain patterns in reinforced concrete up to ultimate loads, provided that adequate optical equipment is developed.

Four prisms in axial compression, and four simply supported beams were tested, and the strains were measured by mechanical gauges as well as recorded from fringe patterns.

Good correlation was obtained.

J.C. MAMET
MOMENT ROTATION PROPERTIES OF
REINFORCED CONCRETE BEAMS

THE MOMENT ROTATION CHARACTERISTICS OF REINFORCED CONCRETE BEAMS•AN APPLICATION OF THE PHOTOSTRESS TECHNIQUE.

by

Jean C. Mamet

A thesis submitted to the Faculty of Graduate Studies and Research in partial fulfilment of the requirements for the degree of Master of Engineering.

Department of Civil Engineering
and Applied Mechanics.
McGill University, Montreal, Canada.

September 1968.

The Moment Rotation Characteristics of Reinforced Concrete Beams. An application of the Photostress Technique.

J. C. Mamet

Department of Civil Engineering and Applied Mechanics.

Master of Engineering
September, 1968.

ABSTRACT

A computer program was developed in order to obtain the deflections and rotations of members up to ultimate load.

Further, a method of recording the fringe patterns in normal and oblique incidences by means of a large oblique incidence attachment was used with good success.

It is proposed that such a method can be used for the determination of strain patterns in reinforced concrete up to ultimate loads, provided that adequate optical equipment is developed.

Four prisms in axial compression, and four simply supported beams were tested, and the strains were measured by mechanical gauges as well as recorded from fringe patterns.

Good correlation was obtained.

ACKNOWLEDGEMENTS

It is a pleasure to thank Professor B. Gersovitz for suggesting the lines of this investigation and for his continuous encouragements.

Thanks are also due to Professor J. O. McCutcheon, Chairman of the Department, for his valuable suggestions, and to various members of staff for their technical assistance.

The experimental work described herein was sponsored by the Emergency Measures Organization of Canada, and was carried out at McGill University.

TABLE OF CONTENTS

LIST OF FIGURES.

LIST OF TABLES.

Notation

Chapter I

C	stress optical coefficient.
E	Young's modulus of elasticity.
F	fringe value $(\lambda/2Ct)$
K	strain optical factor.
n_n	fringe order in normal incidence.
n_o	fringe order in oblique incidence.
R	reinforcing effect correction factor.
t	thickness of a birefringent coating.
Δ_n	angular relative retardation in normal incidence.
Δ_o	angular relative retardation in oblique incidence.
λ	wave length.
ν	Poisson's ratio.
σ_i	principal stress $(i = 1,2)$.
σ_x, σ_y	direct stresses.
σ_{xy}	shear stress.

CHAPTER II.

A_s	area of tension reinforcement.
A'_s	area of compression reinforcement
b	width of rectangular section
c	depth of neutral axis below extreme compressive fiber at ultimate
d	distance from extreme compressive fiber to centroid of tension reinforcement
d'	distance from extreme compressive fiber to centroid of compression reinforcement
E	modulus of elasticity
E_c	modulus of elasticity of concrete
E_s	modulus of elasticity of reinforcing steel
E'_s	modulus of strain hardening of reinforcing steel.
f_c	tensile strength of concrete
f'_c	compressive strength of concrete
f^*_c	actual stress in concrete at extreme tensile fiber
f'^*_c	actual stress in concrete at extreme compressive fiber
f'^{**}_c	actual stress in concrete at depth of centroid of compression reinforcement
f_o	datum stress defined in fig 2.5
f_s	stress in tension reinforcement
f'_s	stress in compression reinforcement
f_y	elastic limit of tension reinforcement
f'_y	elastic limit of compression reinforcement

h	total depth of rectangular cross section
I	moment of inertia
$j_s d$	distance between centroids of tension and compression reinforcements
$k\ d$	depth of neutral axis
k_1	ratio of average concrete compressive stress to maximum stress
k_2	ratio of depth of resultant of concrete compressive force, to depth of neutral axis
k_3	ratio of maximum compressive stress to compressive strength of concrete
$k_u d$	depth of neutral axis at ultimate
K_e	elastic flexural rigidity
K_p	plasticity factor
K'_p	plastic rigidity, or strain hardening coefficient
l	length of beam
l_p	length of plastic region at hinge
m	the ratio $\epsilon_u E_s / k_1 k_3 f'_c$
M	bending moment
M_u	ultimate bending moment
M_y	bending moment at yield of tension reinforcement
n	ratio of modulus of elasticity of steel to that of concrete E_s/E_c

p	percentage of tension reinforcement A_s/bd
p'	percentage of compression reinforcement A'_s/bd
p''	percentage of binding reinforcement
q	tension reinforcement index , pf_y/f'_c
q'	compression reinforcement index $p'f'_y/f'_c$
q_b	tension reinforcement index for balanced conditions
q_{sh}	tension reinforcement index, at commencement of strain hardening
R	radius of curvature
U	strain energy
v	distance from neutral axis to extreme fiber
x	abscissa
y	vertical deflection
z	distance from cross section to nearest point of inflexion
α	integer
δ	the ratio h/d
ϵ	strain
ϵ'_c	compressive strain at extreme fiber of concrete
ϵ'_{cy}	same, at commencement of yield
ϵ_s	steel strain
ϵ_y	steel strain at commencement of yield
ϵ_u	steel strain at ultimate
Φ	total rotation occurring over the length of a plastic region

Φ_e	elastic rotation occurring over the length of a plastic region
Φ_u	total rotation at ultimate, over the length of a plastic region
Φ_y	elastic rotation at commencement of yield, over the length of a plastic hinge
ψ	curvature
ψ_p	curvature in the plastic range of reformations;
ψ_u	curvature at ultimate
ψ_y	curvature at commencement of yield
σ	stress
θ	inelastic rotation over the length of a plastic region;
θ_u	inelastic rotation at ultimate over the length of a plastic region
θ_{tu}	total rotation at ultimate, occurring between the section of maximum-moment, and an adjacent section of zero moment.

Introduction.

In 1967, the author was asked to investigate the possibility of using the photoelastic coating technique to determine the strain distribution in the hinging region of a reinforced concrete member, up to failure.

This implied the development of a photographic technique that would provide an almost instantaneous record of the strain pattern, in order to suppress the effect of creep in concrete.

Although stress and strain distribution in concrete at ultimate has been the object of numerous tests and experiments during the last twenty-five years, most of the measurements were carried out with mechanical extensometers and electrical strain gauges.

To the knowledge of the author, it is the first time that photoelastic coatings are used for this purpose. As such, the present work belongs to two distinct disciplines of the Engineering Science: photoelasticity, and theory of reinforced concrete.

Photoelasticity stems from the discovery of artificial birefringence by Brewster in 1816.

Further pioneer work in this field was done by Coker and Filon in England, at the turn of this century.

In 1930, in France, Mesnager proposed that birefringent coatings might be used to determine strain distributions in situ, but like Brewster, he was unable to develop a technique, due to a lack of suitable available materials.

Using Mesnager's ideas, Zandman developed the method at Paris University in 1956; it was later brought into commercial use in the United States of America, under the trade name "Photostress."

This method has already been used in a wide range of problems; records of its application to concrete, however, are scarce.

Stephen and Priz [Ref 1.14] used birefringent coatings to study the stress distribution in mortar prisms around metal instrusions; Dantu [Ref 1.12] investigated stress concentrations around aggregates in concrete.

In April 1967, Abeles presented a paper at the annual meeting of the American Concrete Institute, held in Toronto, in which he showed strain distribution in prestressed beams.

For concrete there is little need to recall the fundamental work of Considere, Freyssinet, Maillart and von Emperger, done at the beginning of this century.

The elastic theory prevailed, but work continued on the inelastic distribution of bending stresses in reinforced concrete members.

In the nineteen thirties, Brandtzaeg, Stüssi and later Whitney proposed several shapes of stress blocks; however it was not until after the Second World War that, due to the shortage of building materials in Europe, further progress was made in the methods of limit design for frames.

The problem of the rotation capacity of reinforced concrete sections then became of paramount importance, and was studied by such eminent researchers as A.L.L.Baker, Chambaud, Macchi and Rüsch.

In 1956, an international research programme on moment-rotation characteristics was evolved, in which fourteen laboratories took part, under the auspices of the Comité Européen du Béton.

Of particular interest is the work carried on since then at The Imperial College of Technology in London by Baker and his

disciples, Amarakone, Barnard, Chan, Corley, Mattock, etc.

The importance of the subject was confirmed by the joint organization, under the auspices of the American Concrete Institute, and the American Society of Civil Engineers, of an International Symposium on the Flexural Mechanics of Reinforced Concrete, held at Miami in 1964.

Chapter I.

Photoelasticity - The Photostress technique.

1.1 Introduction.

Photoelasticity is a well established technique. Numerous treatises on the subject have been written, where such topics as "stresses and strains at a point, properties of light propagation, natural and artificial birefringence" are developed in detail.

The reader is invited to consult [Refs. 1.1 to 1.9] for further reference.

The equations and the mechanism of the propagation of light through a polariscope are also well known, and so are the techniques of compensation and separation of the principal stresses at a point.

1.2 The Photostress Technique.

The Photoelastic techniques call for the manufacture of plastic models, geometrically similar to parts under investigation, stressed like them and placed in the path of a beam of polarized light.

The Photostress technique, on the contrary, calls for the coating of the workpiece with a thin sheet of birefringent plastic, glued to it so that the strains at the interface be identical in both materials.

Stresses are thus developed in the plastic, that make it optically anistropic.

Provided a reflective adhesive is used, incident polarized light rays will be reflected on that interface, and may be intercepted by the analyser of a reflexion polariscope, in much the same way as in a transmission polariscope.

The only difference stems from the fact that the beam of light crosses the plastic twice; all the formulae established for a transmission polariscope are thus applicable to this particular configuration, provided $2t$ is used instead of t, where t is the thickness of the coating.

Fig. 1.1 shows the path of light and the configuration of a reflexion polariscope, in normal and oblique incidences.

This technique enables the analysis in situ of all the parts of structures which are accessible to light.

At this stage, the interaction between the plastic and the specimen must be considered.

Although the modulus of elasticity of the plastic is only of the order of 500,000 psi [Ref. 1.7, 1.11], the coating contributes to the local strengthening of the specimen, expecially if the latter is thin.

This reinforcing effect was studied by Zandman [Ref. 1.13] who introduced a correction factor R, determined in terms of the relative thickness of the plastic to that of the specimen.

Provided a reflective adhesive is used, incident polarized light rays will be reflected on that interface, and may be intercepted by the analyser of a reflexion polariscope, in much the same way as in a transmission polariscope.

The only difference stems from the fact that the beam of light crosses the plastic twice; all the formulae established for a transmission polariscope are thus applicable to this particular configuration, provided $2t$ is used instead of t, where t is the thickness of the coating.

Fig. 1.1 shows the path of light and the configuration of a reflexion polariscope, in normal and oblique incidences.

This technique enables the analysis in situ of all the parts of structures which are accessible to light.

At this stage, the interaction between the plastic and the specimen must be considered.

Although the modulus of elasticity of the plastic is only of the order of 500,000 psi [Ref. 1.7, 1.11], the coating contributes to the local strengthening of the specimen, expecially if the latter is thin.

This reinforcing effect was studied by Zandman [Ref. 1.13] who introduced a correction factor R, determined in terms of the relative thickness of the plastic to that of the specimen.

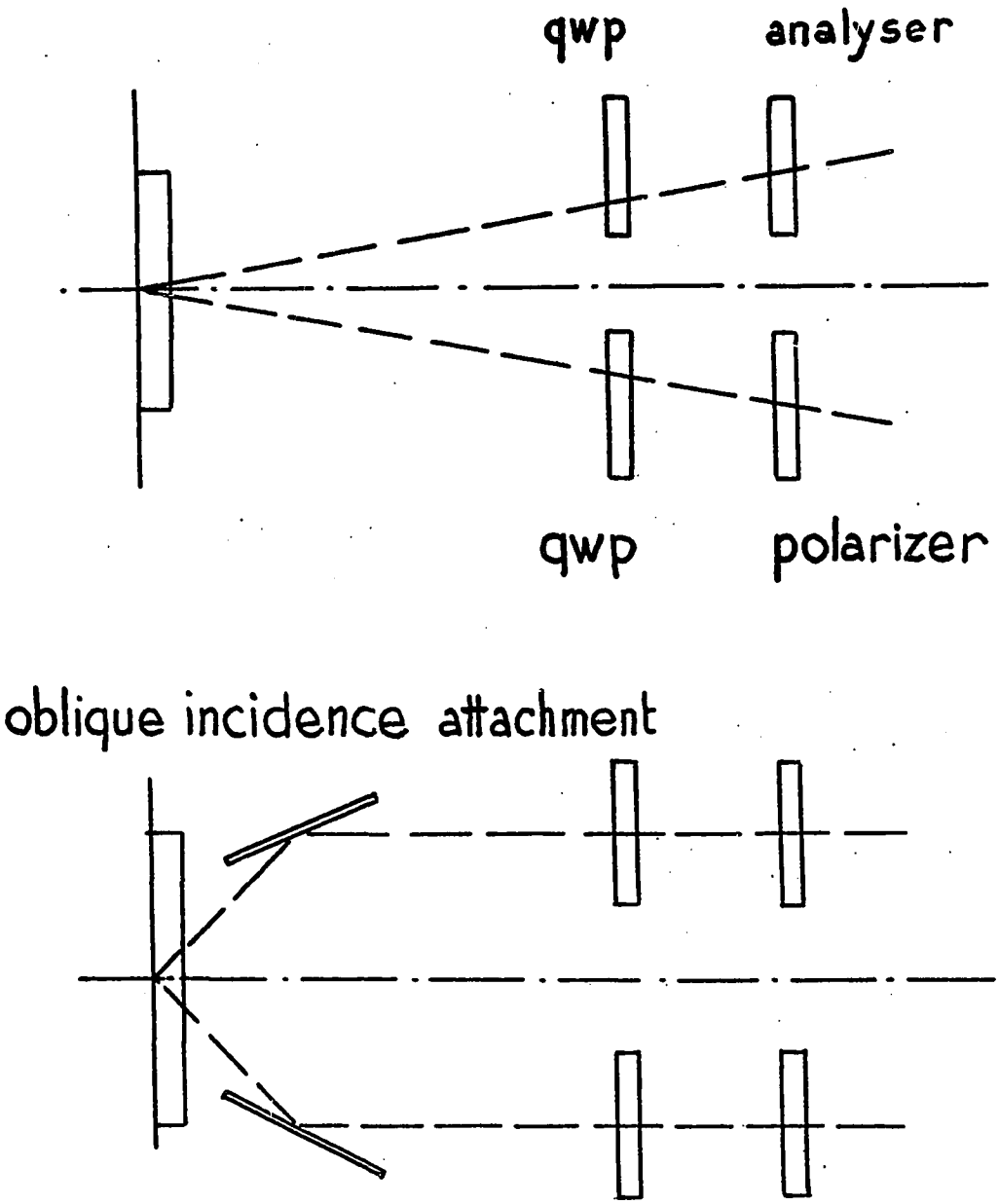

Fig. 1.1 The reflexion polariscope in normal and oblique incidence.

Two cases were considered: a two dimensional stress distribution in the plane of the specimen, and the bending around an axis situated in that plane.

The interaction between the plastic and its support may be treated as follows.

Using the suffix "s" for the specimen, and "p" for the plastic.

$$(\sigma_1 - \sigma_2)_s = \frac{E_s(\epsilon_1 - \epsilon_2)_s}{1 + \nu_s} \tag{1.1}$$

$$(\sigma_1 - \sigma_2)_p = \frac{E_p(\epsilon_1 - \epsilon_2)_p}{1 + \nu_p} \tag{1.2}$$

Also, the angular retardation Δ_n between the polarized rays is given by:

$$\frac{\Delta_n}{2tCR} = \frac{(\epsilon_1 - \epsilon_2)_p E_p}{1 + \nu_p} \tag{1.3}$$

where C is the strain optical coefficient of the plastic. Hence,

$$(\epsilon_1 - \epsilon_2)_s = \frac{1 + \nu_p}{2tCRE_p} = \frac{\Delta_n}{2tKR}$$

where $$K = \frac{CE_p}{1 + \nu_p} \tag{1.4}$$

K, the strain optical factor of the plastic, is generally given by the manufacturer but may be obtained experimentally from a simple calibration test, as will be discussed later.

K does not vary with temperature, between -40 and +95°F [Ref. 1.10, 1.11].

Creep, when the plastic is bonded to its support, and the temperature is below 100°F will affect the readings to within the sensitivity of the measurements; the stress-strain diagram of the plastic is linear and elastic up to failure, which occurs for a strain of at least 0.03 [Ref. 1.11].

Compensation may be achieved as for a transmission polariscope; the Tardy method is often preferred to the others, since requiring no additional equipment.

The determination of individual stresses or strains, however presents different aspects.

Methods of numerical integration based on Lame-Maxwell's equations could, in principle, be used; however the bonding procedure calls for a bevel of adhesive around the plastic, in order to prevent air bubbles from seeping underneath.

Stresses are transmitted from the loaded specimen to the plastic through this bevel, as well as in shear at the interface, so that no genuine free edge is available: further experimental data must be obtained.

This may be done conveniently by using oblique incident light. The relative retardation in oblique incidence is proportional to the difference of the secondary principal stresses in planes perpendicular to the beam of light.

Two cases must be considered.

If the planes of polarization are parallel to the principal directions at the point under consideration, and if θ is the angle of incidence, the following system of equations may be written [Ref. 1.10]

$$(\sigma_1 - \sigma_2)_p = \frac{n_n \lambda}{2t\ CR}$$

$$(\sigma_1 - \sigma_2 \cos^2\theta)_p = \frac{n_o \lambda \cos \theta}{2t\ CR}$$

where n_n and n_o are the fringe orders in normal and oblique incidence, respectively.

For $\theta = 45^{o}$, these equations yield:

$$\sigma_1 = \frac{\lambda}{tCR}\left[\frac{n_n}{2} + \frac{\sqrt{2}}{2}\ n_o\right] \tag{1.5}$$

$$\sigma_2 = \frac{\lambda}{tCR}\left[-\frac{n_n}{2} + \frac{\sqrt{2}}{2}\ n_o\right] \tag{1.6}$$

from which one may derive, for the Photostress material [Ref. 1.17]

$$\epsilon_1 = \frac{\lambda}{2tKR}\ [1.51\ n_o - 1.02\ n_n] \tag{1.7}$$

$$\epsilon_2 = \frac{\lambda}{2tKR}\ [1.51\ n_o - 2.02\ n_n] \tag{1.8}$$

If the orientation requirement above is not satisfied, three separate measurements are necessary, and the following equations must be used [Ref. 1.4]:

$$n_n F_n = 4\sigma_{xy}^2 + (\sigma_x - \sigma_y)^2 \tag{1.9a}$$

$$n_{01}F_{01} = 4(\sigma_{xy} \cos \theta_1)^2 + (\sigma_x - \sigma_y \cos^2\theta_1)^2 \tag{1.9b}$$

$$n_{02}F_{02} = 4(\sigma_{xy} \cos \theta_2)^2 + (\sigma_x - \sigma_y \cos^2\theta_2)^2 \tag{1.9c}$$

A few points must be noted, however:

- the stresses are not necessarily constant over the whole thickness of the plastic; this is especially noticeable along the edges perpendicular to

large stresses' trajectories where no measurements should be taken within a distance $4t$ from the edge [Ref. 1.11].

Hence, the retardation measured is proportional to the average principal stresses difference throughout the thickness, and not at the interface.

- In oblique incidence at 45^{o} , (fig. 1.2) the retardation is also averaged over a distance $2t$ along the plastic; double reflexion also tends to blur the image somewhat.

- Formulae (1.7) and (1.8) call for the difference of numbers which are usually of the same order of magnitude, hence great care must be exercised to obtain both n_n and n_o with great accuracy.

- In order to eliminate any residual or accidental birefringence that might be present in the plastic prior to loading, an initial reading under zero load is compulsory.

Equations (1.7 and 1.8) will thus be used in incremental form, as:

$$\delta(\epsilon_1) = \frac{\lambda}{2tKR}\left[1.51\ \delta(n_o) - 1.02\ \delta(n_n)\right] \tag{1.10}$$

$$\delta(\epsilon_2) = \frac{\lambda}{2tKR}\left[1.51\ \delta(n_o) - 2.02\ \delta(n_n)\right] \tag{1.11}$$

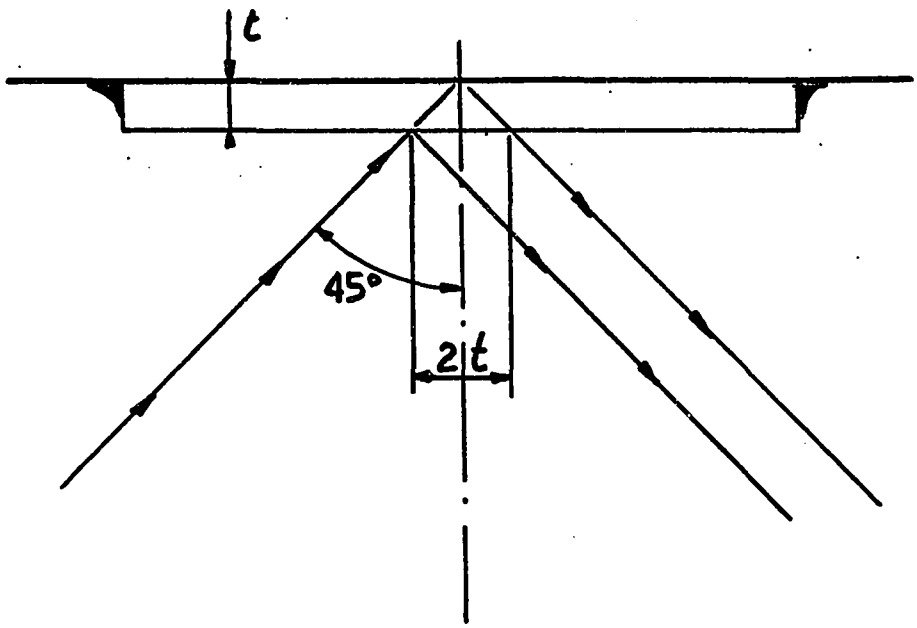

Fig. 1.2 The path of light in oblique incidence.

These remarks would tend to recommend the use of very thin sheets of plastic; however these produce less relative retardation and will yield smaller fringe orders for a given strain condition, and a given Photostress material.

Additional errors will stem from the interpolation between wider spaced fringes.

Finally, it must be recognized that the plastic may be calibrated both for stresses and strains; however only the last procedure is used, since the stresses in the plastic are not representative of the stresses in the test specimen.

This is due to the difference in Poisson's ratio for both materials.

The discussion above was carried for monochromatic light; it is still valid for white light [Ref. 1.15], except that the black isochromatics are replaced with a succession of light spectra, oriented along the directions of maximum shear stress gradient.

Full fringe orders are denoted by the sharp passage from red to green, called tint of passage, and to which the eye is particularly sensitive.

λ, in the formulae, is then the wave length corresponding to this tint of passage.

The use of white light has many advantages; it enables the distinction between isoclinics and isochromatics in a plane polariscope;.in a circular polariscope, the zero order isochromatic remains black, so that the numbering of the fringes is made easier.

Finally, the human eye is more sensitive to the tint of passage than to the lines of maximum intensity in a monochromatic pattern. [Ref. 1.15].

However, sources of error are also introduced. Whereas it is possible to produce sheets of material (Polaroid for instance) which are almost perfectly dichroic over a wide range of wave lengths [Ref. 1.3], it must be noted that the retardation of the quarter wave plates is strictly a function of the wave length of the incident light [Ref. 1.7].

Besides, as the fringe order increases certain colours disappear from the full spectrum.

Above the third order, the colour sequence reduces to white, pink and green, becoming paler everytime. [Ref. 1.7].

All the experiments were conducted in white light.

CHAPTER II

The Moment Rotation Capacity of a Hinging Region in a Reinforced Concrete Member.

2.1 Introduction.

Methods of limit design of frames are based on the assumption that a certain number of hinges are formed in the members; the ultimate load carrying capacity is reached when the structure thus obtained is a mechanism.

Rotation capacity of concrete members however is limited, and a careful check must be made to ensure that the rotation capacity of any part of the structure is not exceeded before all the hinges have formed, i.e., before the collapse load has been reached.

Besides, the ultimate resistance to dynamic loading is a function of the amount of strain energy stored, which in turn depends on the rotation capacity of the hinging regions.

Given such a region of length ℓ_p, let M and Φ be the ultimate moment and rotation at abscissa x. The total strain energy stored in bending is then:

$$U = \int_o^{\ell} M \ \Phi \ dx \qquad (2.1)$$

In the first part of this chapter, the characteristics of a given cross section will be studied, with the main objective of determining its moment curvature diagram up to failure.

Methods of obtaining the rotation between the extremities of a given length of a member will be the object of the second part.

The discussion will be limited to the case of the pure bending of rectangular beams.

Shearing deformations will be neglected throughout.

Further assumptions will be made in due course.

Notations of the American Concrete Institute will be used whenever possible.

2.2 The Moment curvature relationship for a reinforced concrete section.

The following analysis is restricted to the case of under-reinforced concrete sections, as defined later in this section.

Such sections feature a more ductile behaviour and are the usual type encountered in design.

Keeping this restriction in mind, four well defined stages may be observed during the testing to failure of a member in bending :

1. The initial application of the load,
2. The initiation of the first crack in the tensile zone,
3. The yielding of the steel reinforcing bars,
4. The failure of the member, defined here by the ultimate load, moment and deformations, beyond which the member is unable to sustain any further load.

These four stages define four points in the moment-curvature diagram, which will be taken linear between these four points. [Ref 2.1] (fig 2.1).

Some authors, however, disregard the first uncracked phase, and consider the moment-curvature diagram as essentially bi-linear. [Ref 2.21] (fig 2.6, page 47).

Kp, the plasticity factor, defines entirely the behaviour of the member in the inelastic range. Such a diagram lends itself extemely well to the plastic analysis of concrete structures, since : "the familiar moment-area principles for elastic analysis may be used if the inelastic area expanded by the plasticity factor Kp are included in addition to the total M/EI area." (Sawyer) [Ref 2.21].

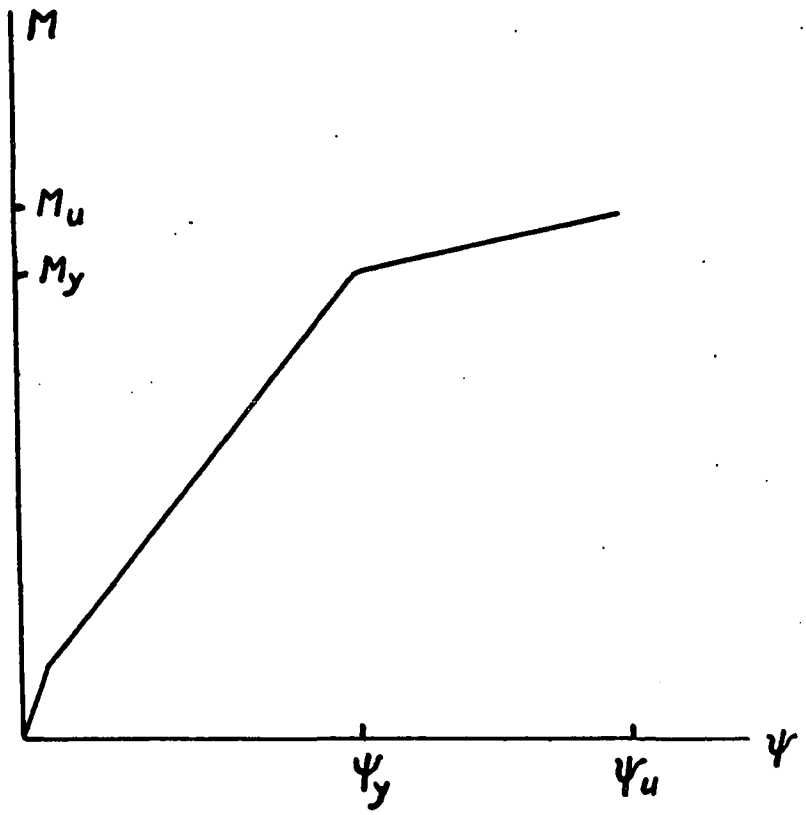

Fig. 2.1 The moment-curvature diagram.

In the following sections, the tri-linear moment curvature diagram will be considered in detail, rather than the simplified approach outlined above.

The first approach is indeed better suited to correlate experimental results, when a detailed observation is carried out at low or intermediate loads.

2.2.1 The initial stage of loading.

Before the first crack develops the section may be analyzed as a homogeneous body, after transforming the tensile and compressive steel areas into equivalent concrete areas.

Strain and stress distributions are linear throughout the section; the maximum tensile stress in concrete must be smaller than its tensile strength.

By referring to fig. 2.2, the following expressions may be derived :

$$kd = \frac{0.5\ bh^2 + A_s(n - 1)d + A'_s(n - 1)d'}{bh + (n - 1)\ (A_s + A'_s)\ d} \qquad (2.2)$$

$$I = \frac{bh^3}{12} + bh\ [kd - \frac{h}{2}]^2 + A_s(n - 1)[d - kd]^2 + A'_s(n-1)\ [kd - d']^2 \qquad (2.3)$$

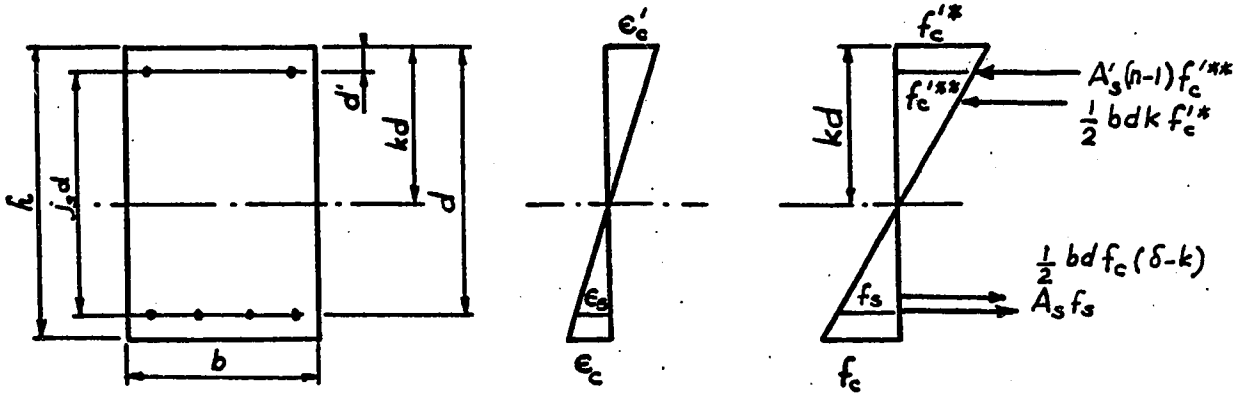

Fig. 2.2 The initiation of cracking.

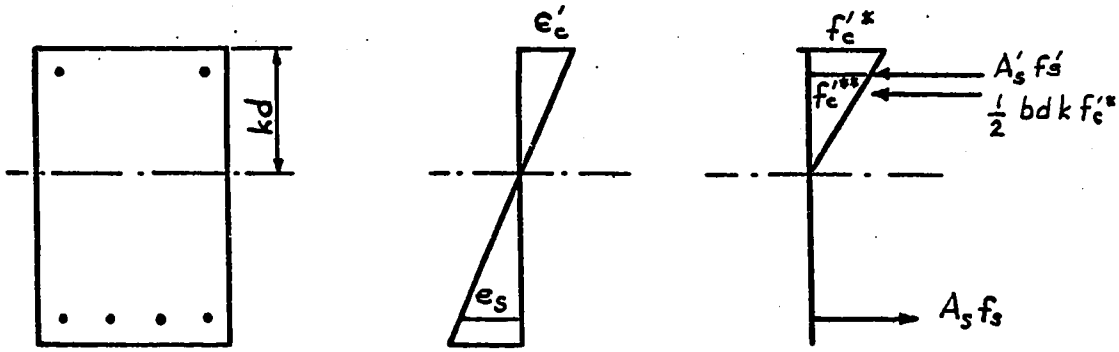

Fig. 2.3 The cracked section.

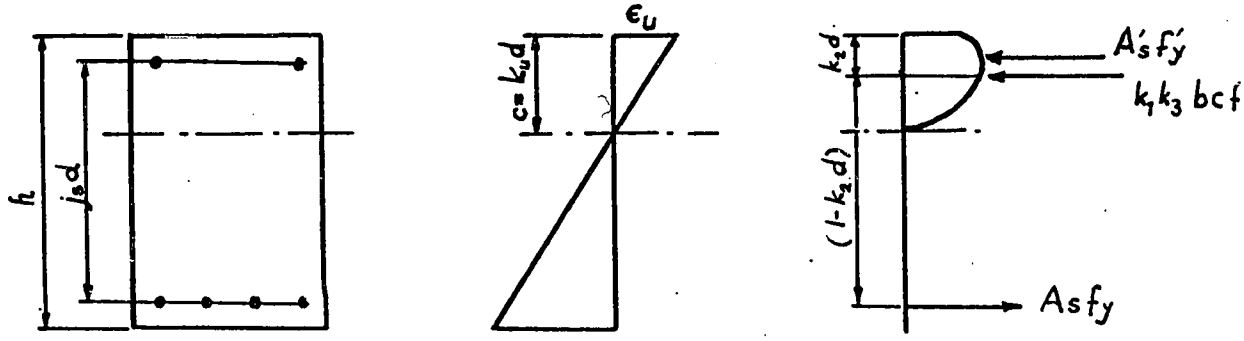

Fig. 2.4 The cross section at ultimate.

or, after transformation :

$$k = \frac{\delta^2 + 2p\,(n-1) + 2p'(n-1)\,(1-j_s)}{2\delta + 2(n-1)\,(p+p')} \qquad (2.4)$$

$$(2.5)\quad I = bd^3\left[\frac{\delta^3}{3} + \delta\,k(k-\delta) + p(n-1)\,(1-k)^2 + p'(n-1)\,(k+j_s-1)^2\right]$$

The axial stresses at a distance v from the neutral axis are then, under a given moment M :

$$\sigma = \frac{Mv}{I} \,. \qquad (2.6)$$

Substituting f_c for σ, and solving (2.6) for M gives the maximum moment resisted by the beam before the first crack is initiated, as follows :

$$M = \frac{f_c\, bd^2}{\delta - k}\left[\frac{\delta^3}{3} + \delta\,k(k-\delta) + p(n-1)(1-k)^2 + p'(n-1)(k+j_s-1)^2\right] \qquad (2.7)$$

The curvature ψ at this stage is given by

$$\psi = \frac{1}{R} = \frac{M}{E\,I} = \frac{f_c}{E\,(\delta - k)d} \;; \qquad (2.8)$$

it might as well be derived from :

$$\psi = \frac{\epsilon_c' + \epsilon_s}{d} \qquad (2.9)$$

When $p' = 0$, these formulae may be further simplified into:

$$k = \frac{\delta^2 + 2p(n - 1)}{2\delta + 2(n - 1)p} \tag{2.10}$$

$$I = bd^3 \left[\frac{\delta^3}{3} + \delta k(k - \delta) + p(n - 1)(1 - k)^2\right] \tag{2.11}$$

$$M = \frac{f_c bd^2}{\delta - k} \left[\frac{\delta^3}{3} + \delta k(k - \delta) + p(n - 1)(1 - k)^2\right] \tag{2.12}$$

They are similar to those given in [Ref. 2.2]δ

2.2.2 The cracked section in the elastic range of steel deformations.

Once the tensile strength of concrete has been reached at the bottom fibers, cracks develop through the tensile zone of the member, and become deeper and deeper as the load is increased.

Due to the order of magnitude of the stresses and strains encountered in this range, it is justified to assume a linear distribution of the latter throughout the cross sections, and that Hooke's law holds.

Bond failures are not considered here.

As the cracks progress, the moment of inertia of the section decreases; cracked sections are thus sections of maximum axial stresses and strains.

Given the latter, the assumptions above make the rigorous calculation of the resisting moment possible; however, the inverse procedure is not possible without trial and error.

Given a bending moment, it is not possible to obtain the stresses and strains exactly, because the depth of the cracks is unknown.

For the solution of design problems, one further assumption is then made, that consists of neglecting tensile stresses in concrete. That assumption will be further discussed in section 2.3.2.

This leads to the diagram of fig 2.3 from which the following formulae may be derived [Ref 2.1)

$$A_s f_s = A'_s (n - 1)\, f'^{**}_c + 0.5\, f'^{*}_c \quad bdk \,. \tag{2.13}$$

However,

$$f'^{**}_c = f'^{*}_c \times \frac{j_s d - (1 - k)d}{kd} = f'^{*}_c \frac{j_s + k - 1}{k} \,,$$

hence

$$A_s f_s = A'_s (n - 1)\, f'^{*}_c \frac{j_s + k - 1}{k} + 0.5\, f'^{*}_c \quad bdk \tag{2.14}$$

Also,

$$f_s = E_s \epsilon_s \,, \quad f'^{*}_c = E_c \epsilon'_c$$

$$f_s = E_s \frac{1 - k}{k} \epsilon'_c \,, \tag{2.15}$$

so that by introducing p and p',

$$\frac{p f_s}{f'^{*}_c} = pn\left(\frac{1 - k}{k}\right) = p'(n - 1) \frac{j_s + k - 1}{k} + 0.5\, k \tag{2.16}$$

This expression may be rewritten as :

$$k^2 + 2k[(n - 1)p' + pn] + 2(n - 1)p'(j_s - 1) - 2pn = 0 \tag{2.17}$$

of which the single acceptable root reads

$$k = -[(n - 1)p' + pn] + \sqrt{[(n - 1)p' + pn]^2 + 2[pn + (n - 1)p'(1 - j_s)]} \qquad (2.18)$$

k is a function of p,p',n only; hence the neutral axis does not shift during this stage of the loading process.

This conclusion stems from the last assumption made. It is justified by the fact that the contribution of the tensile stresses in concrete to the resisting moment of the section is very small indeed.

Solving (2.16) for f'^*_c, and equating the couple of the forces acting on the cross section yields :

$$f'^*_c = \frac{pf_s}{0.5k + (n - 1)p'(j_s + k - 1)/k} \qquad (2.19)$$

$$M = 0.5\, f'^*_c\, bd^2k(1 - \frac{k}{3}) + j_s d\, A'_s f'_s \qquad (2.20)$$

The curvature is given by

$$\psi = \frac{\epsilon_s}{(1 - k)\, d} \qquad (2.21)$$

When the steel is about to yield $f_s = f_y$; in the case of a beam without compression reinforcement, the expressions (2.18) to (2.21) may be simplified into :

$$k = - np + \sqrt{(pn)^2 + 2\,pn} \qquad (2.22)$$

$$f'^{*}_{c} = \frac{2pf_y}{k} \qquad (2.23)$$

$$M_y = 0.5\ f'^{*}_{c}\ bd^2k\ (1 - \tfrac{k}{3}) \qquad (2.24)$$

$$= pf_y\ bd^2(1 - \tfrac{k}{3}) \qquad (2.25)$$

$$\psi = \frac{\epsilon_y}{(1 - k)d} \qquad (2.26)$$

These formulae yield slightly exaggerated values for the stresses and the strains.

From $\psi = M/EI$, a value of the effective moment of inertia of the cross section may be derived; it is constant over the whole present range.

Clearly, this is only an approximation of the real behaviour.

In particular, the moment-curvature diagram derived is a straight line passing at the origin, which is in contradiction with the first part of this chapter.

In the case when theoretical values of deflections, strains or curvatures are needed, a different approach must be taken.

The reader will appreciate that the formulation above holds true for high values of the moment, and in particular when $f_s = f_y$.

Hence, one shall consider the curvature obtained from (2.26) as a true value, and the $M - \psi$ diagram to be linear between the limits of the range.

It is thus possible to calculate ψ for every value of M ; since k is constant, the strains may be derived easily.

2.2.3 The inelastic range.

The last part of the moment curvature diagram corresponds to the inelastic behaviour of the beam, up to failure.

Experiments have shown that the $M-\psi$ relationship could be taken linear over this range as well, [Ref 2.1] and that the moment increases as the curvature increases.

Strain distribution may be considered linear inside the cross section [Ref 2.3, 2.4].

However, the stress in the tensile reinforcement remains approximately constant at the value f_y, this implies that the lever arm of the resultant forces lengthens, hence that a progressive redistribution of stresses occurs in the compression zone. Stresses may thus no longer be considered to vary linearly.

Theoretically, the shape of the stress block at all stages of the loading process is identical to that of the stress-strain curve of the concrete in compression, between the origin and the maximum strain observed at the topmost compression fiber.

If the stress-strain curve may be put into an analytical form, then for any given strain, the calculation of the position of the neutral axis, and of the resisting moment becomes a pure exercise of calculus [Ref 2.9].

Idealized stress-strain curves are often encountered in the literature [Ref 2.3, 2.5, 2.11], and are recognized by several codes of practice [Ref 2.6].

In design, only the ultimate moment strains and deformations are required.

The admitted procedure for that stage is to replace the actual stress block by an equivalent rectangular block, having the same resultant force as the real one [Ref 2.4, 2.7, 2.8].

The procedure adopted in North America consists of defining the resultant force of the compressive stresses in terms of three coefficients k_1, k_2 and k_3, defined as follows : (fig 2.4)

k_1 is the ratio of the average concrete compressive stress to the maximum stress.

k_2 is the ratio of the depth of the resultant force to the depth of the neutral axis;

k_3 is the ratio of the maximum compressive stress to the resistance of concrete in compression, f_c', as determined by standard tests on 6in. x 12in. cylinders.

Using these coefficients, and calling $c = k_u d$ the depth of the neutral axis, one can express the conditions of equilibrium

and compatibility, and deduce the following formulae [Ref 2.1]

$$A'_s f'_y + k_1 k_3 f'_c bc = A_s f_s \tag{2.27}$$

$$M_u = k_1 k_3 f'_c bc (d - k_2 c) + f'_y A'_s j_s d \tag{2.28}$$

Two further assumptions have been made to derive these formulae.

1) The steel in compression is yielding; it is stressed at a constant value f'_y, which may be different from f_y.

   This assumption is justified by the order of magnitude of the strains in concrete at ultimate.

2) The area of concrete occupied by the compressive steel has been neglected.

Using the steel percentages p and p', (2.27) and (2.28) may be rewritten as follows :

$$c = d \frac{p f_s - p' f'_y}{k_1 k_3 f'_c} \tag{2.29}$$

$$M_u = bd^2 \left[(p f_s - p' f'_y)\left(1 - k_2 \frac{p f_s - p' f'_y}{k_1 k_3 f'_c}\right) + p' j_s f'_y \right] \tag{2.30}$$

k_1, k_2 and k_3 have been determined experimentally, and are constants [Ref 2.9]; M_u is thus a function of f_s.

$$\text{Also, } \frac{c}{d} = \frac{\epsilon_u}{\epsilon_u + \epsilon_s} \quad , \tag{2.31}$$

hence by eliminating c between (2.29) and (2.31)

$$f_s = \frac{1}{p} \left[k_1 k_3 f'_c \frac{\epsilon_u}{\epsilon_u + \epsilon_s} + p' f'_y \right]. \tag{2.32}$$

In these formulae, ϵ_u may be given the value

$$\epsilon_u = 0.003 + 0.5/z \tag{2.33}$$

where z is the distance between the section considered and the point of inflexion of the member [Ref. 2.1]. Three cases must be examined according to the relative values of f_s and f_y :

1. $f_s < f_y$ The beam is overreinforced. The beam fails in compression, this case does not correspond to the assumptions of our analysis, and the moment-curvature diagram of the beam is not as shown in fig. 2.1 .

2. $f_s = f_y$ The beam is said to undergo a balanced type of failure. Equations (2.29) to (2.31) apply after substitution of f_s by f_y . The curvature may be obtained by

$$\psi = \frac{\epsilon_u}{c} = \frac{\epsilon_u}{k_u d} \tag{2.34}$$

3. $f_s > f_y$ The reinforcing steel is stressed into its strain hardening range, and

$$\epsilon_s = \frac{f_s - f_o}{E'_s} \tag{2.35}$$

where E'_s is the strain hardening modulus, and f_o is defined on fig 2.5

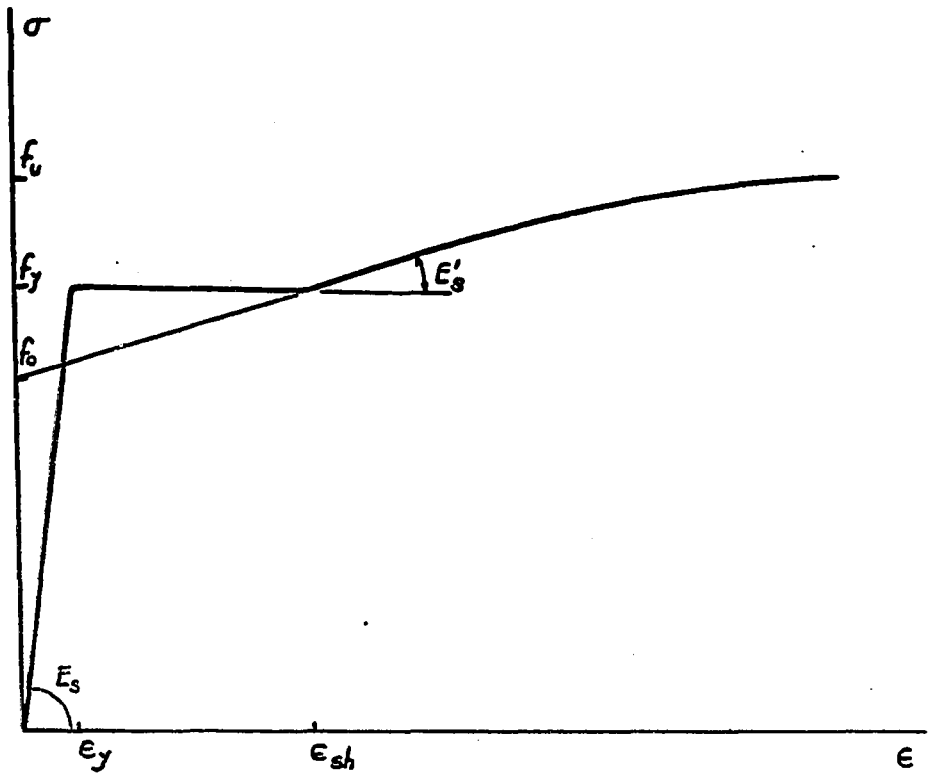

Fig. 2.5 The stress-strain curve for steel.

f_s may be obtained from

$$f_s = \frac{1}{p}\left[k_1 k_3 f'_c \frac{\epsilon_u E'_s}{\epsilon_u E'_s + f_s - f_o} + p' f'_y \right] \tag{2.36}$$

A criterion must now be established that will determine which of the three above modes applies to each case.

From (2.32),

$$\frac{p f_s - p' f'_y}{f'_c} = k_1 k_3 \frac{\epsilon_u}{\epsilon_s + \epsilon_u} \tag{2.37}$$

hence

$$q - q' = k_1 k_3 \frac{\epsilon_u}{\epsilon_u + \epsilon_s} \tag{2.38}$$

Let $(q - q')_b$ and $(q - q')_{sh}$ the values of $(q - q')$ when $\epsilon_s = \epsilon_y$ and $\epsilon_s = \epsilon_{sh}$ respectively,

Hence, if $(q - q') > (q - q')_b$ then $f_s < f_y$ (2.39)

$(q - q')_{sh} < q - q' < (q - q')_b$ then $f_s = f_y$ (2.40)

$(q - q') < (q - q')_{sh}$ then $f_s > f_y$ (2.41)

The expression 16.3 of [Ref. 2.7],

$$M_u = bd^2 f'_c q(1 - 059\ q) \tag{2.42}$$

may be derived from (2.30) for appropriate values of k_1 , k_2 , k_3

whereas expression (2.40) may be transformed into the condition 16-2

of the same Code Requirements:

$$p = \frac{0.85\, k_1\, f'_c}{f_y} \cdot \frac{87000}{87000 + f_y} \qquad (2.43)$$

As mentioned earlier, the problem of obtaining stresses and strains at intermediate stages of the inelastic range is somewhat more delicate.

From the linear shape adopted for the moment-curvature diagram, however, it is possible to obtain approximate values for the strains in the concrete and steel, for a given moment.

Assume first that the depth of the neutral axis, $k\,d$, varies in a known way between M_y and M_u.

The expression for the depth of the equivalent stress block in [Ref. 2.7] suggests the adoption of a linear variation.

From the $M - \psi$ diagram, and from the value obtained for k_1, ϵ_c and ϵ_s may be obtained, and also a value for I.

Naturally, the stresses may not be calculated without choosing a shape for the stress block, which would be consistent, at ultimate, with the equivalent rectangular stress block adopted before.

The ductility of a member's cross section may be expressed as the ratio [Ref. 2.12]

$$\frac{\psi_u}{\psi_y} = \frac{\epsilon_u}{\epsilon_y} = \frac{1 - k}{k_u} \tag{2.44}$$

The conditions for a very ductile section are thus clearly stated:

- ϵ_u must be as large as possible,
- k and k_u must be as small as possible

This calls for sections with compressive reinforcement, close stirrups and small tensile steel percentage [Ref. 2.12].

For the sake of completeness, reference will be made here to the works of Barnard [Ref. 2.19] and Burnett [Ref. 2.20] who recognize the existence of a descending branch that continues the moment-curvature curve, and corresponds to the strain softening branch of the stress-strain curve of concrete [Ref. 2.15].

2.3 Moment-Rotation diagram

2.3.1 Introduction:

In the former section of this chapter, it has been shown that the moment curvature diagram of a rectangular reinforced concrete member in pure bending could be established once the properties of the cross section were known.

The strain distribution, and an effective value of the moment of inertia of the cracked section were also determined.

However, if the concept of curvature is well defined for metal beams, it is not as clear in concrete.

Whereas plastic hinges develop in a continuous way in the first case, they develop in an essentially discontinuous manner in a brittle material, through the formation of a discrete number of cracks of finite width.

Measuring the curvature of a member becomes a delicate operation, and much of the result depends on the gauge length adopted for the measurements. Besides, the length of the plastic hinge often extends further than the distance of theoretical plastification.

Another reason acts in favor of the concept of moment rotation, rather than moment-curvature.

It is generally admitted that no large error is made by expressing the inelastic deformation of a member in bending in terms of the finite rotation of a plastic hinge occurring in a definite cross section.

This assumption simplifies the computation of redundant structures, and is in fact the basis of the methods of analysis of frames established by Baker [Ref 2.3], Macchi, and Cohn-Petcu [Ref 2.13]. It is thus appropriate to pause, and examine the methods developed to obtain the moment-rotation properties of members.

Again, the discussion will be restricted to the case of members of rectangular cross-sections, subjected to pure bending.

This corresponds to the conditions in which the beams of the experimental program were tested.

2,3.2 The theoretical moment-rotation relationship

It has been seen that the obtension of large curvatures in concrete is achieved by the formation of a discrete number of cracks, and that there is a concentration of stresses and strains at each cracked section.

This fact is incompatible with any analytical determination of moment-rotation characteristics, in which one would expect the curvature to be a continuous function.

A closer look at various cross-sections of a cracked member, however, will show

- that the strains in the tensioned concrete between cracks are small, and
- that the contribution of the tensile stresses to the resisting moment is negligible.

The last observation leads to the assumption used in section 2.2.2.

The physical implication is that every section may now be treated as if it were cracked, the sagging of the neutral axis between cracks being neglected; from formula (2.21) we will see that ψ is thus made a continuous function, without appreciable loss of accuracy.

By definition, the rotation of a concrete member over a length lp is given by

$$\Phi = \int_{o}^{lp} \psi(x) \; dx \qquad (2.45),$$

where,

$$\psi = \frac{1}{R} = \frac{M}{E_c I} \qquad (2.46),$$

In these formulae, both M, E_c and I are functions of the abscissa x , since E_c may be taken as the secant modulus given at ultimate by [Ref 2.3]

$$E_c = \frac{f'^*_c}{0.002}$$

M(x) is known, in the case of statically determinate members; $E_c I$ may be determined indirectly from

$$\psi(x) = \frac{\epsilon'_c(x)}{k(x)\, d} \qquad (2.47)$$

Hence, the rotations and deflections of a simply supported beam can be determined from (2.52), or more generally, by integration of

$$\frac{\partial^2 y}{\partial x^2} = \frac{M}{E_c I} \qquad (2.48)$$

An alternative approach consists of determining the value of $M/E_c I$ at a certain number of nearby sections, and to use numerical or graphical methods of integration.

Modern computer methods of structural analysis do provide another powerful tool.

For a given system of loads acting on a beam one first determines the value of ψ and of $E_c I$ at α nearby sections, one shall then assume a constant value of E_c, and derive the effective value of I at these sections.

The member may now be considered as a continuous beam, having $\alpha + 1$ spans of different moments of inertia.

Provided that adequate restraint conditions are supplied at the ficticious intermediate joints, a computer programme solving continuous beam problems may be used.

Such a programme was written by the author on the indications of Messrs. Gere and Weaver [Ref 2.14] and is discussed elsewhere in this paper.

The repetitive use of this programme at various stages of a loading process yields the true picture of rotations and deflections of a member, up to failure.

From the principles established here, consider the curvature diagram drawn for simply supported beams subjected to 1 and 2 point loads respectively (fig 2.7).

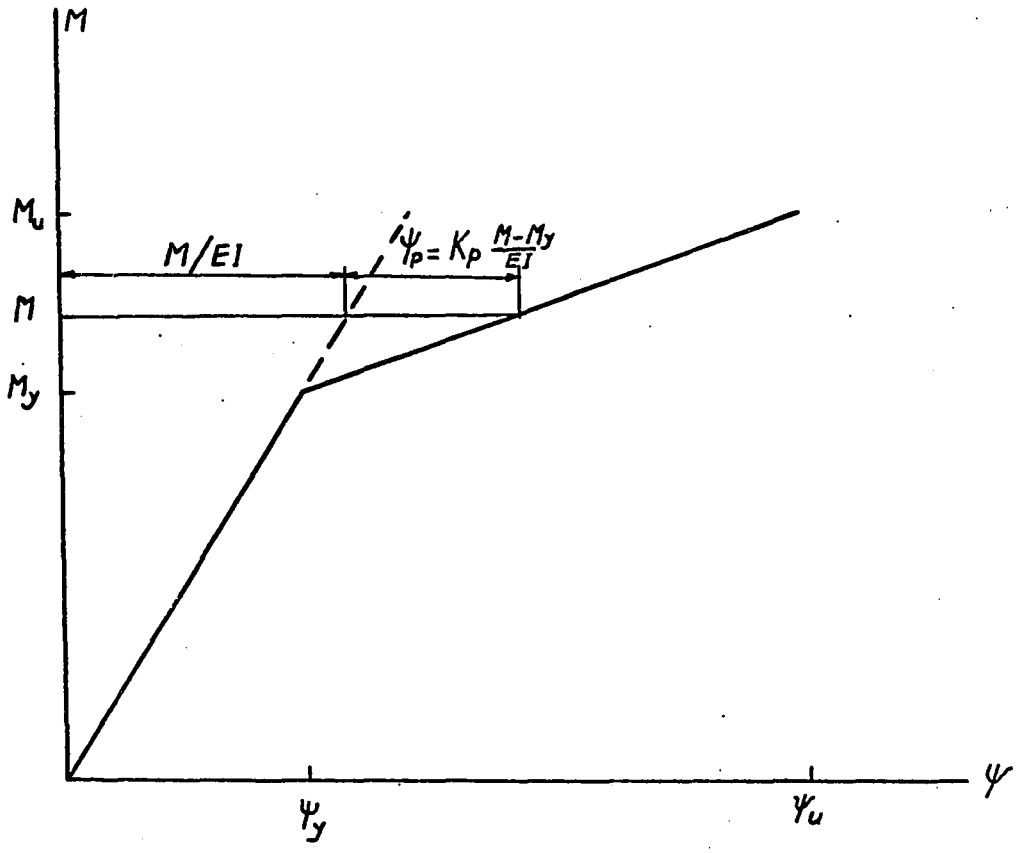

Fig. 2.6 Bilinear moment-curvature diagram.

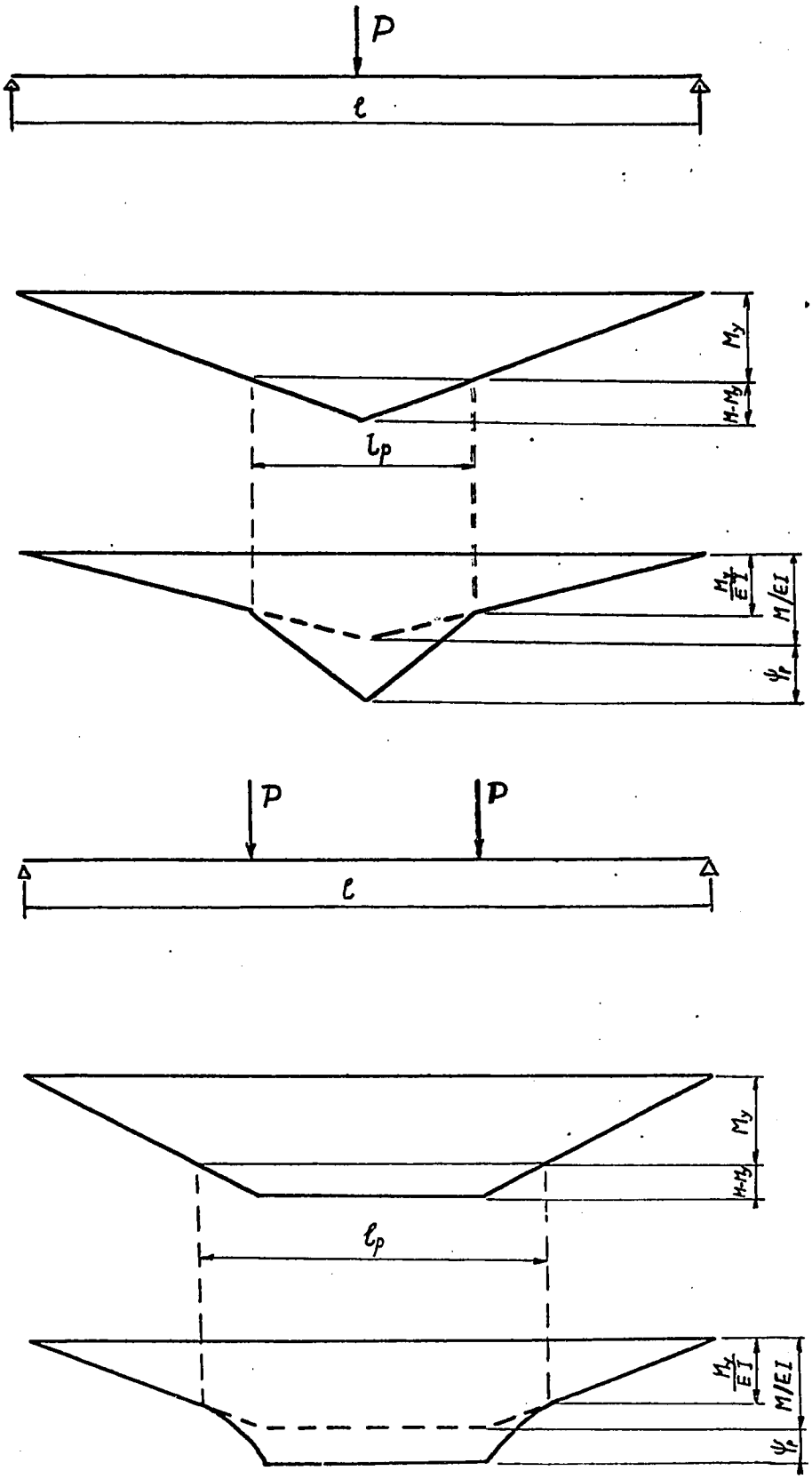

Fig. 2.7 The length of the hinging region.

In the first case, failure will occur at the centre of the beam, and the hinging region is very well defined.

In the second instance the hinging region has nearly the same length as the region of constant moment.

This is in contradiction with the assumption made in section 2.3.1, and with experimental observations which show that failure occurs most generally within a small length, due to the progression of one crack only. [Ref 2.13, 2.16].

This can be explained theoretically by the fact that formula (2.48) is only an approximation of

$$\psi = \frac{\partial^2 y}{\partial x^2} \Big/ \left[1 + \left(\frac{\partial y}{\partial x} \right)^2 \right]^{1.5} \qquad (2.49)$$

which shows that even if $\partial^2 y/\partial x^2$ is constant, there is a maximum value of ψ for $\partial y/\partial x = 0$, i.e. near the centre of the beam.

2.3.3. The bilinear moment-rotation diagram

For under-reinforced members a different approach consists of deriving the moment-rotation diagram from the idealized bilinear moment-curvature diagram discussed in section 2.2, and reproduced on fig 2.6.

This can be done mathematically [Ref 2.17].

As an example, consider a simply supported beam subjected to a concentrated load P at mid-span (fig 2.7). Let $M_{max} = \frac{PL}{4}$, and let fig 2.6 represent the M-ψ diagram at all sections of the beam; the curvature may be expressed as

$$\psi = \frac{M}{K_e} + \frac{M - M_y}{K'_p} \quad , \tag{2.50}$$

where K_e is the elastic rigidity of the beam,

K'_p is the plastic rigidity, or strain hardening coefficient of the beam.

The length of the plastic region is given by

$$\ell_p = \ell \times \frac{M_{max} - M_y}{M_{max}} \quad ,$$

and the total rotation over ℓ_p is

$$\Phi = \int_{-\frac{\ell_p}{2}}^{\frac{\ell_p}{2}} \psi(x)\, dx$$

Let $\Delta M = M - M_y$, and $\Delta M_{max} = M_{max} - M_y$;

then $M = M_y + \Delta M = M_y + \Delta M_{max} \left(1 - \frac{2x}{\ell_p} \right)$

$$\Psi(x) = \frac{M}{K_e} + \frac{M - M_y}{K'_p} = \frac{M}{K_e} + \frac{\Delta M_{max}}{K'_p} \left(1 - \frac{2x}{\ell_p} \right),$$

and Φ reads:

$$\Phi = \frac{M}{K_e} \ell_p + \int_{\frac{-\ell_p}{2}}^{\frac{\ell_p}{2}} \frac{\Delta M_{max}}{K'_p} \left(1 - \frac{2x}{\ell_p} \right) dx$$

$$= \Phi_e + \theta \quad ,$$

where $\theta = \frac{\Delta M_{max}}{K'_p} \times \ell'_p$

ℓ'_p is a constant; for this particular type of moment diagram,

$\ell'_p = \ell_p$.

The bilinear approach makes the determination of a moment-rotation diagram (fig 2.8) particularly easy, for beams of constant flexural rigidity.

The inelastic rotation is obtained as the product of the inelastic curvature by a plastic length ℓ'_p which can be determined for simple cases from the shape of the moment diagram.

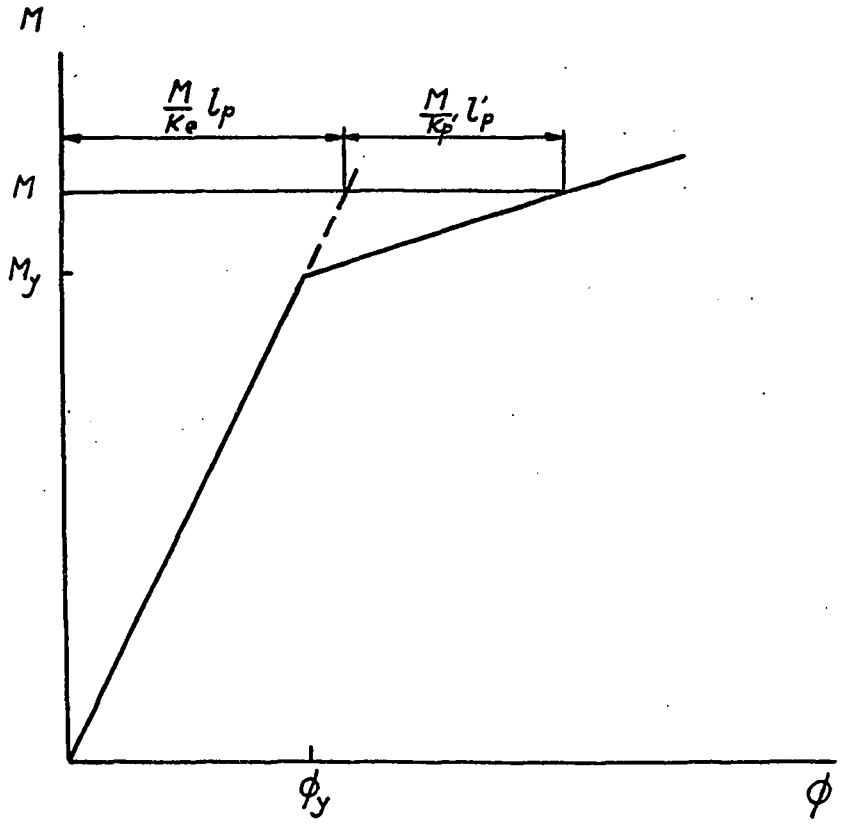

Fig. 2.8 The moment-rotation diagram.

A particular case of the bilinear law was proposed by Baker [Ref 2.3]; it consists of a pure elastic-plastic diagram.

The further simplification is that the inelastic behaviour does no longer depend on the shape of the moment diagram.

The whole moment-rotation curve is determined by two points L_1 and L_2 (fig 2.9), the coordinates of which are given in [Ref 2.3].

Further experiments at the Imperial College of Technology led to revised expressions in 1964 [Ref 2.5].

L_1 corresponds to M_y, and the rotation at L_1 is calculated on the basis of a maximum strain of 0.001 in steel; L_2 corresponds to failure, at a strain of 0.01 in steel.

Baker also defines the maximum inelastic rotation as

$$\theta = \frac{e_{cu} - e_{cy}}{k_u d} \ell_p , \qquad (2.51)$$

where ℓ_p is given in terms of coefficients which depend on the grades of steel and concrete.

Baker's simplified diagram is not derived from the concept of moment-curvature..

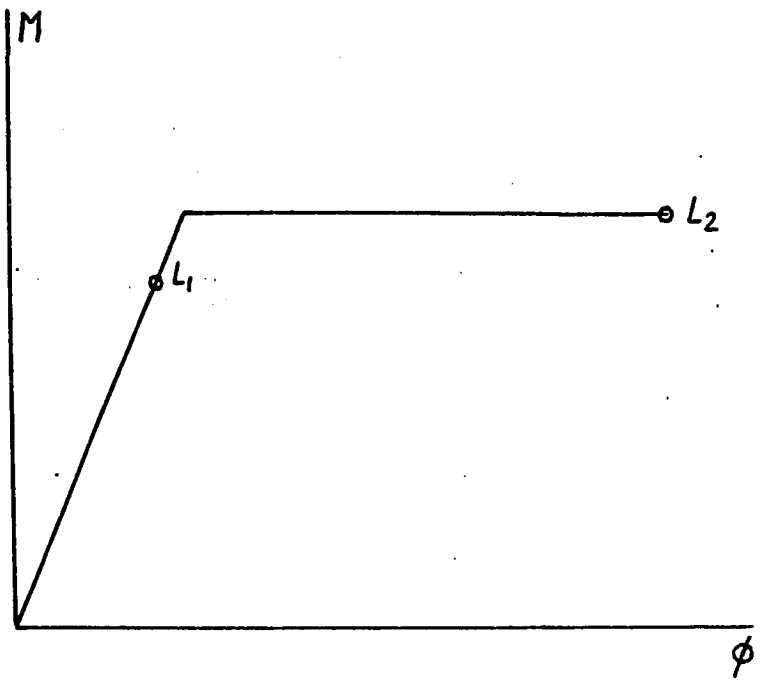

Fig. 2.9 Baker's moment-rotation diagram.

2.3.4 Recent experimental work.

Recent experimental work has been aimed at providing simplified expressions in which the inelastic angular displacements are given as the product of an average curvature ψ_u by a length ℓ_p taken as the length of the equivalent plastic region, (fig 2.10), Of particular interest in this field are the works of Mattock and Corley. Mattock [Ref 2.1] studied the moment rotation characteristics of reinforced concrete beams in the region of peak moments. He confirmed that the ultimate curvature may be taken as

$$\psi_u = \epsilon_u / k_u \, d \, , \qquad \text{where}$$

$$\epsilon_u = 0.003 + 0.5/z \tag{2.52}$$

Taking the inelastic rotation θ_u at a distance 0.5d from the cross section for reference, he defines the spread of plasticity as the ratio θ_{tu}/θ_u , where θ_{tu} is calculated over the distance z from the cross section.

The formulae used are :

$$\theta_u = \Phi_u - \Phi_y \, M_u/M_y \, , \qquad \text{where}$$

$$\Phi_u = \psi_u \frac{d}{2} \quad \text{and} \quad \Phi_y = \psi_y \frac{d}{2}$$

and

$$\frac{\theta_{tu}}{\theta_u} = 1 + (1.14z/d - 1) \left[1 - \frac{q - q'}{q_b} \sqrt{\frac{d}{16.2}} \right] \tag{2.53}$$

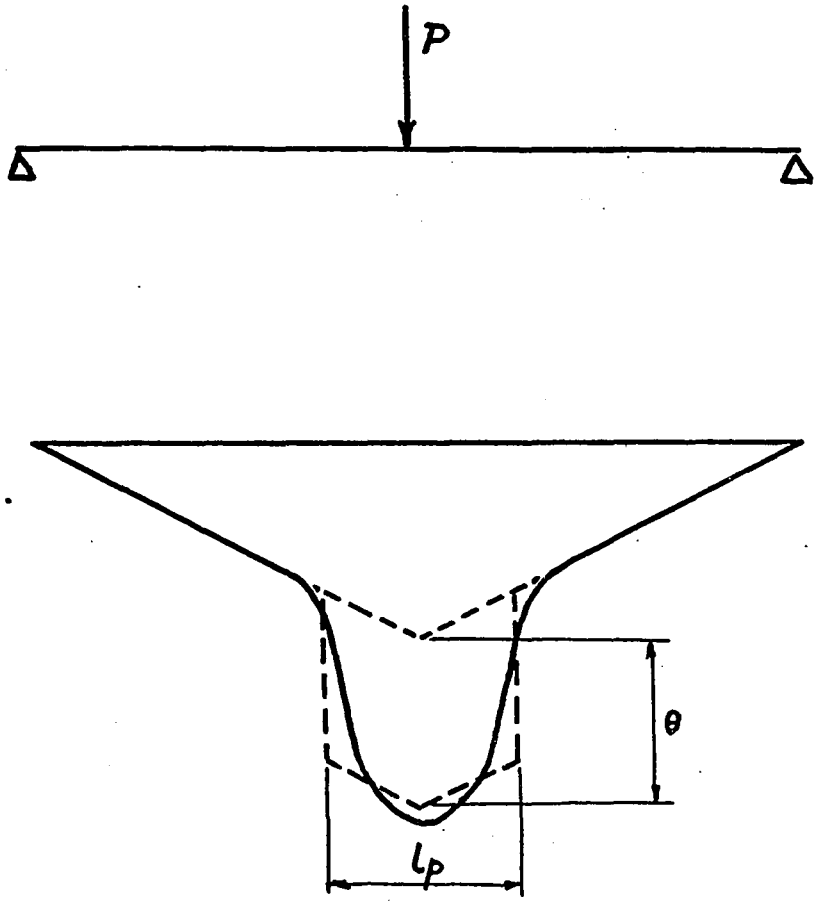

Fig. 2.10 The equivalent plastic region.

Corley [Ref 2.18] extended Mattock's work by including several more parameters in the study, particularly the percentage of binding steel p", and the size of the specimen.

He recommended to replace (2.52) with

$$\epsilon_u = 0.003 + 0.02 \frac{b}{z} + \left(\frac{p'' f_y}{20}\right)^2 \qquad (2.54)$$

where f_y must be expressed in ksi, thereby taking into effect the confinement of the concrete in compression due to the stirrups, and the width of the beam.

He also recommended to replace (2.53) with

$$\frac{\theta_{tu}}{\theta_u} = 1 + \frac{0.4}{\sqrt{d}} \cdot \frac{z}{d} \quad .$$

He observed that the size of the specimen did not have a significant influence on the magnitude of the maximum compressive strain in concrete.

CHAPTER III

Experimental results.

3.1 Introduction.

The experimental work described in this chapter is meant to determine whether the Photostress technique may be used to obtain the strain distribution in the hinging region of a reinforced concrete member.

A test programme was designed in the summer of 1967, and was carried out between August 1967 and August 1968.

It may be divided in three stages.

First, a series of simple tests on metal specimens was undertaken in order to get acquainted with the technique and to gain confidence in the readings. Calibration of the birefringent plastic also took place during that stage.

Then, a series of four mortar prisms was tested in axial compression; strains obtained by Photostress were compared to the readings of extensometers.

Finally, four beams were tested in bending and the fringe patterns were recorded on film.

For all the work described in the subsequent sections, technical help was strictly limited to the following:

- construction of a wooden form for four mortar prisms;
- lathe-turning of a steel pointer to apply the load on the metal strips used for the calibration tests;
- flame bending, welding and brazing of steel yokes for the compression tests on prisms, and of parts of the camera attachment;
- extensometer and Demec gauge readings, and operation of testing machine for the four tests in bending.
- modification to shorten the head of a ball socket for the camera attachment.

3.2 The Budd Polariscope.

A major tool for the performance of the experiments, the reflexion polariscope used was the "Large Field Meter, Model LF/MU" manufactured by the Instruments Division of the Budd Company. It is shown on fig. 3.1.

The accessories used for the experiments were:

- an oblique incidence attachment.
- a full wave plate and linear compensator attachment.

The telemiscrocope visible in fig. 3.2 was not used during the experiments; however, its base plate served as a support for a camera attachment that was built to make the photographic record of the fringe patterns easier and faster.

During the last stages of the work, the need of a larger oblique incidence attachment was felt, in order to obtain photographic records of fringe patterns, 4 in. x 4 in. in size, under oblique incident light.

Such an attachment was built; it consists of a trapezoidal plywood box containing two front faced mirrors.

Figures 3.4 and 3.5 show the details of that box, that was mounted on a separate stand.

The sensitivity of the polariscope is claimed to be of $\pm$ 2 degrees on the angle of the isoclinics, and of one percent of a fringe order. For a fringe value of about 0.001 in/in, this enables the measurement of strains within 10^{-5} in/in [Ref. 1.11, 1.17].

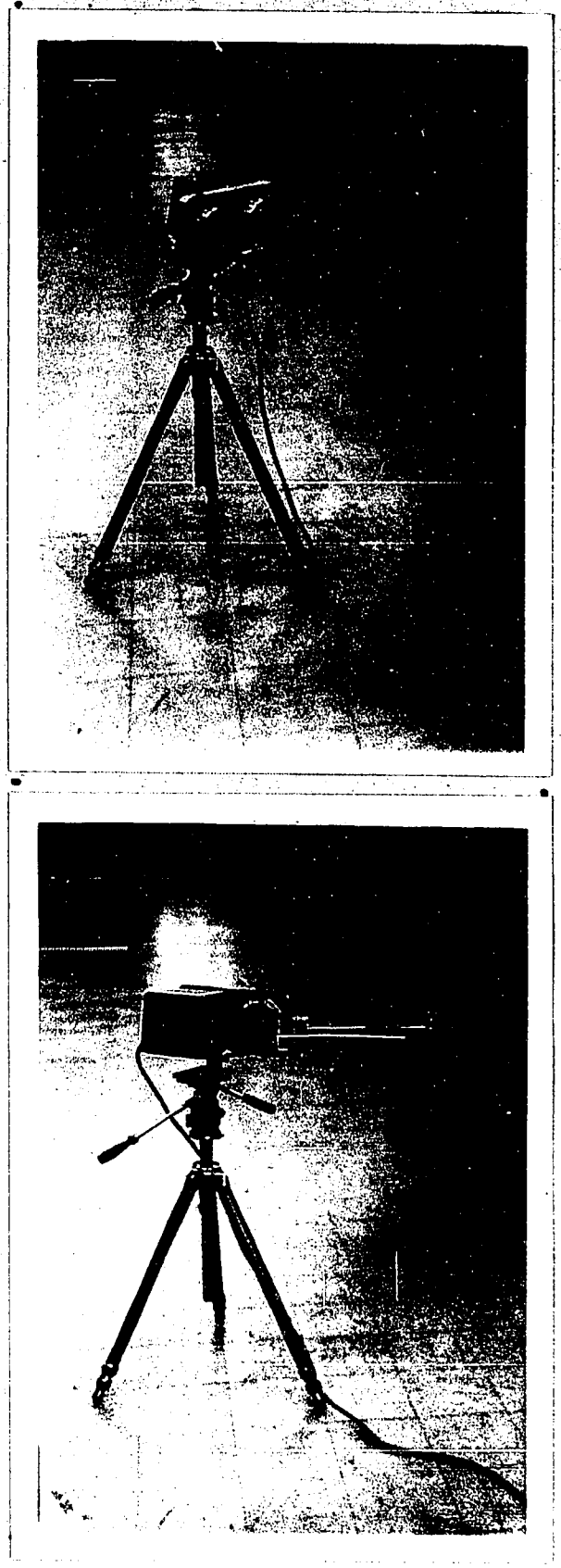

Fig. 3.1 The Budd Polariscope.

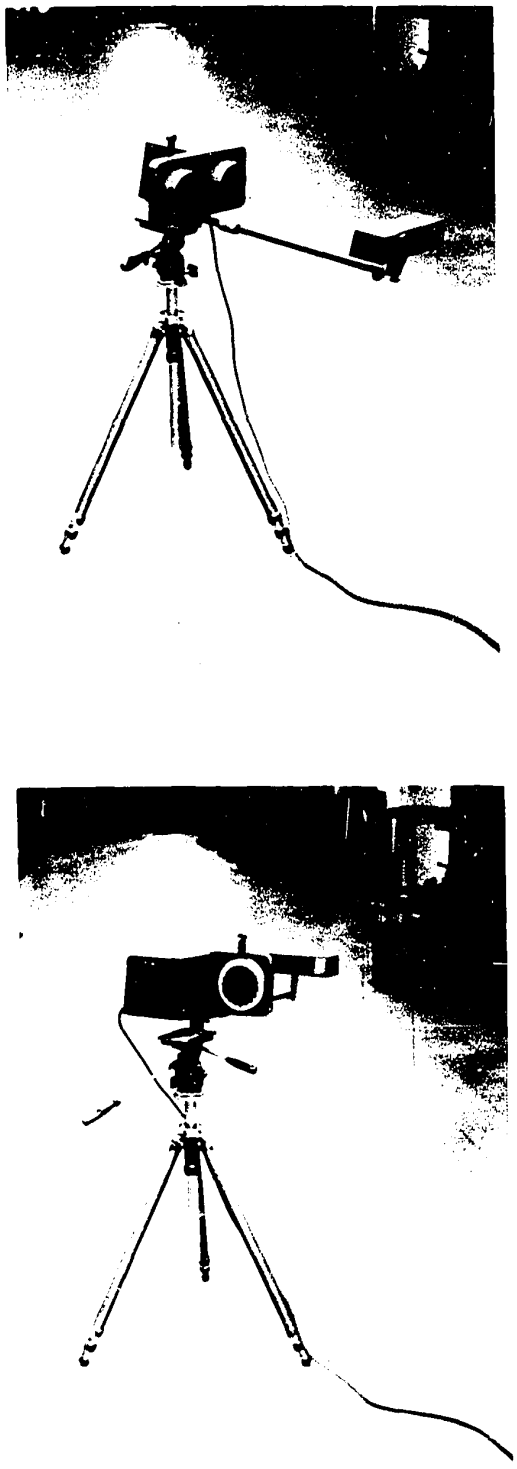

Fig. 3.1 The Budd Polariscope.

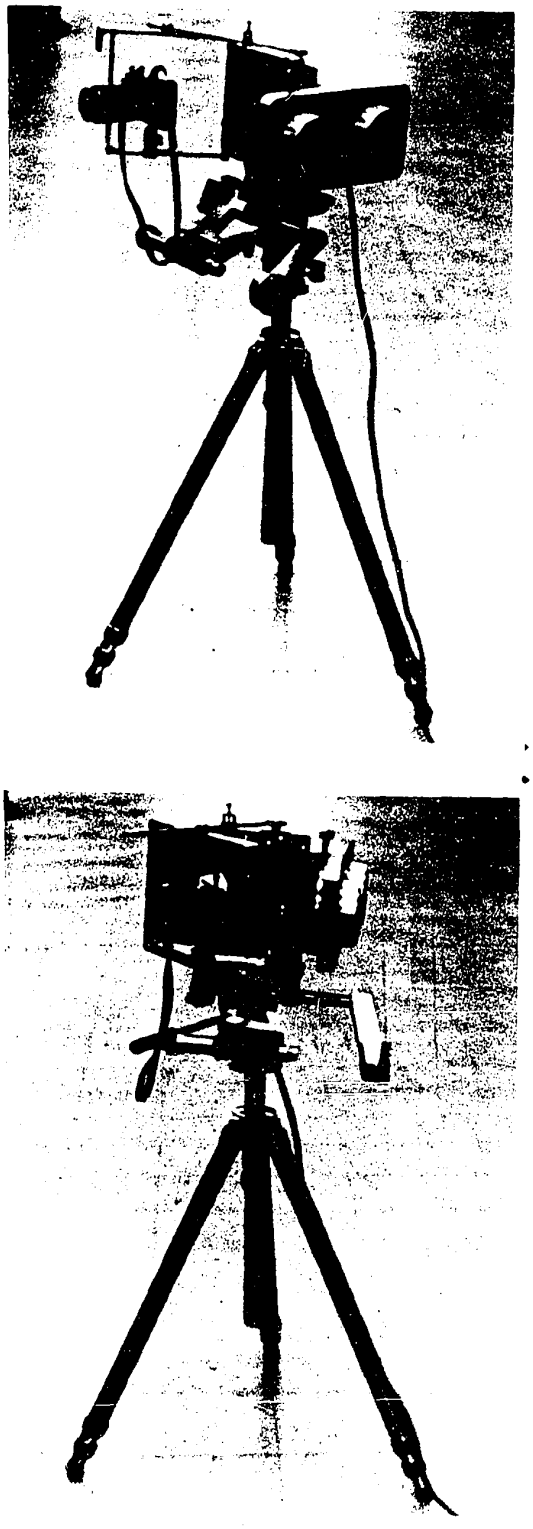

Fig. 3.2 The Budd polariscope and Camera attachment.

Fig. 3.3

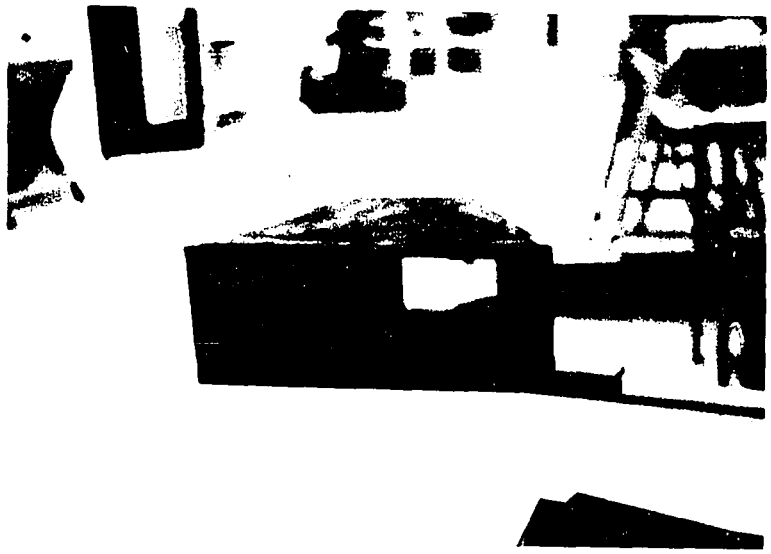

Fig. 3.4 The larger oblique incidence attachment.

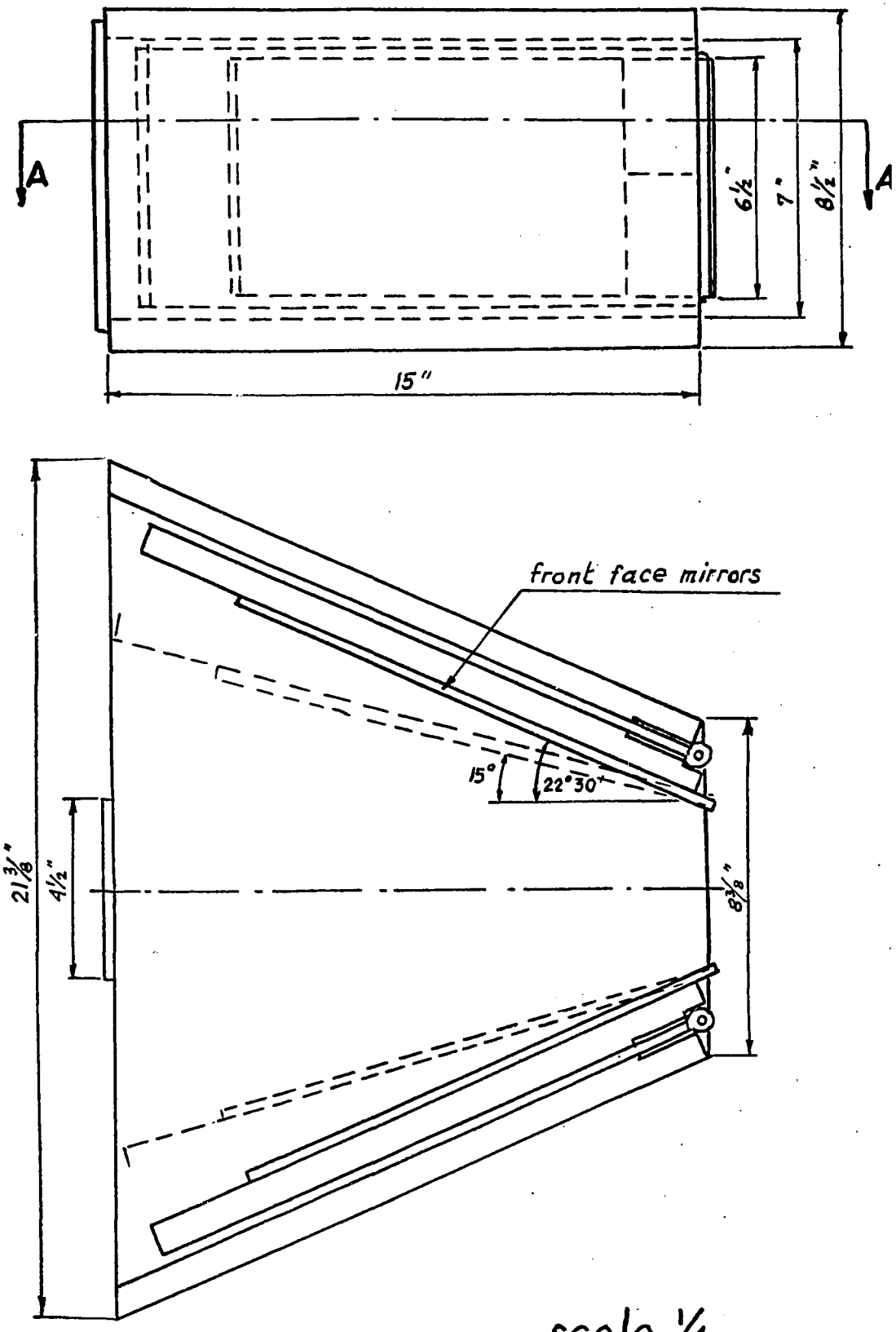

scale ¼

material: plywood, ¼" thick

Fig. 3.5. The larger oblique incidence attachment

elevation · cross section AA

3.3 Calibration tests.

The birefringent plastic used in all the experiments was supplied by the Budd Company, under the designation SC 10; it had the following characteristics:

strain optical coefficient K: about 0.10

modulus of elasticity : 480,000 psi

maximum elongation : 0.025 in/in.

It was shipped in flat sheets, 10 in. x 10 in. x .120 in. in size; altogether 200 square inches were used, from two separate sheets.

Samples from each sheet were submitted to a series of calibration tests in order to verify the value of K given by the manufacturer.

These tests were performed on steel or aluminium bars, to which the samples, 2 in. x 0.75 in., were bonded and which were submitted to bending or axial load.

A load-fringe order curve was drawn in each case, from which K was determined. (figs 3.7 to 3.10).

The curves obtained have always been perfectly straight lines; the maximum fringe order reached was close to 4 .

Similar tests were also performed

- to acquire proficiency in the readings and in the use of the polariscope,
- to check the quality of the bond between plastic and metal, and thus the adequacy of bonding procedures,
- to measure the intensity of light passing through the analyser, for the future choice of films, shutter speeds and diaphragm openings,
- to determine the behaviour of the plastic under sustained load.

For this purpose, a sample of the plastic was glued to the tension face of an aluminium cantilevered bar which was left under load for 24 hours.

The fringe order was then close to 5, and the descending branches of the load-fringe order curves, both for normal and oblique incidences were found to superimpose to the ascending ones, to within the sensitivity of 1 or 2% mentioned above.

For cantilevered bars, b inches wide, and h inches thick, subjected to a load P located at a distance l from the centre of the sample, the value of k is given from equations (1.23), (1.43) and (1.44) by [Ref 1.17]

$$K = \frac{n_n}{p} \cdot \frac{\lambda\, b\, h^2}{12\, t\, R\, l} \cdot \frac{E_s}{1+\nu_s} \quad ,$$

where n_n/P is the inverse of the slope of the calibration curve, and $\lambda = 22.7 \times 10^{-6}$ in. is the wave length at the tint of passage.

For tension tests, the corresponding formula reads

$$K = \frac{n_n}{p} \cdot \frac{\lambda\, b\, h}{2\, t\, R} \cdot \frac{E_s}{1+\nu_s}$$

whereas the fringe value is given in all cases by $F = \lambda/2\ t\ K\ R$.

Fig 3.6 shows the set up of the cantilever tests; Table 3.1 is a survey of the principal data relevant to each test, and figs 3.7 to 3.10 are the load-fringe order diagrams.

TABLE 3.1

Calibration tests.

Test number	1	2	3	4
sheet number	1	1	2	2
type of test	(1)	(2)	(1)	(1)
material	Steel	Alu.	Steel	Alu.
E (in. 10^6 psi)	29.0	10.5	29.0	10.4
ν	0.30	0.30	0.30	0.30
width b (in.)	0.99	1.00	0.99	1.00
thickness h (in.)	0.244	0.184	0.249	0.247
distance 1 (in.)	12.0	—	12.0	12.0
t (in.)	0.121	0.121	0.121	0.121
thickness of plastic and adhesive (in.)	0.126	0.26(3)	0.121	0.127
R [Ref 1.17]	1.43	0.984	1.408	1.285
n_n/P	0.0925	0.769	0.0849	0.228
K experimental	0.110	0.108	0.107	0.113
K (average)	0.109		0.110	
K given	0.101		0.104	
discrepancy in %	8		6	
fringe value ($F \times 10^3$)	0.602	0.875	0.605	0.664
F for $R = 1$ ($F \times 10^3$)	0.860	0.860	0.852	0.852

Code:

(1) Bending on cantilever
(2) Tension test
(3) Plastic was glued on both faces for symmetry.

Fig. 3.6 Set up for cantilever calibration test.

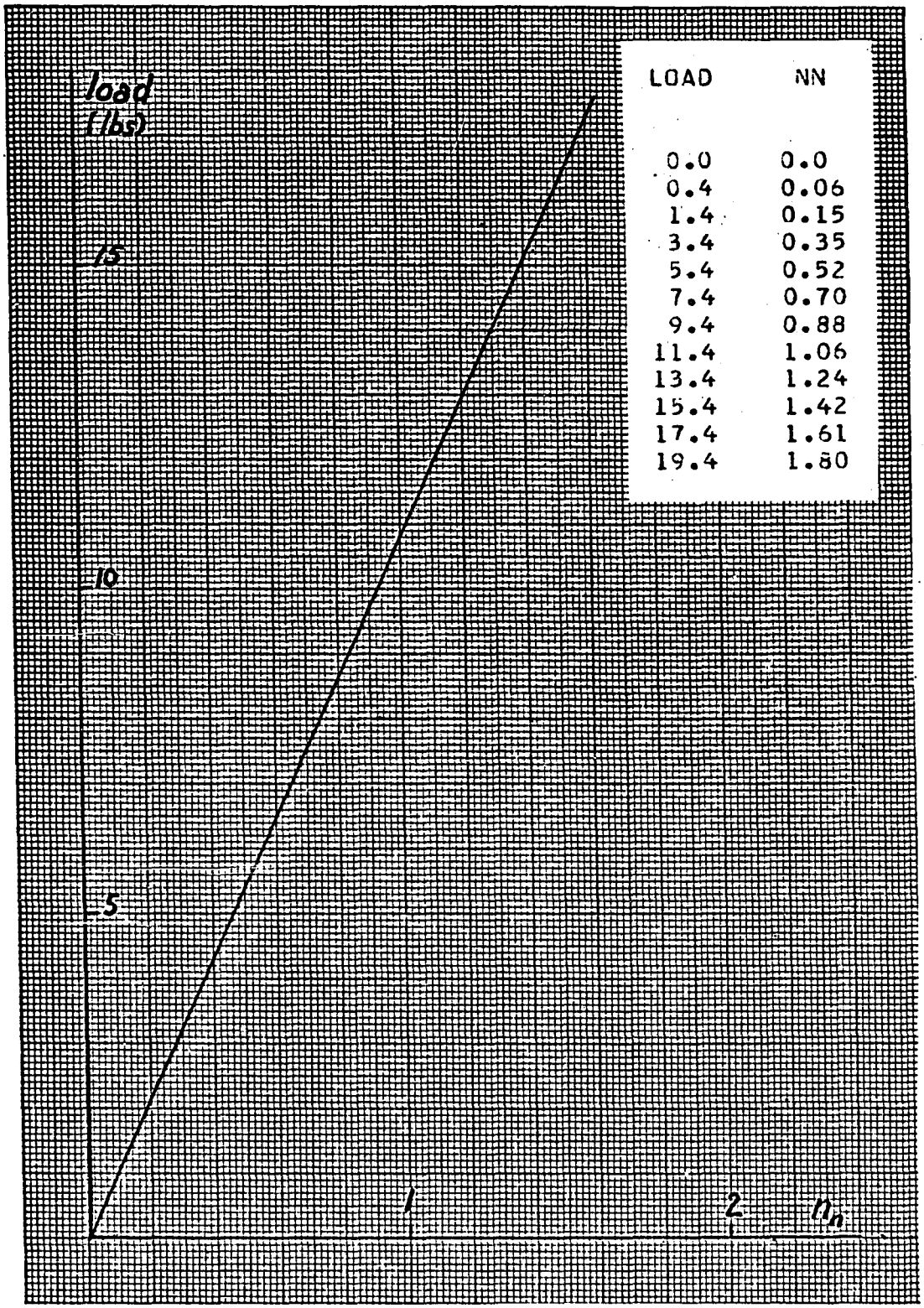

LOAD	NN
0.0	0.0
0.4	0.06
1.4	0.15
3.4	0.35
5.4	0.52
7.4	0.70
9.4	0.88
11.4	1.06
13.4	1.24
15.4	1.42
17.4	1.61
19.4	1.80

Fig. 3.7 Test No. 1. Load $-n_n$ curve.

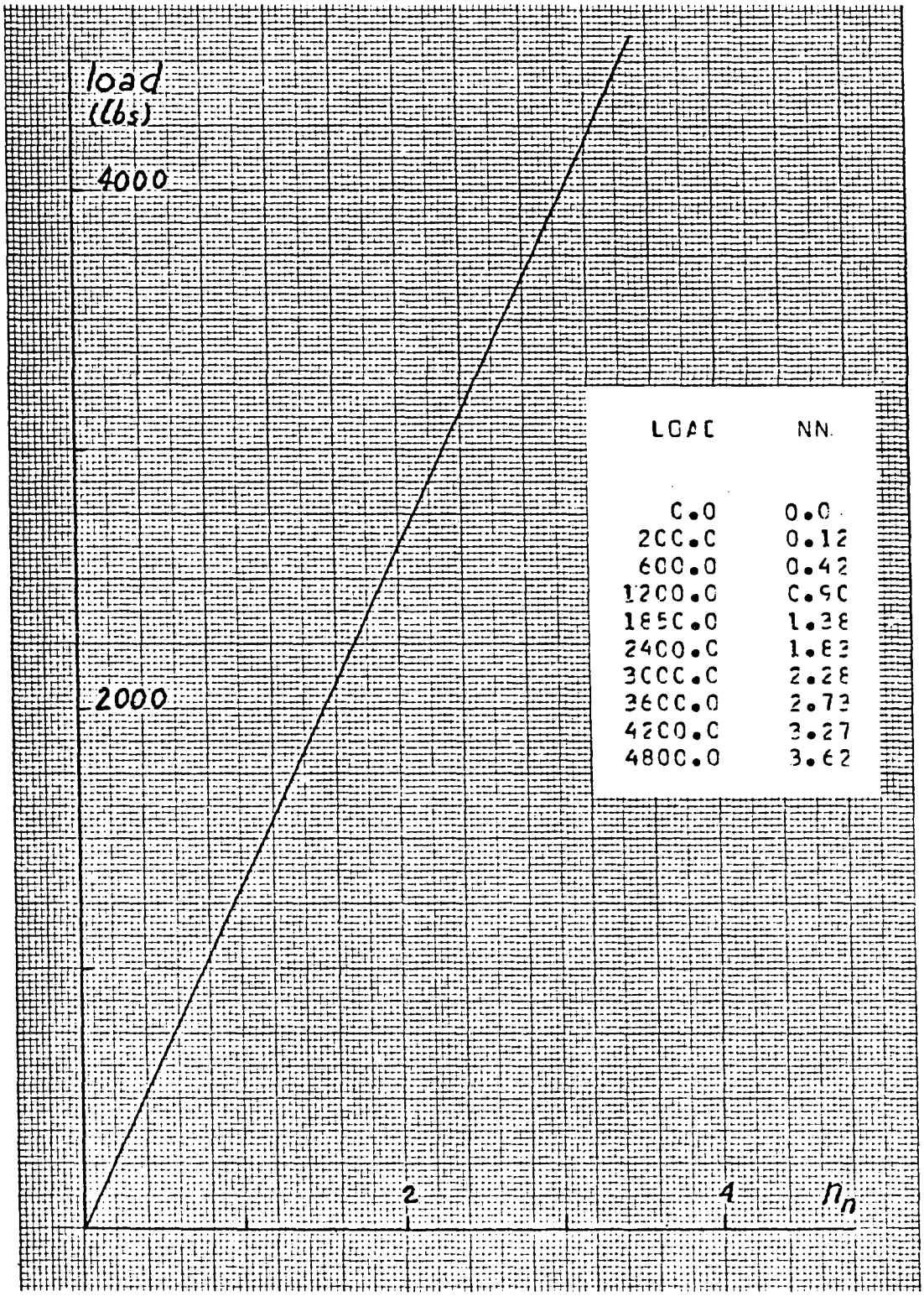

Fig. 3.8 Test No. 2 . Load $-n_n$ curve.

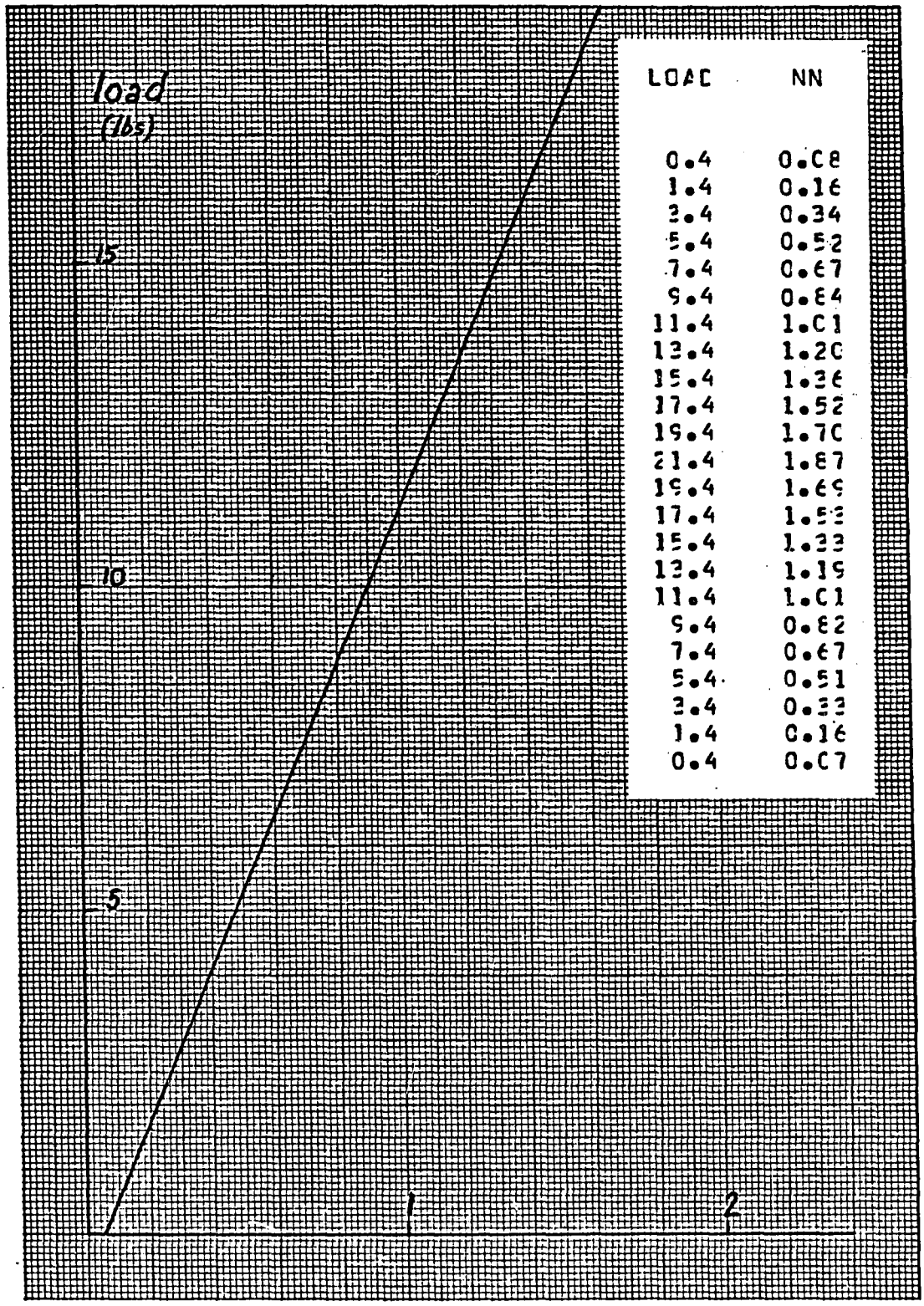

Fig. 3.9 Test No. 3. Load $-n_n$ curve.

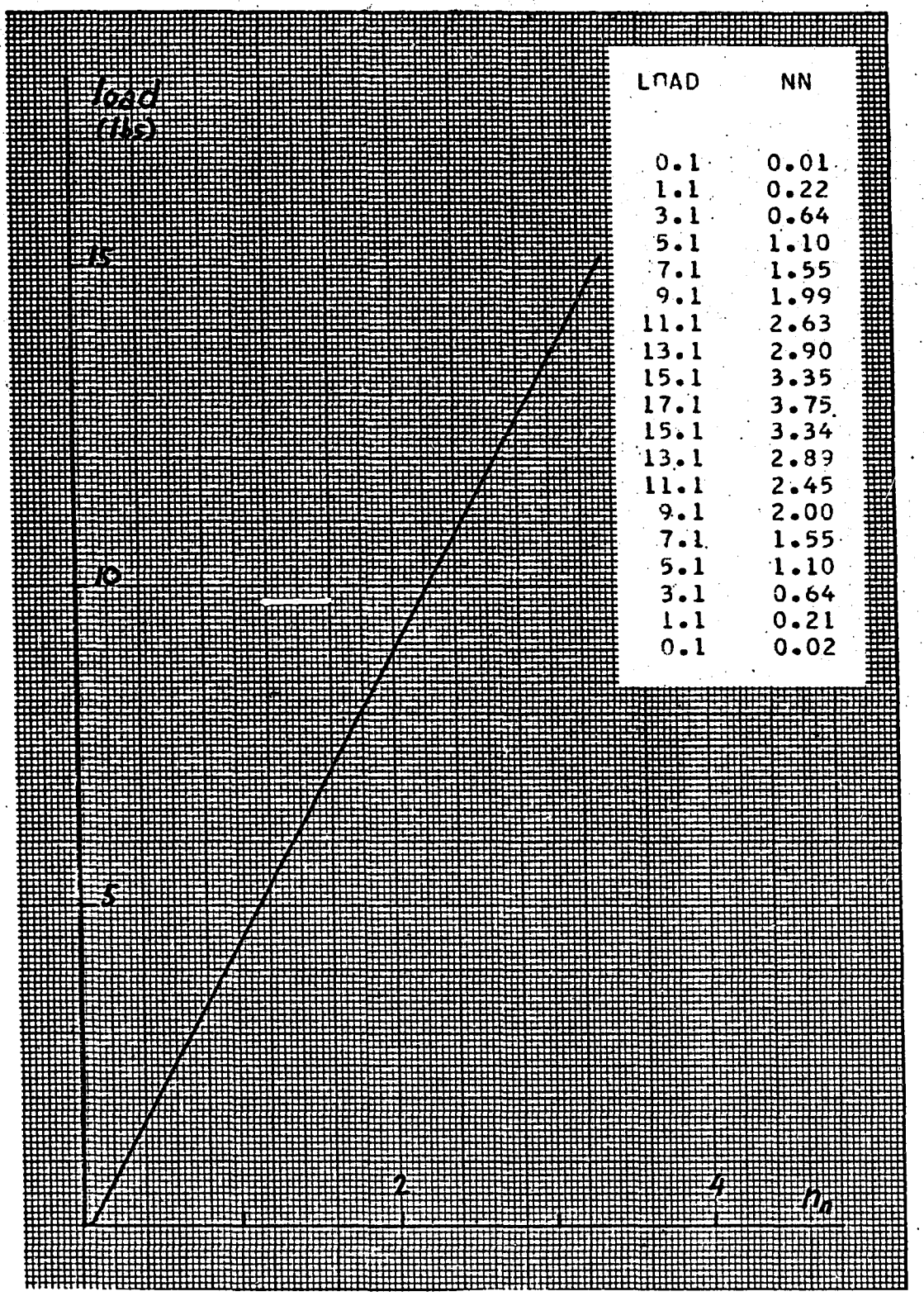

LOAD	NN
0.1	0.01
1.1	0.22
3.1	0.64
5.1	1.10
7.1	1.55
9.1	1.99
11.1	2.63
13.1	2.90
15.1	3.35
17.1	3.75
15.1	3.34
13.1	2.89
11.1	2.45
9.1	2.00
7.1	1.55
5.1	1.10
3.1	0.64
1.1	0.21
0.1	0.02

Fig. 3.10 Test No. 4 . Load -n_n curve.

3.4 Tests on prisms in axial compression.

The next part of the experiments consisted of testing to failure the four mortar prisms.

Mortar was chosen instead of concrete in order to avoid parasitic fringes due to stress concentrations around the aggregates. [Ref 1.12].

The prisms were cast horizontally, side by side, in a plywood form, and compacted by means of a pneumatic vibrator.

Each batch contained the following:

Silica sand Nos. 10 and 16	:	3 lbs of each;
Silica sand Nos. 24 and 35	:	3.75 lbs of each;
Silica sand No. 70	:	1.50 lb
High Early strength Cement	:	4.62 lbs
Water	:	1400 cc.

A few hours after pouring, the form was wrapped in burlap, and kept moist for 72 hours; it was then dismantled, and the prisms were immersed in water for 7 days.

They were capped with a molten sulphur-carbon compound, and tested at ages varying from 104 to 273 days.

One piece of plastic, 2 in. x 4 in., was glued to each prism.

Cutting it to size was done by hand with a light jig saw, after the sheet of plastic had been clamped onto a wooden board, on both sides of a groove.

All faces in contact with the birefringent material were covered with drafting tape to avoid scratching it.

Surface preparation of the plastic consisted of cleaning it with acetone, and then with a dry cotton swab; the surface of the concrete was first roughened with sand paper, then air blasted.

The adhesive was obtained from the Budd Company, and has the designation 4HRCT; it is a low viscosity reflective cement to be mixed with 15% in weight of hardener, and has a curing time of 4 hours, at room temperature.

The dial gauges were located on either side of the front face of the prisms, to which the plastic was glued, and at the middle of the back face.

The points of measurement were thus located in plan at the apexes of an equilateral triangle.

The tests were performed on a hydraulic testing machine, of which one head contained a ball socket packed with grease.

Nonetheless, centering of the prism was a lengthy and tedious trial and error procedure.

As soon as contact between the head of the machine and the top face of the prism was established, the socket was blocked in its position and no adjustment took place.

A small load was applied; if the readings of the three dial gauges were not of the same order of magnitude, the load had to be removed and the prism, or the head, readjusted for another trial.

If they were comparable, then another small increment of 2000 lbs would be applied, as a check, and the test would start from there.

In order to separate the principal strains, using formulae (1.10) and (1.11), a short program called FOTSTRES was written.

A listing may be found at the following pages.

FOTSTRES can give the strains at a maximum of 20 points, subjected to 30 loading stages. The input consists essentially of the fringe value, and of rectangular matrix [A (I,J)], where

I is three times the total number of points, and

J is the number of loads considered.

X being the number of a point, ($3X \leq I$), the lines $3X-2$, $3X-1$, and $3X$ of the matrix contain respectively:

- all the successive values of the load, including the initial value
- all the successive values of n_n, in the same order,
- all the successive values of n_o, at point X.

The output consists of a table of five columns, containing respectively, the values of the load, n_n, n_o, strain A and strain B.

By convention, strain A is parallel to the analyser handle of the polariscope.

An additional print-out of some of the intermediate stages of the computation may be specified for checking purposes.

Tables 3.2 to 3.6 give the print out relative to each of the tests, figs 3.13 to 3.18 give the stress-strain curves for each test.

Each prism tested had particular features:

Prism No.1.

Each extensometer was bolted to a small tee glued to the mortar by means of epoxy resin; so was the angle on which the tip was supported, as shown on fig 3.11 .

Both parts were cemented to the mortar over an area of 2 x 2 sq. in. at four inches from each other, so that the actual gauge length could not be obtained accurately : it was between 4 and 8 inches.

Both extreme cases were considered, and the corresponding strains were calculated and plotted.

A hysteresis cycle was first done, up to 60% of ultimate; (fig 3.14, table 3.2); then only the prism was tested to failure (table 3.3, fig 3.15).

Fig 3.13 shows the readings on the three dials as an indication of the good centering achieved.

Prisms Nos. 2,3,4.

In order to avoid the difficulty encountered with prism No.1, a new set up was developed for the extensometers (fig 3.12).

It consists of two yokes secured to the concrete by three screws with sharp ends, and to which the extensometers were connected by small, tightly screwed angles.

The gauge length was thus clearly defined, as the distance between the two screws located on the front face.

The average of the readings on the two lateral extensometers was used to plot the graphs.

Prisms 3.

Here, the plastic was glued transversally in order to examine possible edge effects along the sides.

By extending the plastic 1/8" beyond the edges of the prism, it was possible to concentrate the edge effect "outside" the front face.

On the other hand, the effect at the horizontal edges of the plastic was found to extend well into the plastic, to the point that readings at the central point were difficult; this suggests that plastic surfaces be extended by one inch beyond the area of interest, in the direction of the load.

Tables 3.4 to 3.6 and figs 3.16 to 3.18 are related to the tests on prisms 2,3 and 4.

```
//FOTSTRES    JOB  (F119,000,001,025,150,01),'.J.C.MAMET.

    DIMENSION A(6C,3C),DELNN(30),DELNC(30),CELSTR(30),STRENA(30),
   1DELNM(3C),DELSTP(3C),STRENB(30)
    WRITE (6,1C1)
101 FORMAT (1H1,'PHOTCSTRESS TECHNICUE  PRINCIPAL STRAINS')
20C READ (5,1C2) K,L,R
1C2 FORMAT (2I8,E13.4)
    WRITE (6,103) K,L,R
103 FORMAT (1H ,//' NC CF PCINTS   NC CF LCADS   FRINGEVALUE'/I9,I16,
   1E17.4)
    IF(K-1) 2C4,2C4,2C5
2C5 DO 2C2 M=1,K
    WRITE (6,1C9) M
1C9 FORMAT (1H ,//' PCINT ',I4)
2C4 READ (5,1C4) ((A(I,J),J=1,L),I=1,3)
1C4 FORMAT (9F8.2)
    DO 2C1 J=1,L
    DELNM(J) =C.C
    DELNN(J) =C.C
    DELNO(J) =C.C
    DELSTP(J) = C.C
    DELSTR(J) = C.C
    STRENA(J) = C.C
2C1 STRENB(J) = C.C
    DO 2C3 J=2,L
    DELNM(J) = 1.C2 * (A(2,J)-A(2,J-1))
    DELNN(J) = 2.C2 * (A(2,J)-A(2,J-1))
    DELNO(J) = 1.51 * (A(3,J)-A(3,J-1))
    DELSTP(J) = DELNC(J) - DELNM(J)
    DELSTR(J) = DELNC(J) - DELNN(J)
    STRENA(J) = STRENA(J-1) + R*DELSTP(J)
    STRENB(J) = STRENB(J-1) + R*DELSTR(J)
2C3 CONTINUE
    WRITE (6,1C7)
1C7 FORMAT (1H ,//'     LCAD      NN       NC        STRENA          STREN
   1'//)
    DO 2C2 J=1,L
    WRITE (6,1C8) (A(I,J),I=1,3),STRENA(J),STRENB(J)
1C8 FORMAT (1H ,F8.1,2F8.2,2E14.4)
2C2 CONTINUE
    GO TO 2CC
    END
```

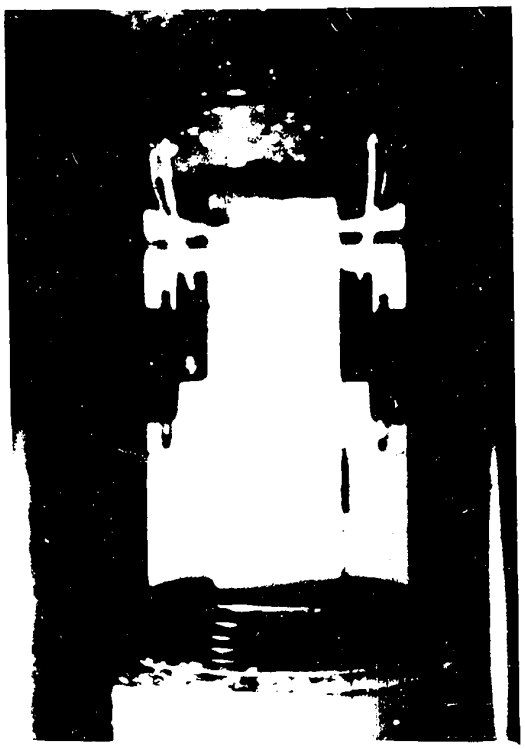

Fig. 3.11 Compression test. Prism No. 1.

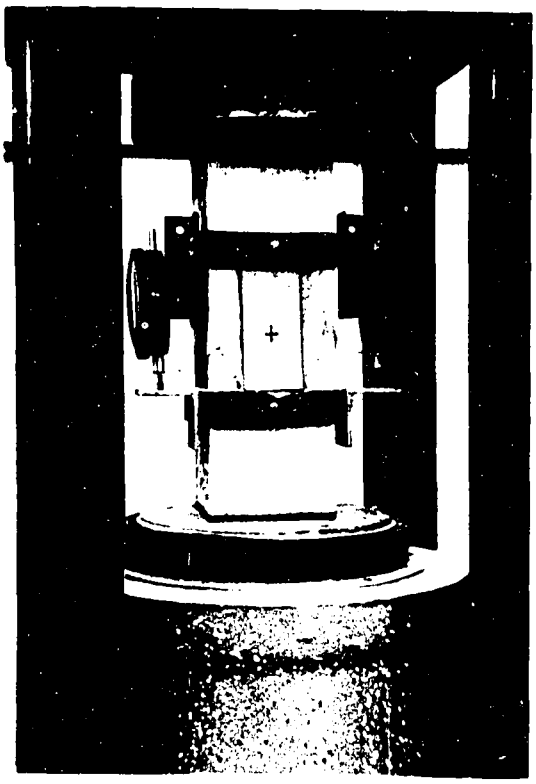

Fig. 3.12 Compression tests. Prisms No. 2,3,4 .

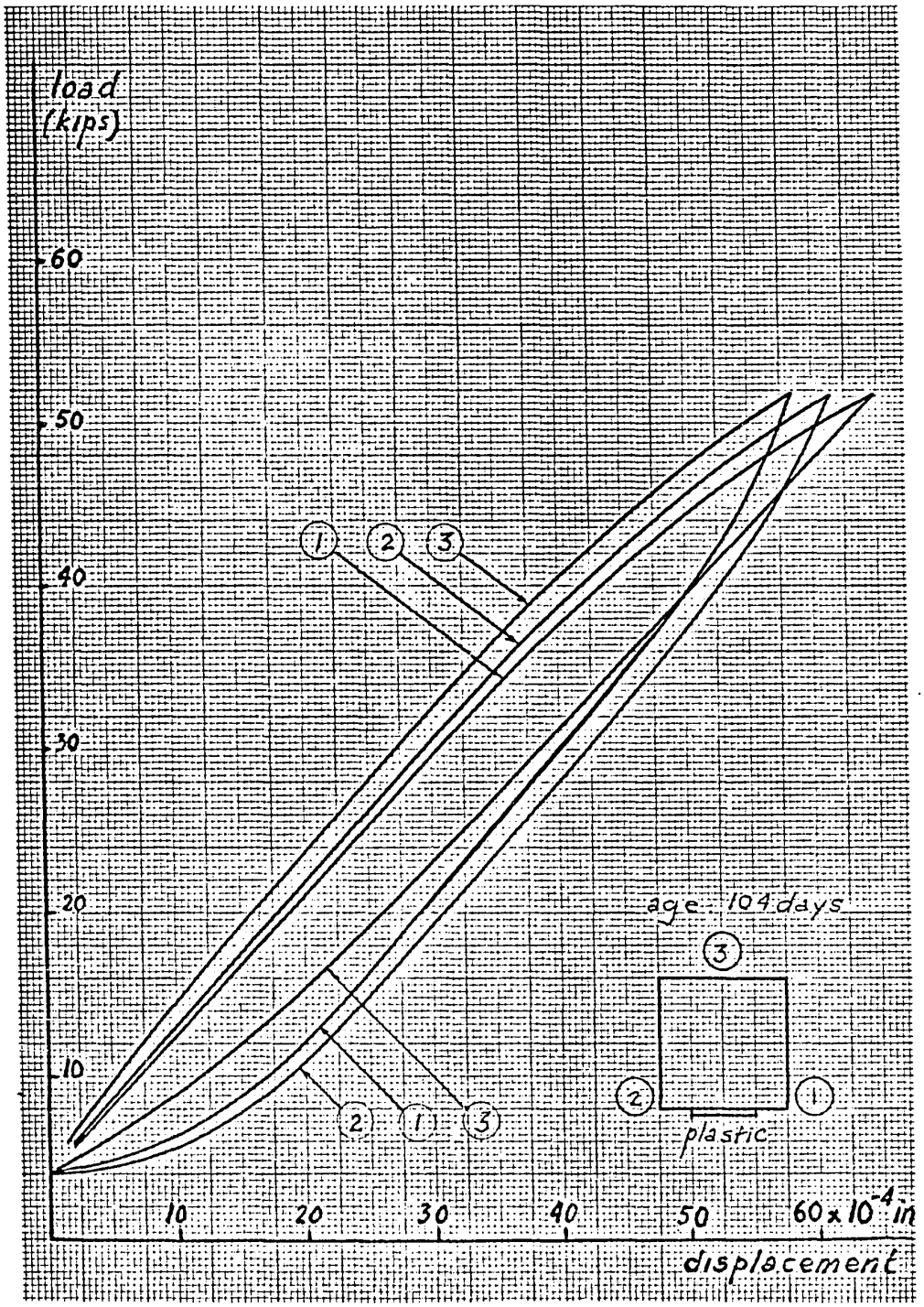

Fig. 3.13. Prism No. 1 - Dial gauge readings.

NC CF PCINTS	NO CF LCADS	FRINGEVALLE
1	25	C.86CCE-03

LOAC	NN	NO	STRENA	STRENB
8CCC.0	-0.26	-C.62	C.C	C.0
12C00.0	-0.36	-C.74	-C.6811E-04	0.1789E-04
16CCC.0	-0.44	-C.79	-C.6287E-04	C.9193E-04
20C00.0	-0.51	-C.9C	-C.1443E-03	0.7069E-04
24CCC.0	-0.5E	-1.C2	-C.2387E-C3	C.3646E-04
284C0.C	-0.72	-1.1E	-C.3237E-C3	C.7190E-04
32100.0	-0.E4	-1.3C	-C.3743E-C3	C.1245E-03
36CC0.C	-0.93	-1.41	-C.4382E-03	C.1380E-03
404C0.C	-1.C4	-1.57	-C.5495E-C3	C.1213E-03
436CC.0	-1.12	-1.7C	-C.6481E-03	C.9150E-04
478C0.C	-1.24	-1.E4	-C.7246E-C3	C.1182E-03
522CC.C	-1.41	-2.C5	-C.8482E-C3	C.1408E-03
48CC0.0	-1.3E	-2.C1	-C.8226E-C3	C.1406E-03
436CC.C	-1.2E	-1.E9	-C.772CE-03	C.8798E-04
40C0C.0	-1.2C	-1.EC	-C.7C78E-03	C.1006E-03
36CCC.C	-1.12	-1.69	-C.6351E-C3	C.1045E-03
32CC0.C	-1.C4	-1.53	-C.4975E-C3	C.1733E-03
28CC0.C	-0.95	-1.4E	-C.5115E-C3	C.8187E-04
24CC0.C	-0.87	-1.39	-C.4648E-C3	C.5977E-04
20CC0.0	-0.75	-1.24	-C.3753E-C3	C.4610E-04
16CC0.C	-C.6E	-1.13	-C.2939E-C3	0.6734E-04
12CC0.0	-0.59	-1.C1	-C.217CE-C3	C.6682E-04
8C0C.0	-0.44	-C.92	-C.2317E-03	-C.7688E-04
4CCC.0	-0.37	-C.7E	-C.1113E-C3	-C.1668E-04
0.0	-0.17	-C.62	-C.7E95E-C4	-0.1563E-03

Table 3.2 Hysteresis cycle. Prism No. 1 .
Principal strains.

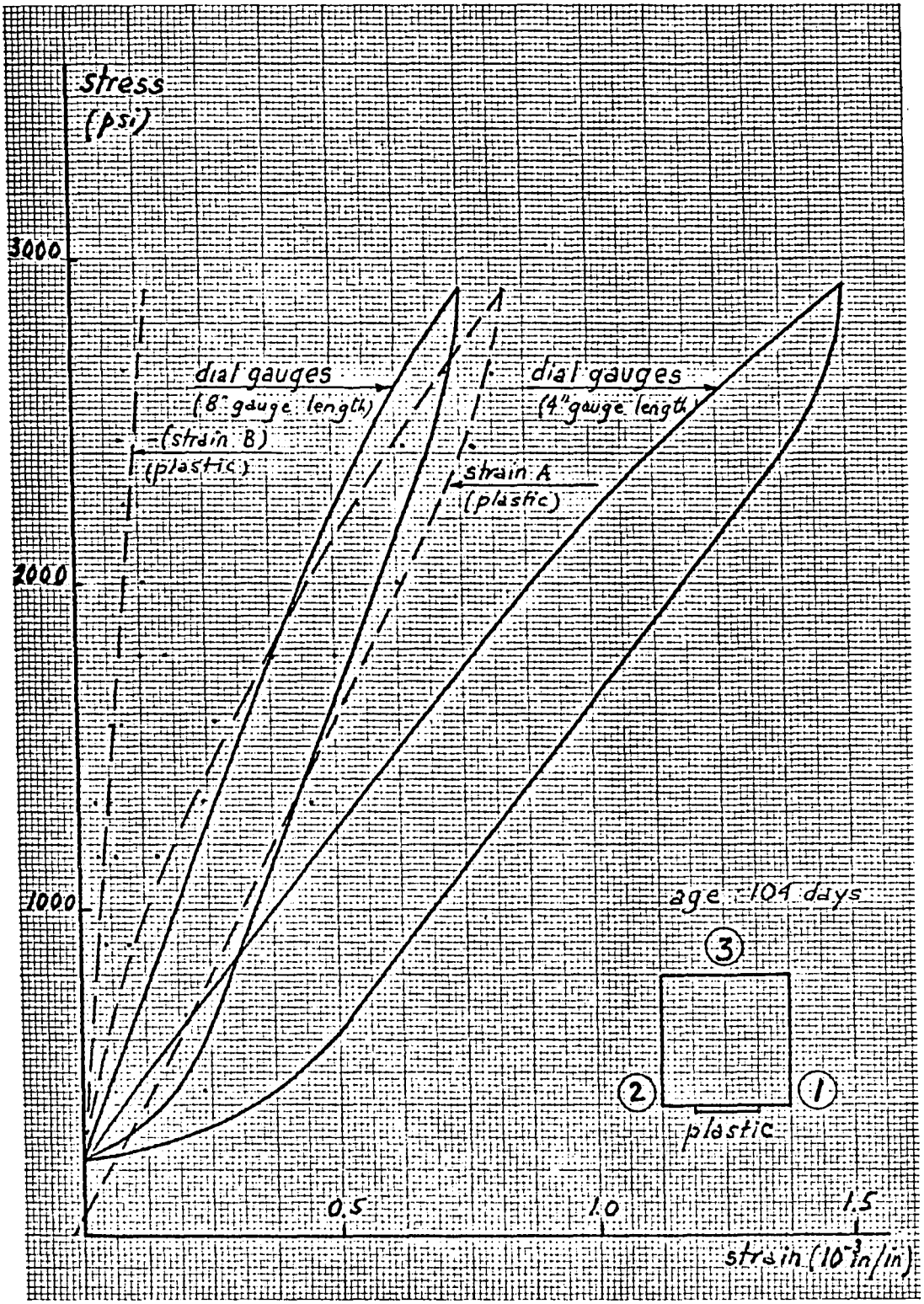

Fig. 3.14 Prism No. 1 - Hysteresis cycle. Stress strain curves.

NO OF POINTS	NO OF LOADS	FRINGEVALUE
1	19	0.8600E-03

LOAD	NN	NO	STRENA	STRENB
800.0	-0.25	-0.52	0.0	0.0
4000.0	-0.25	-0.63	-0.1428E-03	-0.1428E-03
8000.0	-0.36	-0.69	-0.1243E-03	-0.2967E-04
12000.0	-0.42	-0.80	-0.2145E-03	-0.6828E-04
16000.0	-0.52	-0.91	-0.2696E-03	-0.3741E-04
20200.0	-0.60	-1.02	-0.3423E-03	-0.4123E-04
24000.0	-0.68	-1.12	-0.4020E-03	-0.3216E-04
28000.0	-0.80	-1.26	-0.4785E-03	-0.5503E-05
32000.0	-0.89	-1.37	-0.5424E-03	0.7998E-05
36000.0	-0.99	-1.44	-0.5456E-03	0.9082E-04
40400.0	-1.08	-1.56	-0.6225E-03	0.9133E-04
44200.0	-1.17	-1.68	-0.6994E-03	0.9185E-04
48000.0	-1.31	-1.84	-0.7843E-03	0.1273E-03
52200.0	-1.42	-2.02	-0.9216E-03	0.8462E-04
56000.0	-1.59	-2.18	-0.9802E-03	0.1722E-03
60000.0	-1.82	-2.46	-0.1142E-02	0.2081E-03
64200.0	-2.05	-2.72	-0.1278E-02	0.2700E-03
68000.0	-2.38	-3.18	-0.1586E-02	0.2460E-03
75000.0	-2.88	-3.70	-0.1823E-02	0.4393E-03

Table 3.3 Prism No. 1 up to failure. Principal strains.

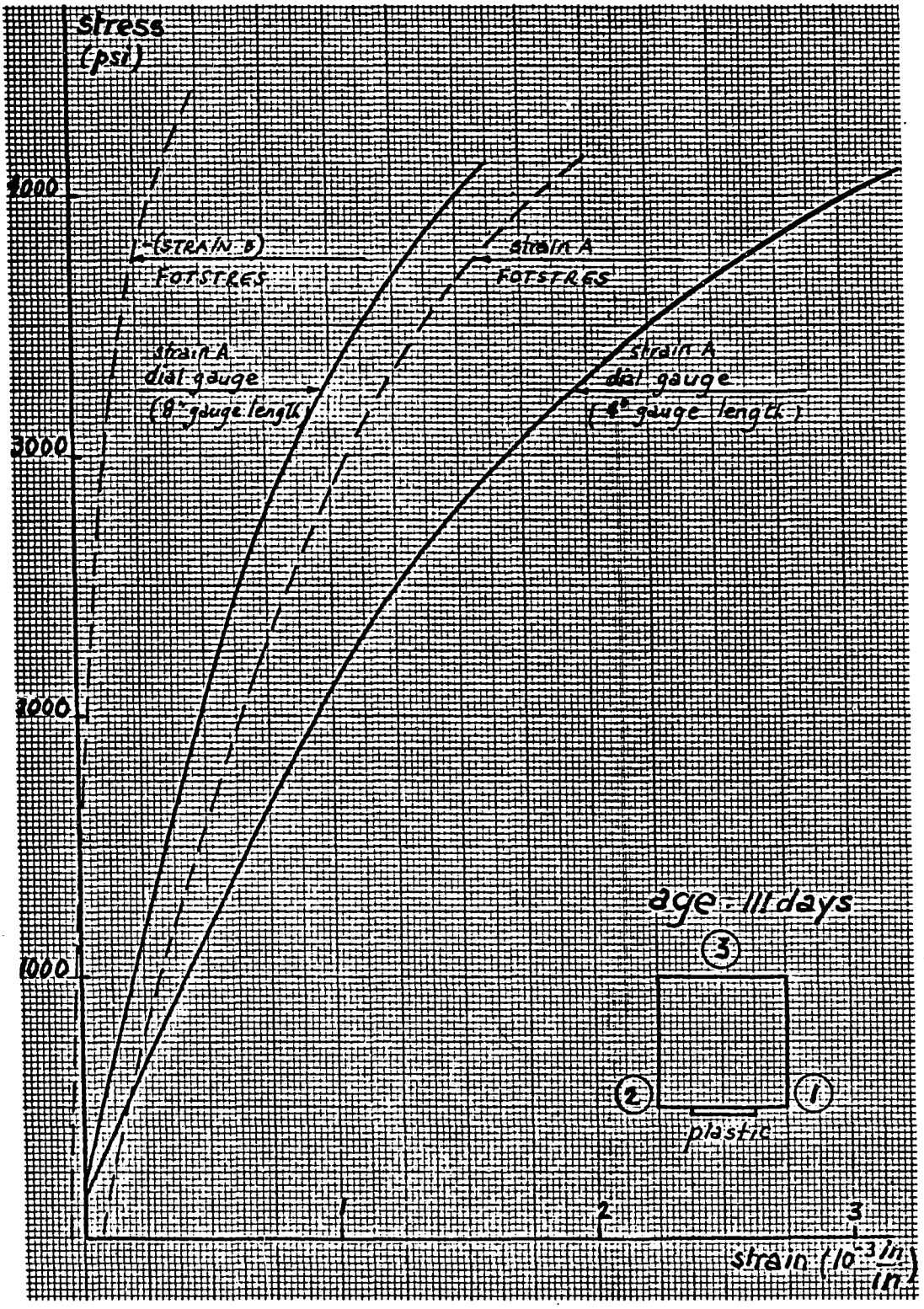

Fig. 3.15 Prism No. 1 up to failure. Stress-strain curve.

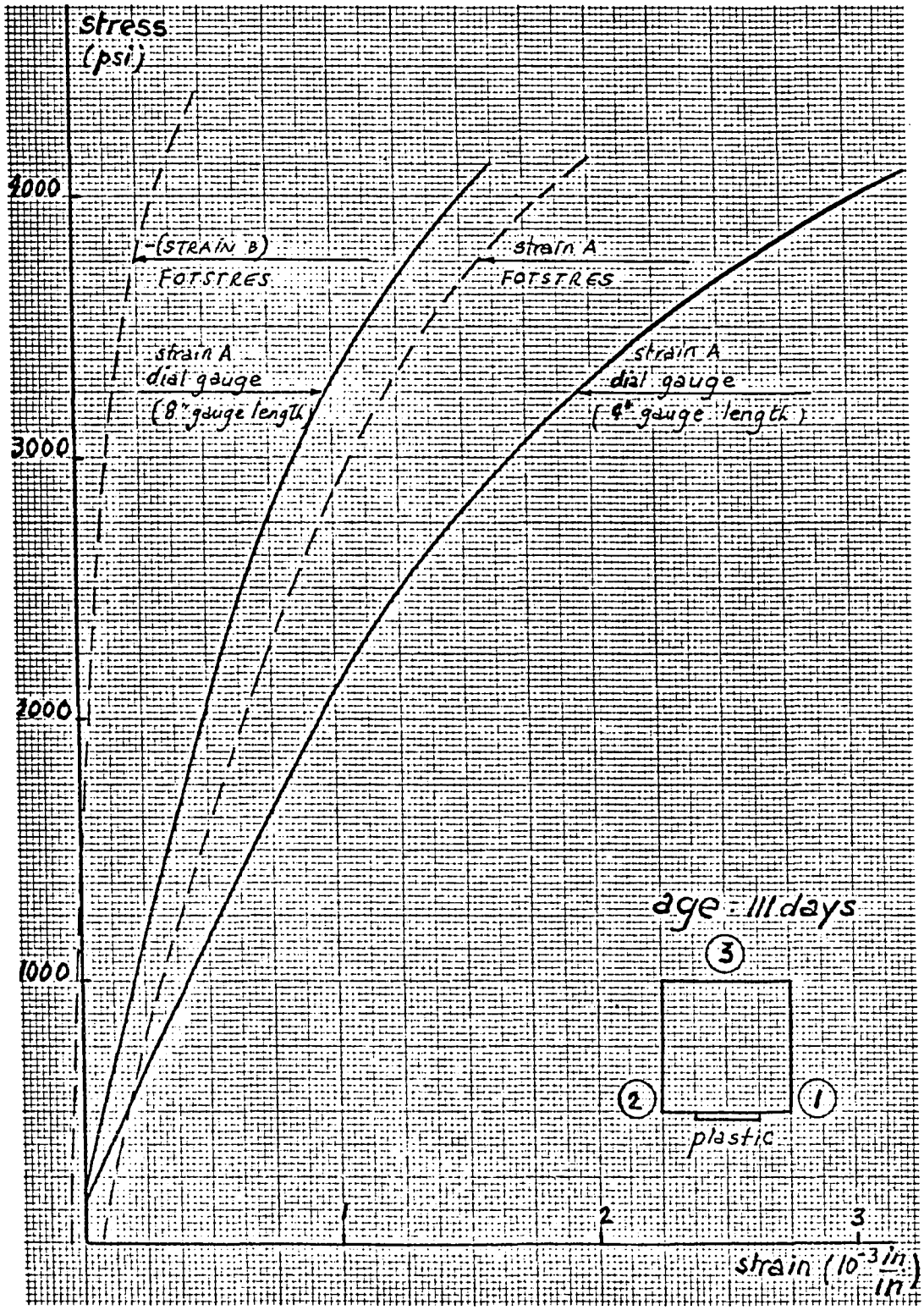

Fig. 3.15 Prism No. 1 up to failure. Stress-strain curve.

NO OF POINTS	NO OF LOADS	FRINGEVALUE
1	20	0.8600E-03

LOAD	NN	NO	STRENA	STRENB
800.0	0.0	-0.55	0.0	0.0
2000.0	-0.08	-0.61	-0.7740E-05	0.6106E-04
4000.0	-0.10	-0.68	-0.8110E-04	0.4902E-05
6000.0	-0.12	-0.74	-0.1415E-03	-0.3827E-04
12000.0	-0.24	-0.92	-0.2700E-03	-0.6355E-04
18000.0	-0.39	-1.09	-0.3591E-03	-0.2373E-04
24000.0	-0.56	-1.22	-0.3788E-03	0.1028E-03
30000.0	-0.68	-1.36	-0.4554E-03	0.1294E-03
36000.0	-0.82	-1.57	-0.6053E-03	0.9993E-04
42000.0	-1.04	-1.77	-0.6720E-03	0.2224E-03
48000.0	-1.23	-2.08	-0.9079E-03	0.1499E-03
54000.0	-1.45	-2.27	-0.9616E-03	0.2853E-03
60000.0	-1.65	-2.57	-0.1176E-02	0.2432E-03
66000.0	-1.86	-2.93	-0.1459E-02	0.1405E-03
72000.0	-2.22	-3.22	-0.1520E-02	0.3893E-03
75000.0	-2.42	-3.50	-0.1708E-02	0.3732E-03
78000.0	-2.70	-3.76	-0.1800E-02	0.5219E-03
81000.0	-2.86	-3.98	-0.1945E-02	0.5142E-03
84000.0	-3.12	-4.19	-0.1990E-02	0.6932E-03
87000.0	-3.40	-4.45	-0.2082E-02	0.8419E-03

Table 3.4 Prism No. 2. Principal strains.

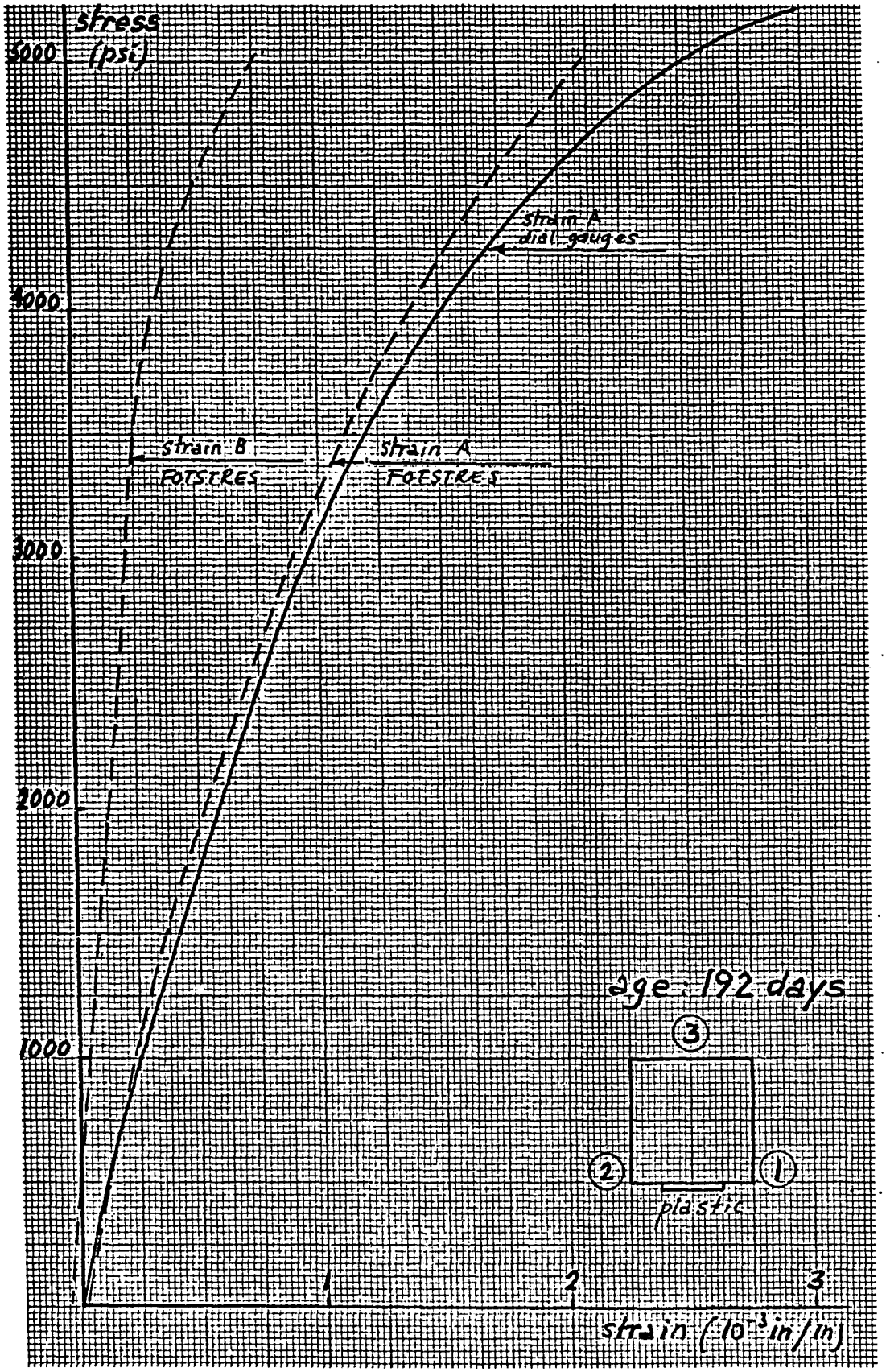

Fig. 3.16 Prism No. 2 . Stress-strain curve.

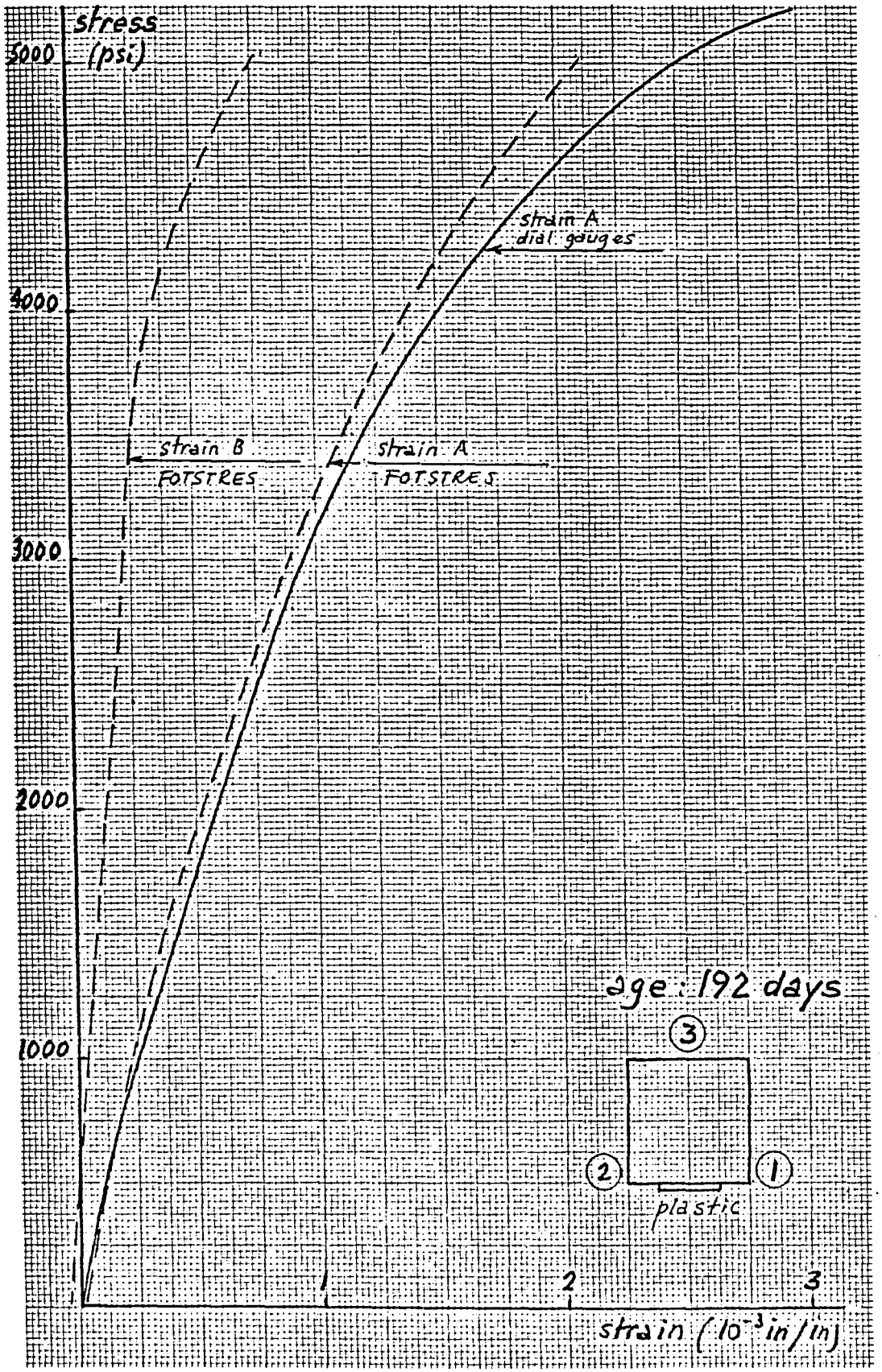

Fig. 3.16 Prism No. 2 . Stress-strain curve.

NO OF POINTS	NO OF LOADS	FRINGEVALUE
1	15	0.9600E-03

LOAD	NN	NO	STRENA	STRENB
2000.0	0.0	-0.68	0.0	0.0
6000.0	-0.15	-0.81	-0.3724E-04	0.9176E-04
12000.0	-0.30	-1.03	-0.1913E-03	0.6665E-04
18000.0	-0.48	-1.30	-0.3841E-03	0.2873E-04
24000.0	-0.65	-1.48	-0.4687E-03	0.9030E-04
30000.0	-0.80	-1.65	-0.5579E-03	0.1301E-03
36000.0	-0.88	-1.74	-0.6046E-03	0.1522E-03
42000.0	-1.05	-2.00	-0.7931E-03	0.1099E-03
48000.0	-1.25	-2.28	-0.9813E-03	0.9374E-04
54000.0	-1.52	-2.53	-0.1069E-02	0.2381E-03
60000.0	-1.73	-2.70	-0.1106E-02	0.3822E-03
66000.0	-2.08	-3.13	-0.1357E-02	0.4318E-03
73000.0	-2.32	-3.58	-0.1731E-02	0.2644E-03
78000.0	-2.86	-4.25	-0.2127E-02	0.3324E-03
81000.0	-3.08	-4.45	-0.2194E-02	0.4549E-03

Table 3.5 Prism No. 3 - Principal strains.

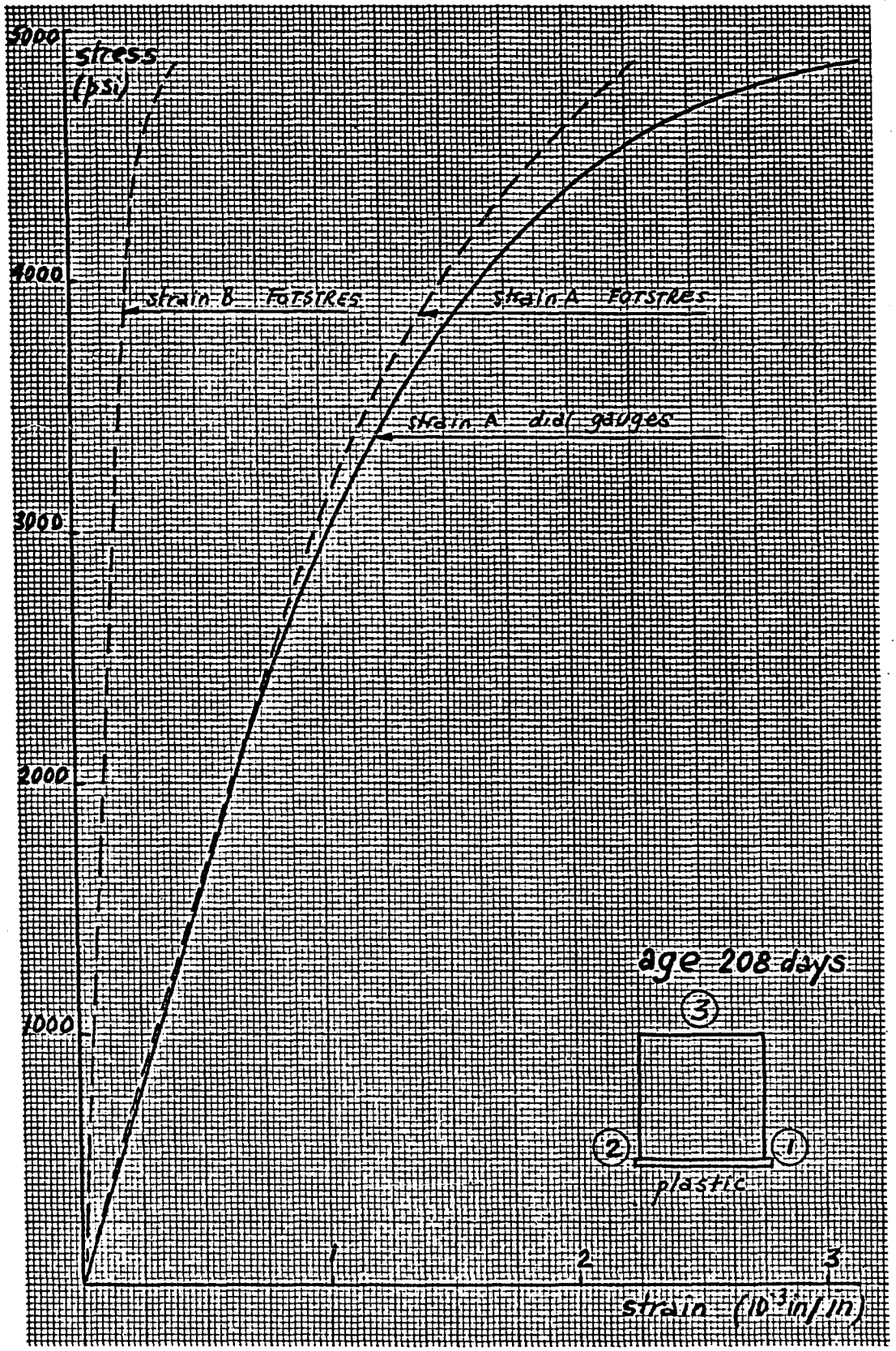

Fig. 3.17 Prism No. 3 . Stress-strain curve.

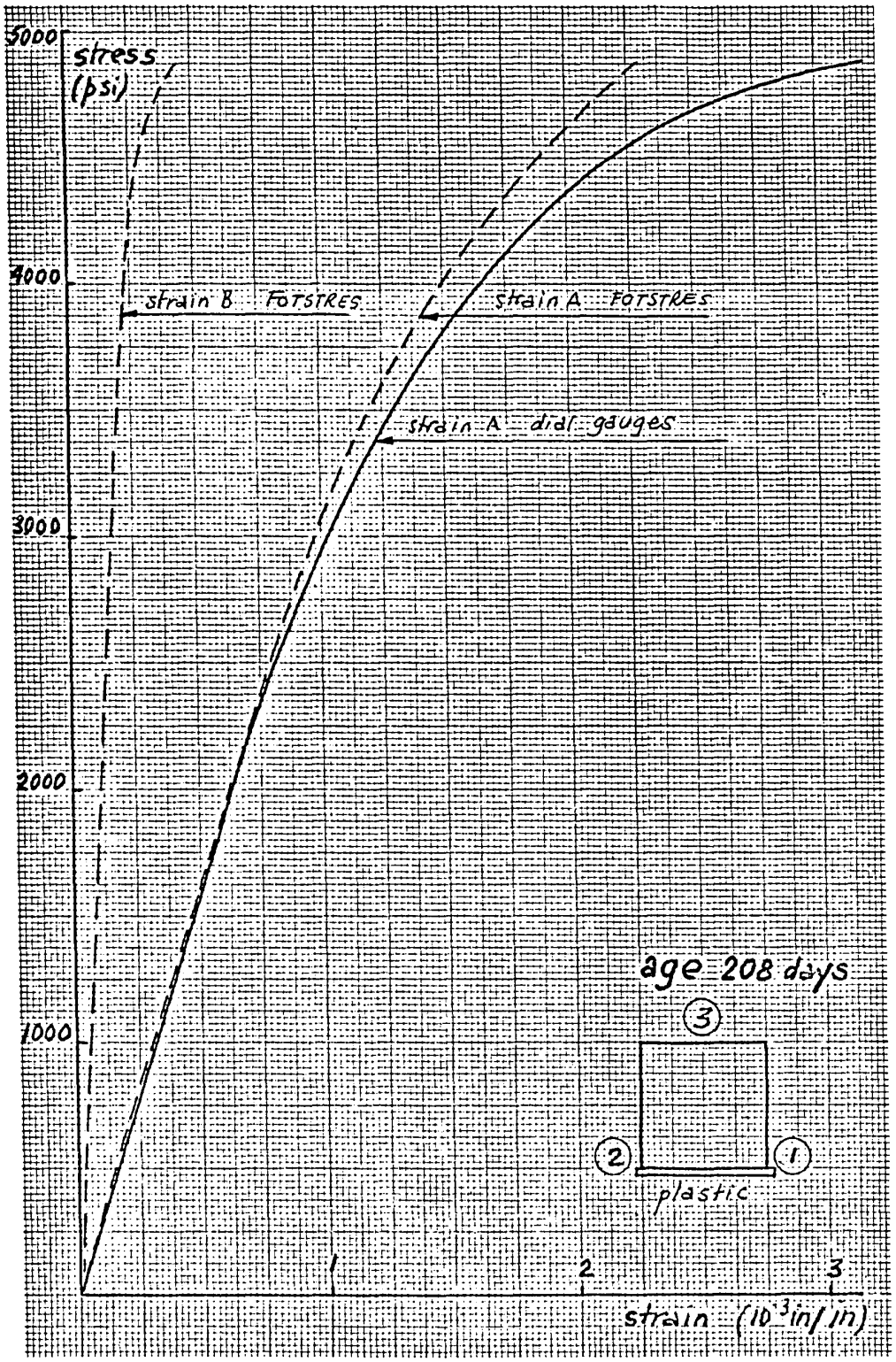

Fig. 3.17 Prism No. 3 . Stress-strain curve.

NO OF POINTS	NO OF LOADS	FRINGEVALUE		
1	19	0.8600E-03		
LOAD	NN	NC	STRENA	STREN
4CCC.0	-0.14	-C.6C	C.C	C.0
6CCC.0	-0.24	-C.86	C.9804E-C5	C.9580E
8CCC.0	-0.32	-C.96	-C.4988E-C4	C.1049E
12CCC.0	-0.44	-1.1C	-C.1264E-03	C.1316E
16CCC.0	-0.52	-1.15	-C.1212E-C3	C.2056E
2CCCC.0	-0.57	-1.3C	-C.2721E-C3	C.9770E
24CCC.0	-0.65	-1.42	-C.3578E-C3	C.8084E
28CCC.0	-0.79	-1.52	-C.3648E-03	C.1942E
32CCC.C	-0.86	-1.66	-C.5112E-03	C.1080E
36CCC.0	-0.92	-1.75	-C.54C7E-03	0.1387E
42CCC.0	-1.C7	-1.94	-C.6646E-C3	C.1352E
48CCC.0	-1.23	-2.14	-C.784CE-C3	C.1534E
54CCC.0	-1.4C	-2.28	-C.8167E-03	C.2669E
6CCCC.0	-1.62	-2.6C	-C.1C39E-02	C.2336E
66CC0.C	-1.8E	-2.8C	-C.1071E-02	0.4255E
72CCC.0	-2.2C	-3.25	-C.1375E-C2	C.3971E
78CCC.0	-2.54	-3.64	-C.1583E-C2	C.4813E
81CCC.0	-2.77	-3.88	-C.1693E-C2	C.5691E
84CCC.C	-3.C5	-4.25	-C.1928E-C2	0.5751E

Table 3.6 Prism No. 4. Principal strains.

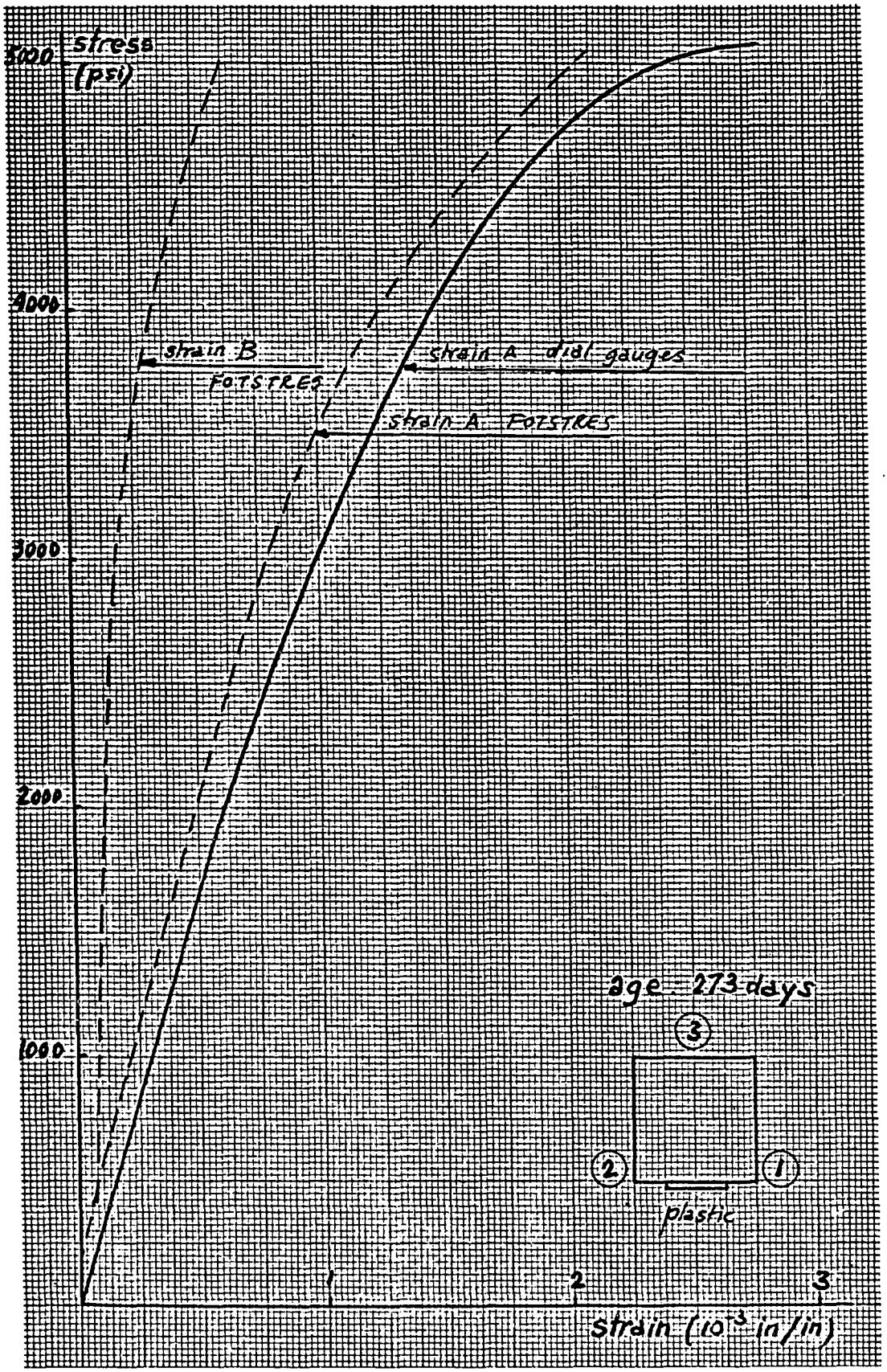

Fig. 3.18 Prism No. 4 . Stress-strain curve.

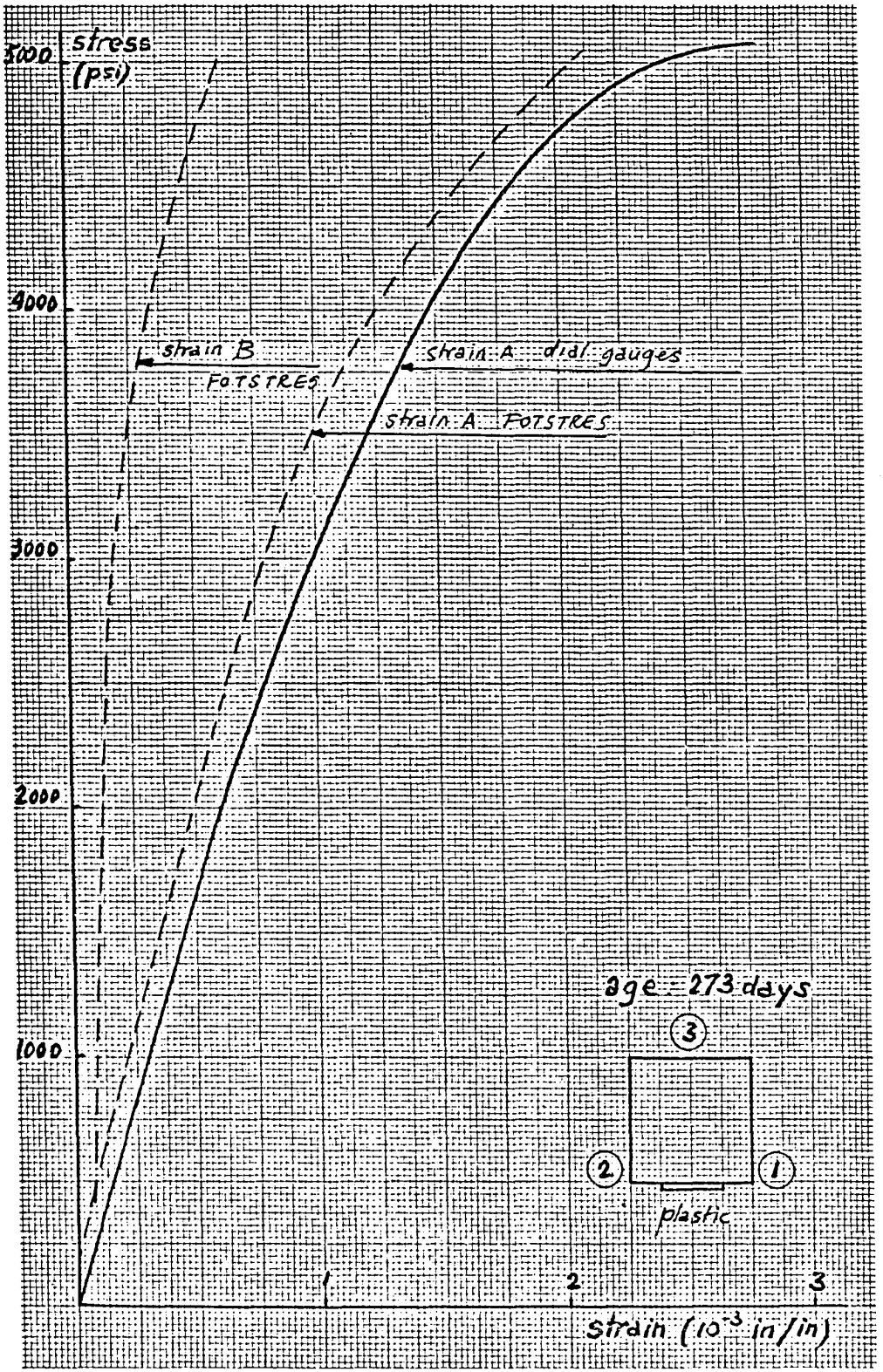

Fig. 3.18 Prism No. 4 . Stress-strain curve.

3.5 Tests on beams in bending.

3.5.1 Aims-Design of the beams.

In section 3.4, stress-strain curves of mortar in axial compression have been obtained with good accuracy.

This encouraging result led the author to proceed to the last part of the experimental program, i.e. the determination of the strains in the hinging region of a reinforced beam in bending, by means of the Photostress technique.

In the experiments on prisms, readings were generally discontinued shortly before failure, when creep was becoming too important.

The same time effect problem occurs for the beams; it is of the greatest importance if inelastic behaviour is being studied.

The aim of this study on beams is to develop a technique that will enable the researcher to record a complete strain distribution in a minimum of time.

Four simply supported beams were built, and tested. They were designed for the following criteria:

1) In order to make the collection of data near or at ultimate as easy as possible, the hinge was to occur at a section of symmetry, so that the directions of the principal strains be the same throughout the test:

2) Parasitic fringes due to a concentrated load were not desirable in the hinging region, as they would superimpose to the fringe pattern in bending.

3) The hinging region had to be located in advance, so as to limit the area covered by the plastic. These conditions led to design the beams for two symmetrical loads and to taper the top face of the beam so that the mid-span section be the section of minimum resistance.

4) The overall dimensions had to be such that the ultimate load of the beams be compatible with the range of available testing machines, and that the area of the hinging region correspond to the field of the polariscope, which was to be located at about two feet from the beam.

This led to design the beam with a length of 48 inches, a width of three inches, and a depth of 5 inches, as shown on fig 3.19; as such these beams could be carried by one man.

Two equal loads were applied at 9 inches from the section of symmetry, and the actual span was 44 inches.

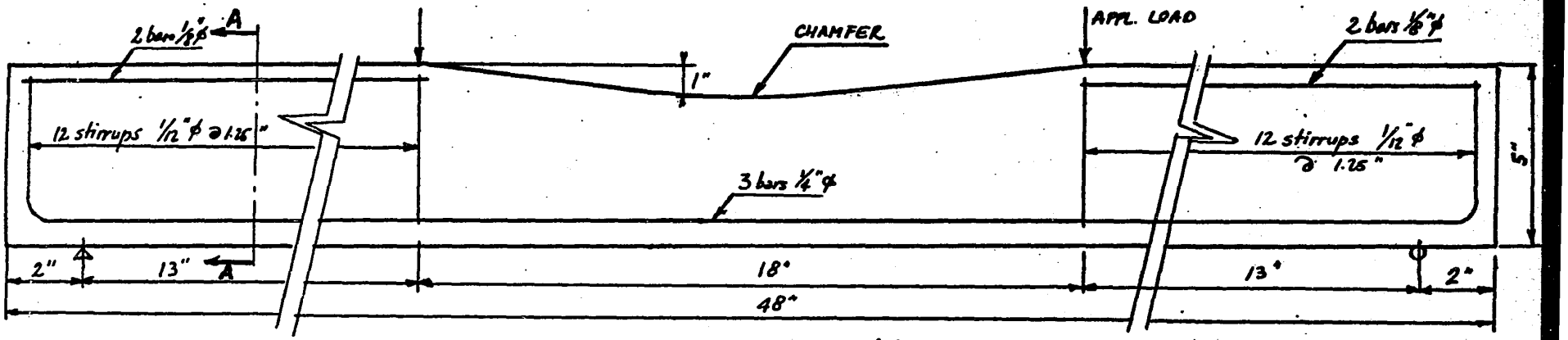

Elevation (scale 1/4)

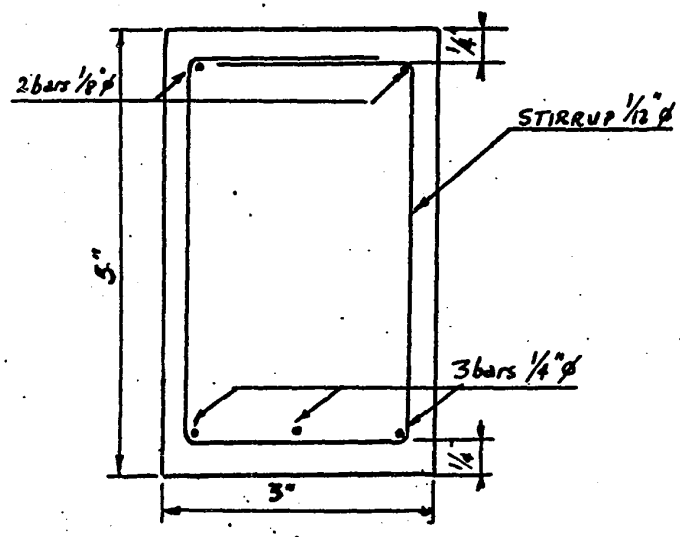

section AA
(scale 1/2)

Bar list (2 beams)

1/4"ϕ : 6 bars — 4 | 47 | 4 — 14½

1/8"ϕ : 8 bars

1/12"ϕ : 48 stirrups :
4 seats
4 spacers

J.C. Mamet	Sketch No 1
Model beam for Photostress analysis	
SCALES	sept 26th 67
1/2 . 1/4	REV.
No Page 98	Fig. 3.19

Compressive reinforcement was not considered for the critical section, in order to avoid parasitic effects on the fringe pattern; the critical section was largely underreinforced in order to obtain a marked range of inelastic behaviour.

The shear spans of the beam were heavily reinforced for shear, in order to allow for a possible overload; compressive reinforcement was used there to hold the stirrups.

Again, mortar was used instead of concrete.

3.5.2 Fabrication of the specimen.

The beams were cast two at a time in the form shown on fig 3.20 .

The mortar mixes were identical to those used for the prisms, and described in section 3.4 .

So were the compacting and curing procedures.

The reinforcing cages were spot-welded, fitted with small wire seats, and then cleaned with acetone, and placed in the forms.

Beams No. 1 and 2 were tested at 248 and 269 days respectively; beams No. 3 and 4 were tested after 14 days only.

For each series of two beams, the following samples were taken :

- tensile steel : 4 coupons
- compression steel : 2 coupons
- stirrups : 2 coupons
- mortar : six 3" x 6" cylinders for compression tests
  two 3" x 6" cylinders for split tension test

The average tensile strength of the mortar was 533 psi for beams 1 and 2,and 383 psi for beams 3 and 4.

The stress-strain curves for the mortar in compression, and for steel are given on figures 3.21 to 3.26 .

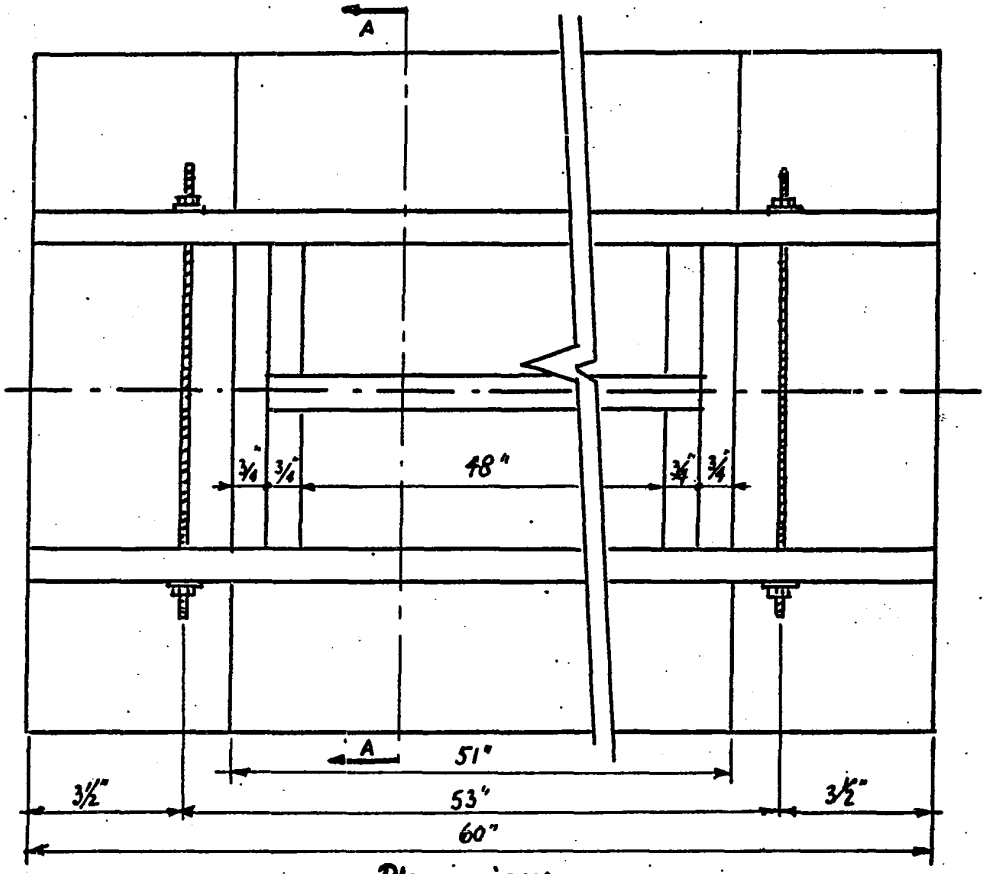

Plan view

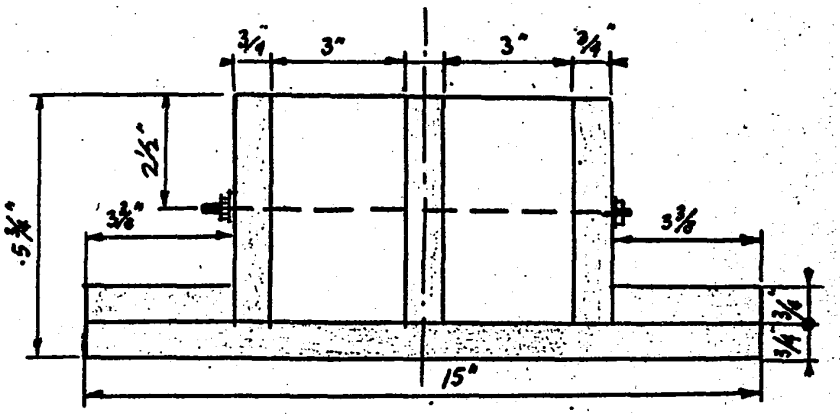

section AA

Bill of materials:

Plywood:
- 1 - 60 x 15 x ¾
- 2 - 60 x 5 x ¾
- 2 - 51 x 3⅜ x ¾
- 2 - 49½ x 5 x ¾
- 2 - 6⅜ x 5 x ¾
- 4 - 3 x 5 x ¾

Miscellaneous:
- 2 Threaded rods, ~ 10" Lg.
- 4 Nuts
- 4 Washers
- Woodscrews + nails

J. C. Mamet	Sketch No 2.
Formwork for beams Nos 1 to 9. 3" x 5" x 48"	
Scale 1/4	oct 3rd, 67
	REV
No. PAGE 101	fig 3.20

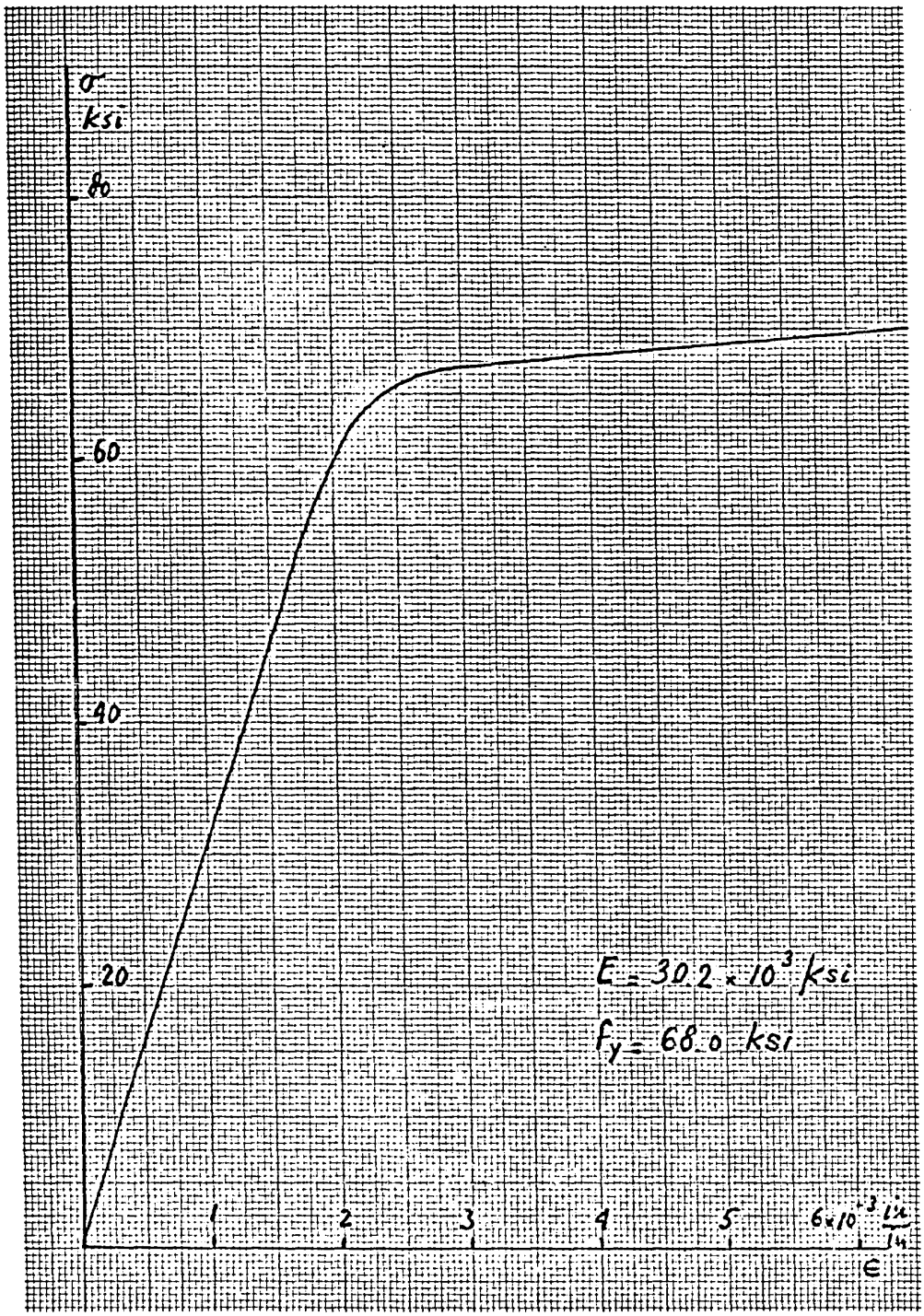

Fig. 3.21 Beams 1 and 2 . Tensile reinforcement.
Stress strain curve.

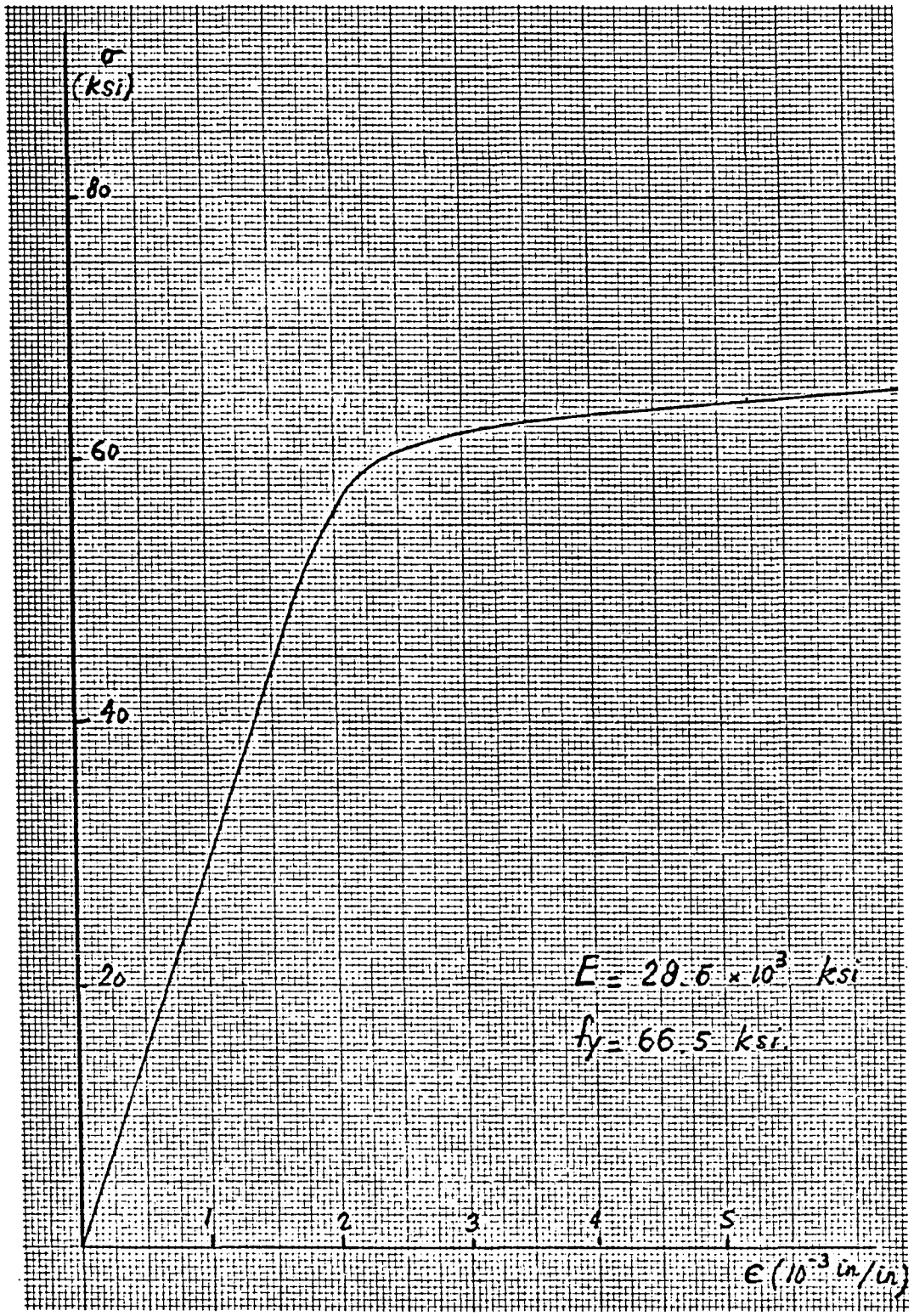

Fig. 3.22 Beams 3 and 4 . Tensile reinforcement. Stress strain curve.

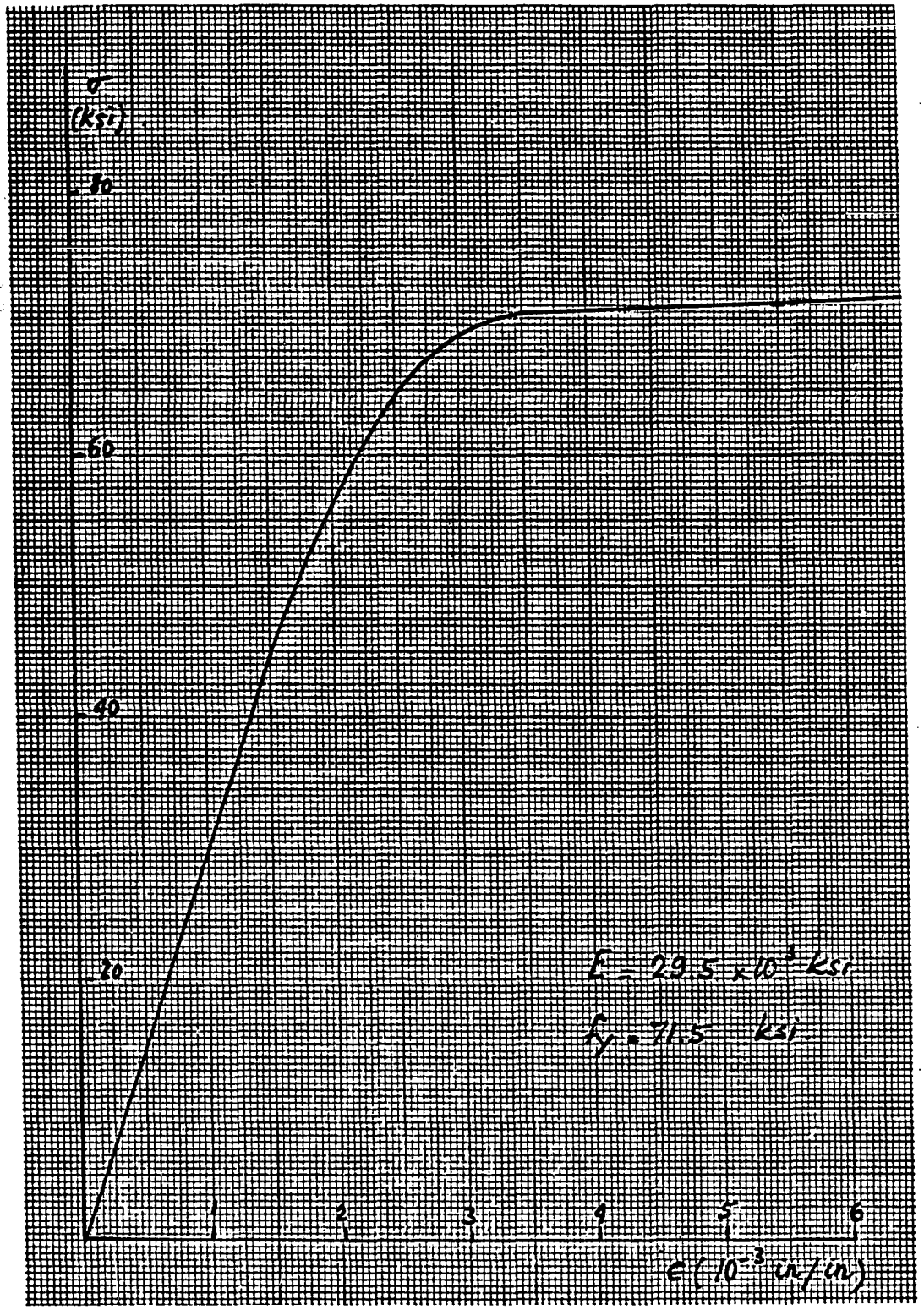

Fig. 3.23 Beams 1 to 4. Stirrups. Stress strain curve.

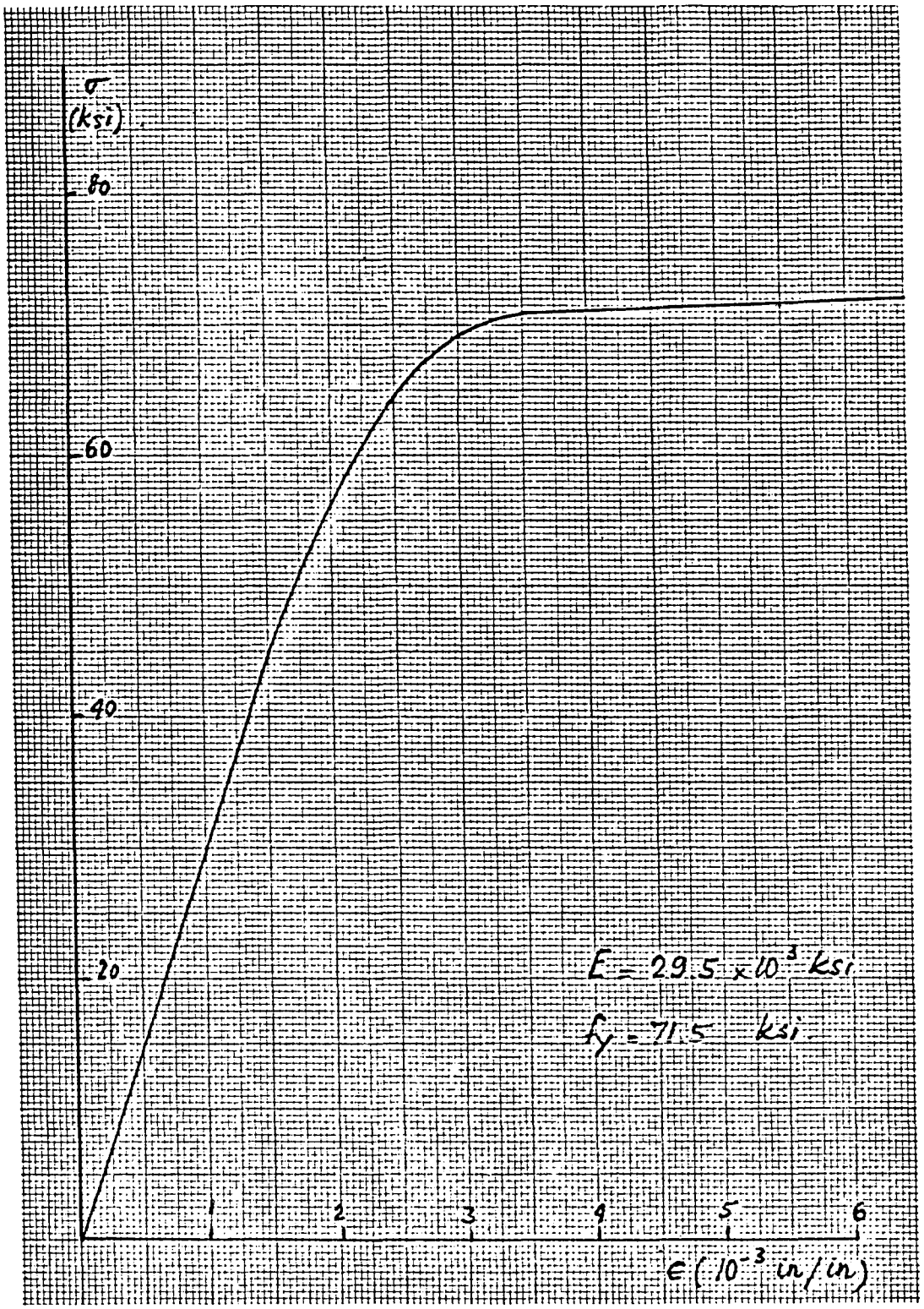

Fig. 3.23 Beams 1 to 4. Stirrups. Stress strain curve.

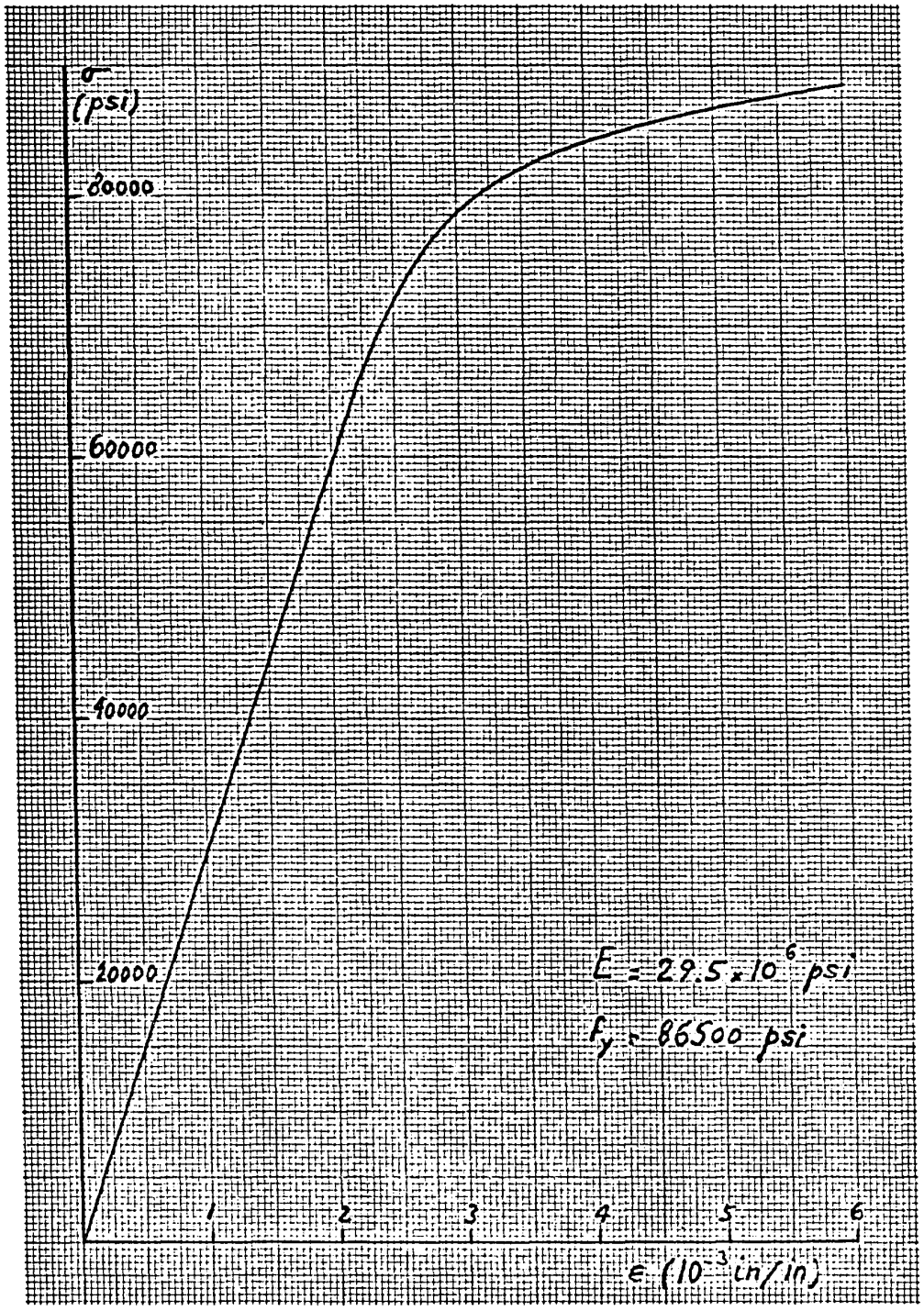

Fig. 3.24 Beams 1 to 4 . Compressive reinforcement.

Stress-strain curve.

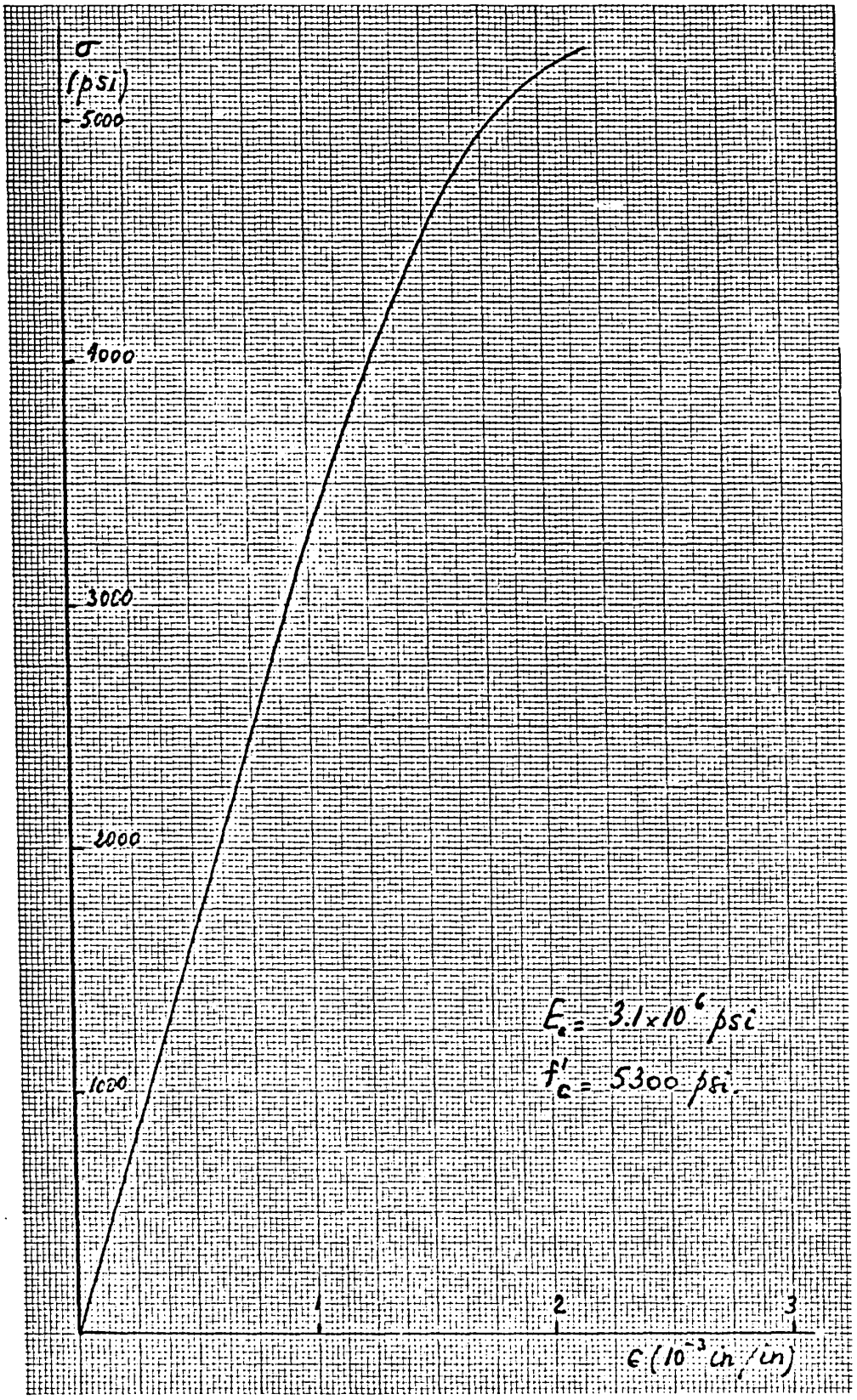

Fig. 3.25 Mortar for beams 1 and 2 . Stress strain curve.

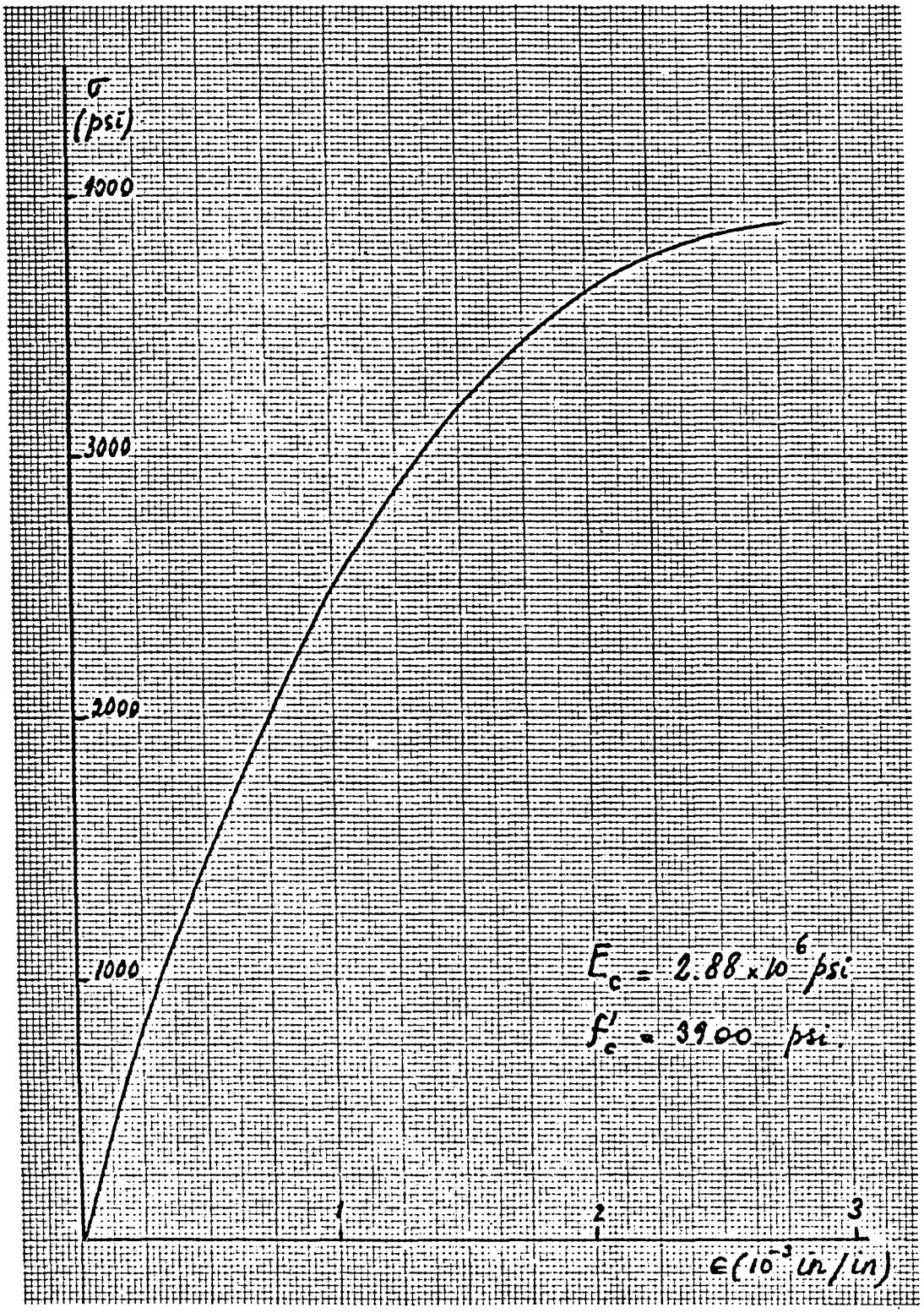

Fig. 3.26 Mortar for beams 3 and 4 . Stress strain curve.

3.5.3 Analysis of the beams.

The analysis of the beams was performed in accordance with sections 2.2.1, 2.2.2, 2.2.3 and 2.3.2 above.

The beams were idealized in a succession of segments 2" and 13" long, and having the geometrical properties shown on fig 3.27 .

Due to the difference in the age of beams 1-2 and 3-4, at testing, and in the resulting difference in the strength of the mortar (see figs. 3.25 and 3.26), separate calculations had to be performed for the two series of beams.

For each segment of the beams, the characteristic values of the moment-curvature diagram, at initiation of cracking, at yield and at ultimate were determined.

The values pertaining to the critical section of beams 1 and 2 have been calculated as examples, in sections 2.2.1.1, 2.2.2.1, and 2.2.3.1 above.

A summary of characteristic data may be found in table 3.7, for all four beams.

The values of the moments of inertia, deduced from the curvatures, may be found in tables 3.8 and 3.9 .

Curves giving the strains at five points of the critical section, in function of the applied load, may be found in figures 3.28 to 3.42 .

In order to obtain the rotations and deflections of the beams, the latter were regarded as continuous structures of which each segment would correspond to a separate span or member.

A computer program, called CONTBEAM was written to solve continuous beams problems.

It is based on the stiffness method of analysis, in which an overall stiffness matrix of the whole structure is generated, as a combination of the stiffness matrices of its members.

The matrix is then rearranged so as to group terms corresponding to degrees of freedom of the joints, and to restraints of the supports separately.

After the inversion of the matrix, a load vector is formed: all loads are considered to be applied at the joints; however, member loads may be considered as well, in terms of equivalent joint loads.

A displacement vector is then formed, and printed as the output; shears and bending moments at the ends of each member may be printed if desired.

The main limitations of the programme are as follows:

- the number of segments is limited to 24;
- each one must be of constant section;
- twisting or axial load are not considered;
- ultimate behaviour is not considered.

A listing of CONTBEAM may be found in Annexe No.1, as well as a typical print out, (beams No. 1.2, at 5100 lbs.).

Again, beams 1-2 and 3-4 were treated separately.

Load-deflection curves, at mid span and at points situated under the applied loads may be found in figs 3.43 and 3.44 .

The distribution of the rotations along the beams was also plotted on figs 3.45 - 3.46 for several loads.

Finally the spacing of the cracks was calculated with the following formula [Ref 2.22] :

$$e = \frac{0.4\ D \times 2b(h-d)}{A_s} = \frac{0.8\ D\ b\ (h-d)}{A_s}$$

where D is the diameter of the tensile reinforcement bars. For beams 1 to 4, e was found to be 1 inch .

The depth of the cracks has also been calculated, for beams 1-2 and 3-4, by assuming that the strains remained linear, and that the crack was limited to the part of the beam where $\epsilon_c > f_c/E_c$.

Figures 3.47 and and 3.48 give the 'load-depth of cracks' curves.

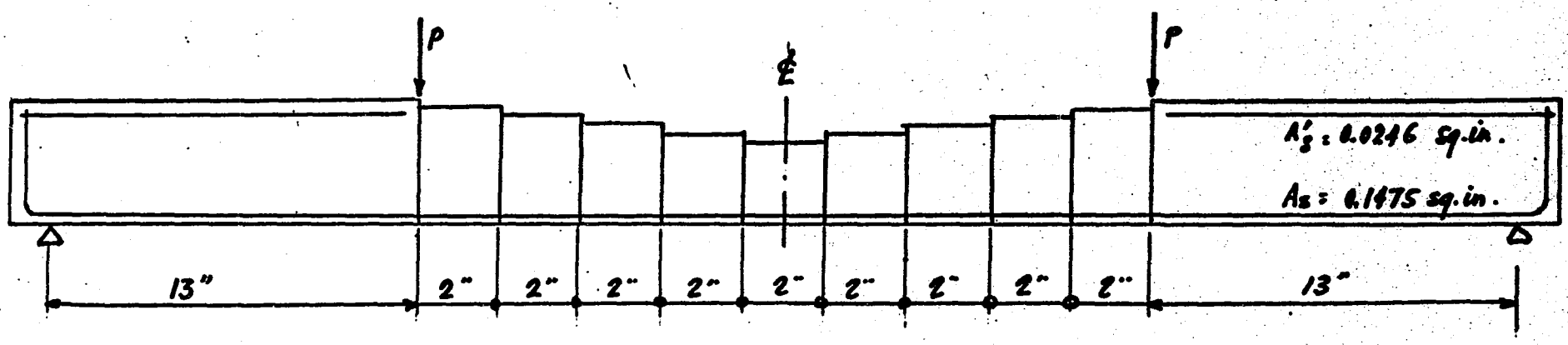

SEGMENT No	1	2	3	4	5	6	7	8	9	10	11
TYPE	6	5	4	3	2	1	2	3	4	5	6
h (in)	5.0	4.875	4.687	4.375	4.187	4.0	4.187	4.375	4.687	4.875	5.0
d (in)	4.75	4.625	4.437	4.125	3.937	3.75	3.937	4.125	4.437	4.625	4.75
b (in)	3.0	3.0	3.0	3.0	3.0	3.0	3.0	3.0	3.0	3.0	3.0
I (in^4)	31.3	28.7	25.5	20.7	18.2	16.0	18.2	20.7	25.5	28.7	31.3
p	0.0103	0.0106	0.0110	0.0119	0.0125	0.0131	0.0125	0.0119	0.0110	0.0106	0.0103
p'	0.0017	0	0	0	0	0	0	0	0	0	0.0017

Fig. 3.27 Beams 1 to 4 - Geometrical Properties.

Table 3.7

Beams B1 - B2

segment no.	Ref. formula	1	2	3	4	5	6
initiation of cracking.							
moment (lbs. in.)	2.7	5670	6180	6700	7560	8100	8870
curvature $\psi \times 10^6$ (in^{-1})	2.9	95	91	87	81	79	75
k	2.4	0.58	0.575	0.574	0.567	0.561	0.56
applied load 2P(lbs.)		872	950	1030	1162	1246	1364
yield of steel							
moment	2.20	32400	34200	36000	38600	40500	48550
curvature $\psi \times 10^6$	2.26	1003	934	878	815	777	955
k	2.18	0.399	0.392	0.384	0.372	0.368	0.354
applied load 2P		4960	5260	5540	5940	6240	7480
ultimate							
moment	2.30	33650	35900	38500			
curvature $\psi \times 10^6$		3050	3100	3410			
k		0.262	0.252	0.240			
applied load		5170	5580	5900			

f'_c = 5300 psi, f_c = 533 psi, f_y = 68 ksi,

$E_c = 3.1 \times 10^6$ psi, $E_s = 30.0 \times 10^6$ psi n = 10

Tables 3.7 (cont'd.)

Beams 3 and 4

segment no.	Ref. formula	1	2	3	4	5	6
initiation of cracking.							
M	2.7	4070	4440	4810	5430	5860	6370
$\Psi \times 10^6$	2.9	73.5	70.4	67.3	62.6	61.1	58.0
k (same as B1-B2)							
2P		626	682	740	836	896	980
yield							
M	2.20	31700	33500	35200	37750	39600	47500
$\Psi \times 10^6$	2.26	1001	934	878	815	777	955
k (same as B1-B2)							
2P		4870	5140	5420	5800	6100	7320
ultimate							
M	2.30	31900	33900	35850			
Ψ		2100	2100	2070			
K (same as B1-B2)							
2P		4900	5220	5520			

$f'_c = 4000$ psi, $f_c = 383$ psi, $f_y = 66.5$ ksi, $E_c = 2.88 \times 10^6$ psi,

$E_s = 28.8 \times 10^6$ psi, $n = 10$

MOMENTS OF INERTIA

$E = 3.1 \times 10^6$ psi

2P Load (lbs.)	P (kips)	I6 ($inches^4$)	I5	I4	I3	I2	I1
400	.200	38.77	34.416	30.822	25.231	22.286	19.488
800	.400	38.77	34.416	30,822	25.231	22.286	19.488
1200	.600	38.77	34.416	28.55	21.50	18.15	14.95
1800	.900	27.3	24.2	21.10	17.0	14.85	12.50
2400	1.200	22.5	20.95	18.6	15.4	13.45	11.55
3000	1.500	20.3	19.40	17.3	14.55	12.80	11.1
3600	1.800	19.0	18.45	16.4	14.02	12.40	10.8
4200	2.100	18.2	17.90	16.1	13.6	12.15	10.6
4500	2.250	17.9	17.67	15.92	13.5	12.05	10.5
4800	2.400	17.6	17.45	15.75	13.4	11.90	10.4
5100	2.550	17.45	17.30	15.55	13.35	11.85	4.28
5400	2.700	17.25	17.15	15.45	13.30	5.38	3.35
5700	2.850	17.05	16.95	15.30	6.20	3.64	3.35

Beams 1 and 2

Table 3-8

MOMENTS OF INERTIA (E = 2.88 x 10^6 psi)

Load 2P	P	I6	I5	I4	I3	I2	I1
400	200	38.77	34.416	30.822	25.231	22.286	19.48
800	400	38.77	34.416	30.822	23.45	19.40	16.35
1200	600	30.40	26.30	23.00	18.60	15.85	13.70
1800	900	23.40	21.90	19.50	16.20	14.15	12.35
2400	1200	20.90	20.20	18.10	15.35	13.40	11.80
3000	1500	19.70	19.10	17.30	14.85	13.10	11.45
3600	1800	18.90	18.70	16.85	14.45	12.80	11.25
4200	2100	18.45	18.40	16.60	14.30	12.65	11.10
4500	2250	18.30	18.20	16.40	14.20	12.60	11.10
4800	2400	18.15	18.10	16.30	14.05	12.50	11.00
5100	2550	18.05	18.00	16.25	14.00	12.50	5.42
5400	2700	17.95	17.90	16.25	13.95	5.61	5.42

Beams 3 and 4

Table 3-9

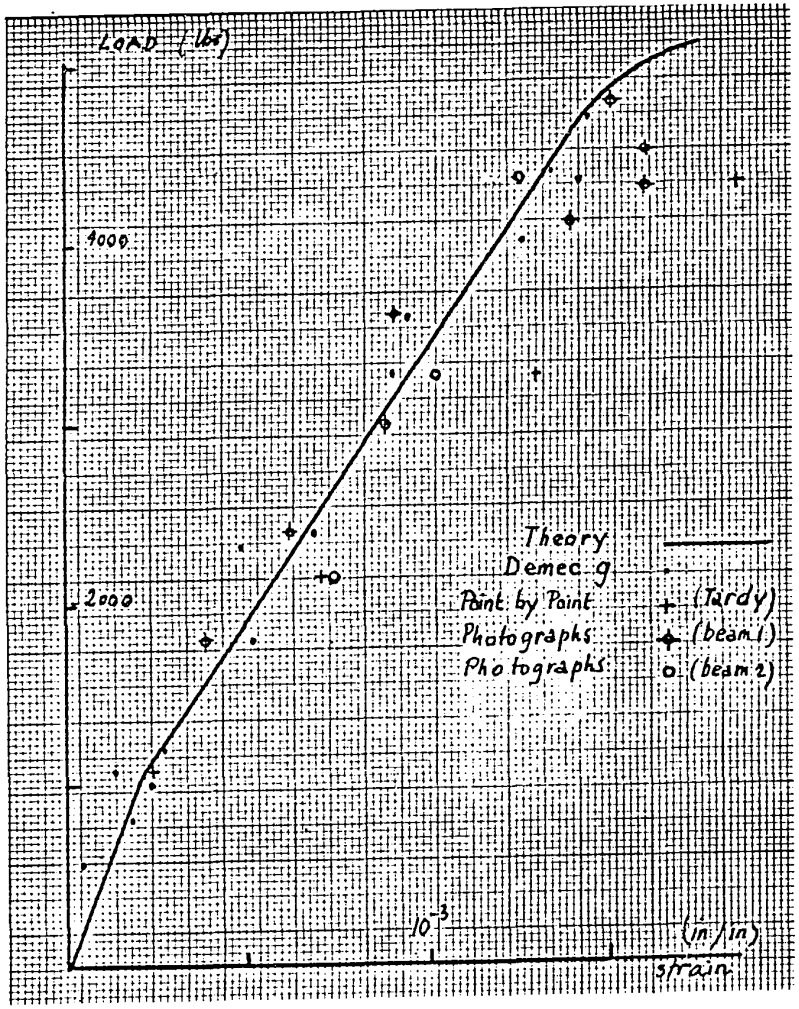

Fig. 3.28 Point 1 .

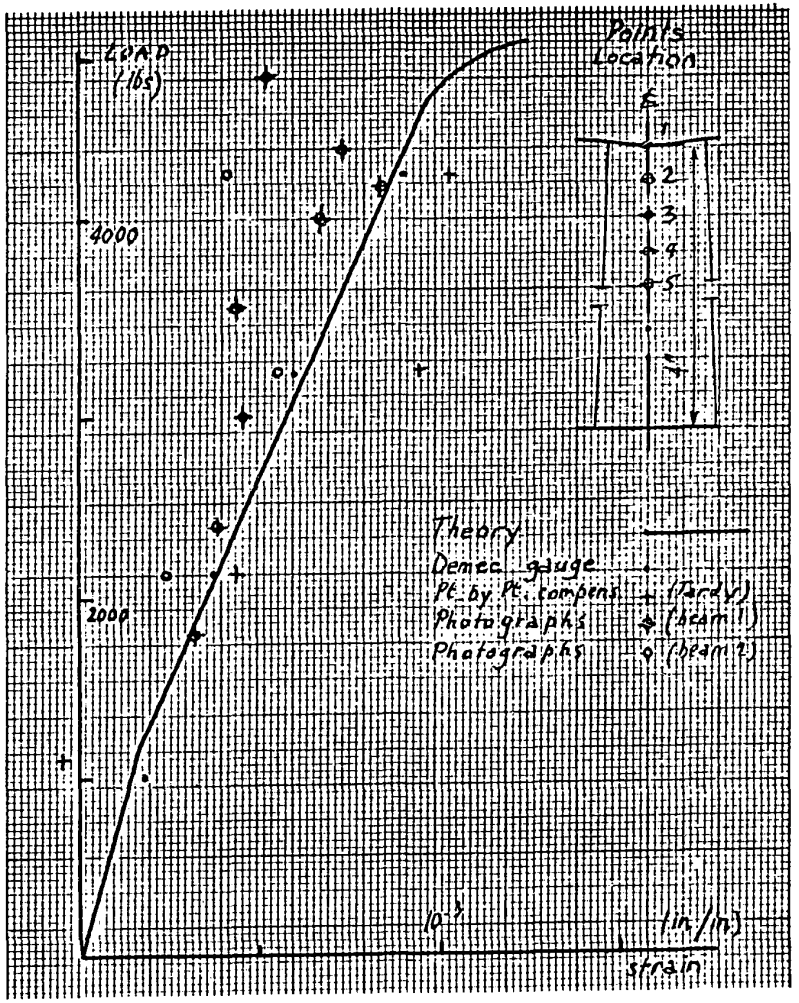

Fig. 3.29 Point 2 .

Beams 1 - 2 . Load-strain curves.

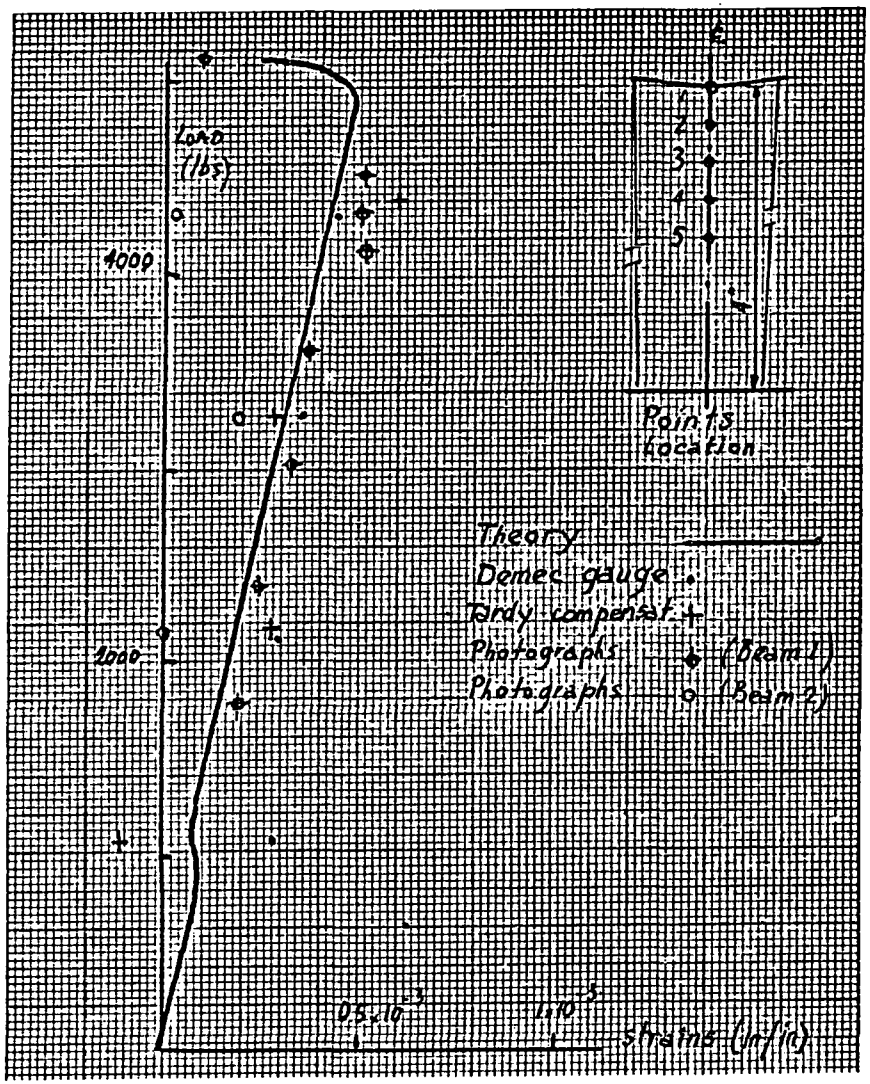

Fig. 3.30 Point 3 .

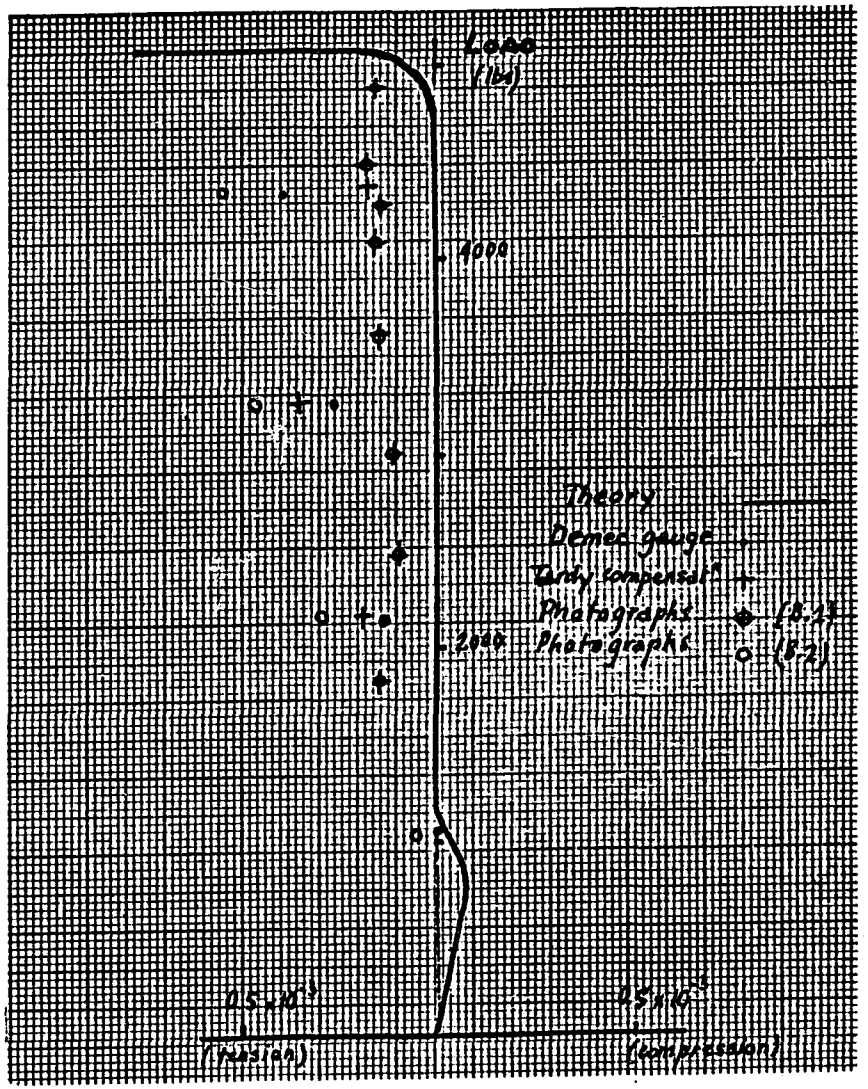

Fig. 3.31 Point 4 .

Beams 1 - 2 . Load-strain curves.

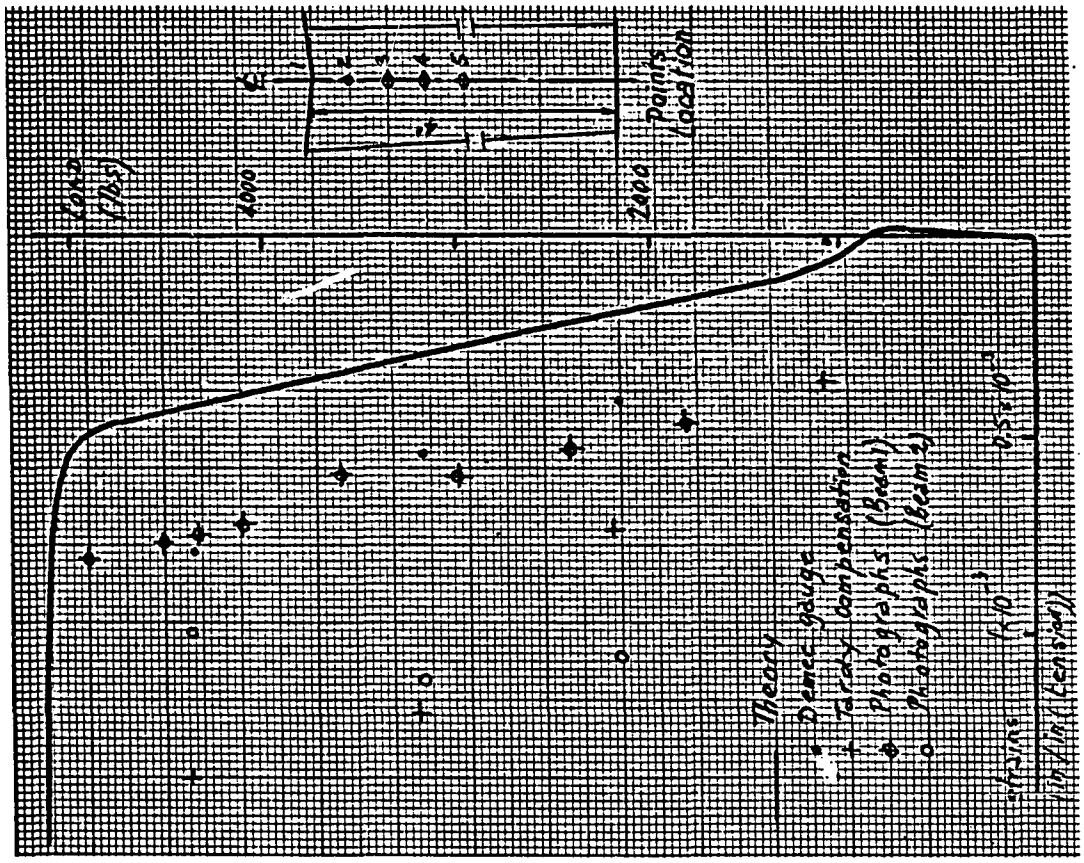

Fig. 3.32 Beams 1 + 2 . Point 5 . Load-strain curve.

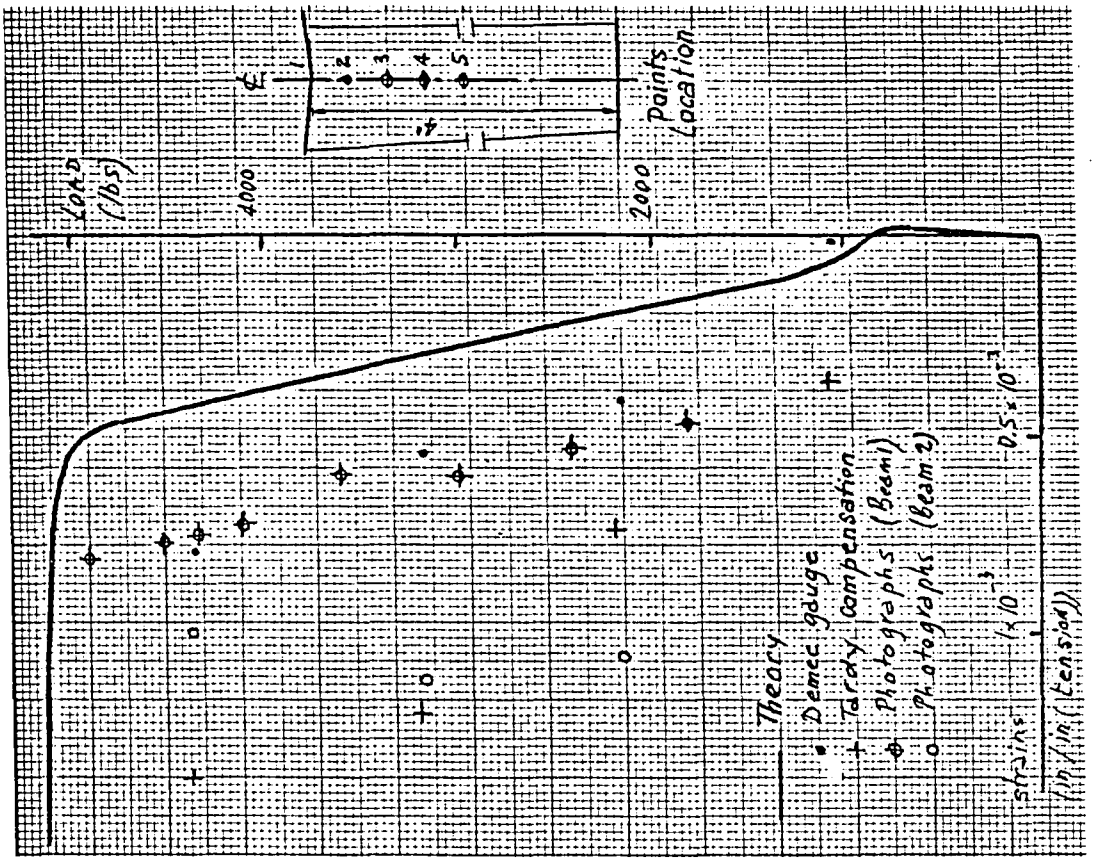

Fig. 3.32 Beams 1 → 2 . Point 5 . Load-strain curve.

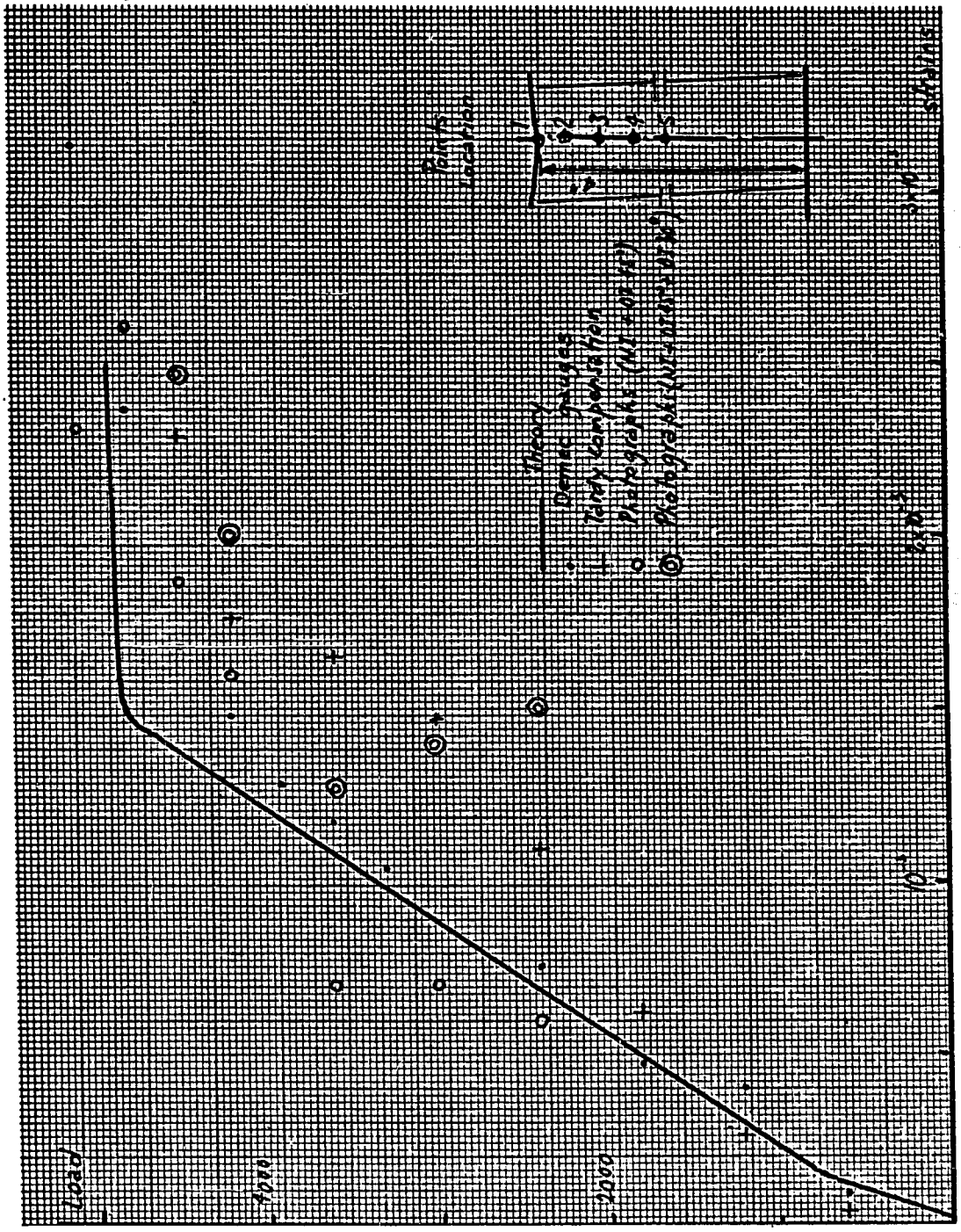

Fig. 3.33 Beam 3 - Point 1 - Load-strain curve.

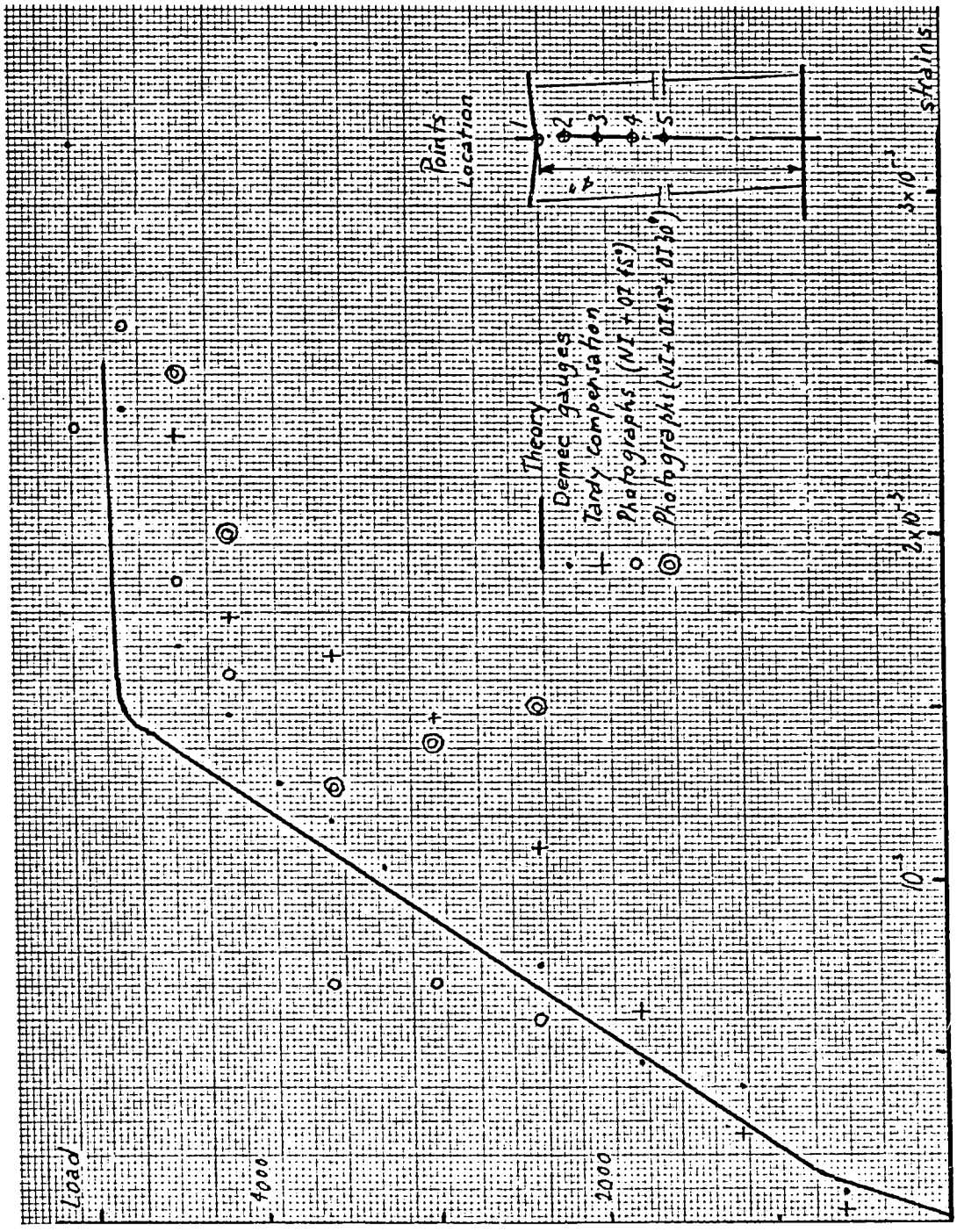

Fig. 3.33 Beam 3 - Point 1 - Load-strain curve.

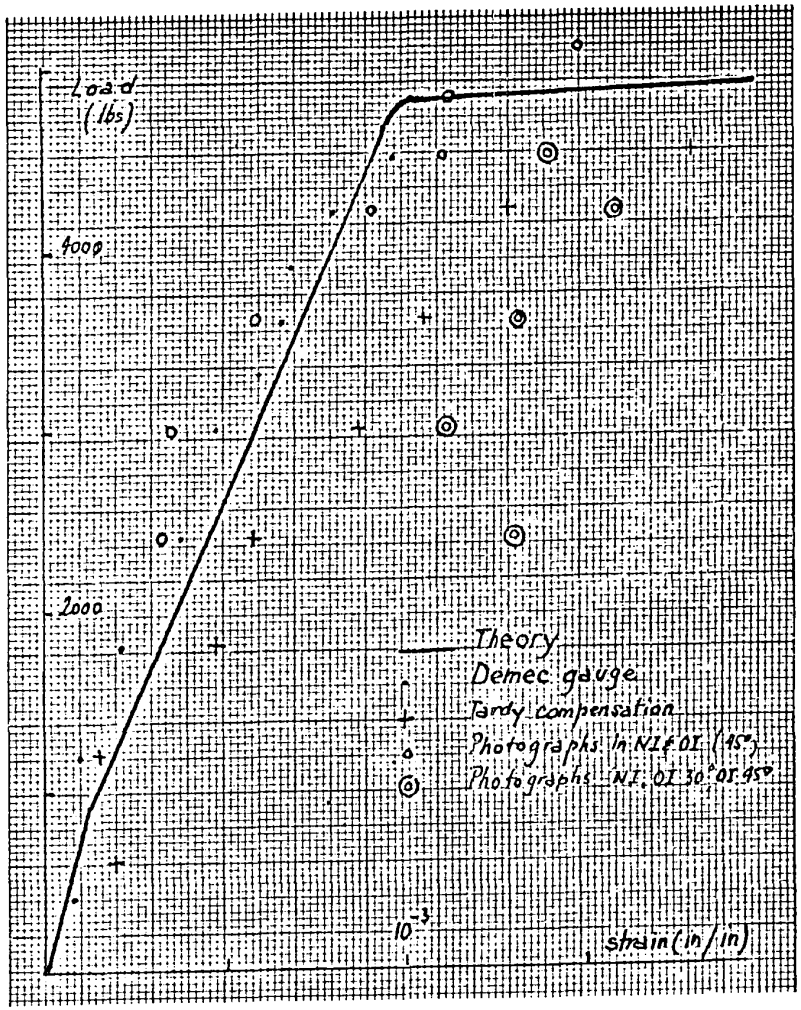

Fig. 3.34 Point 2 .

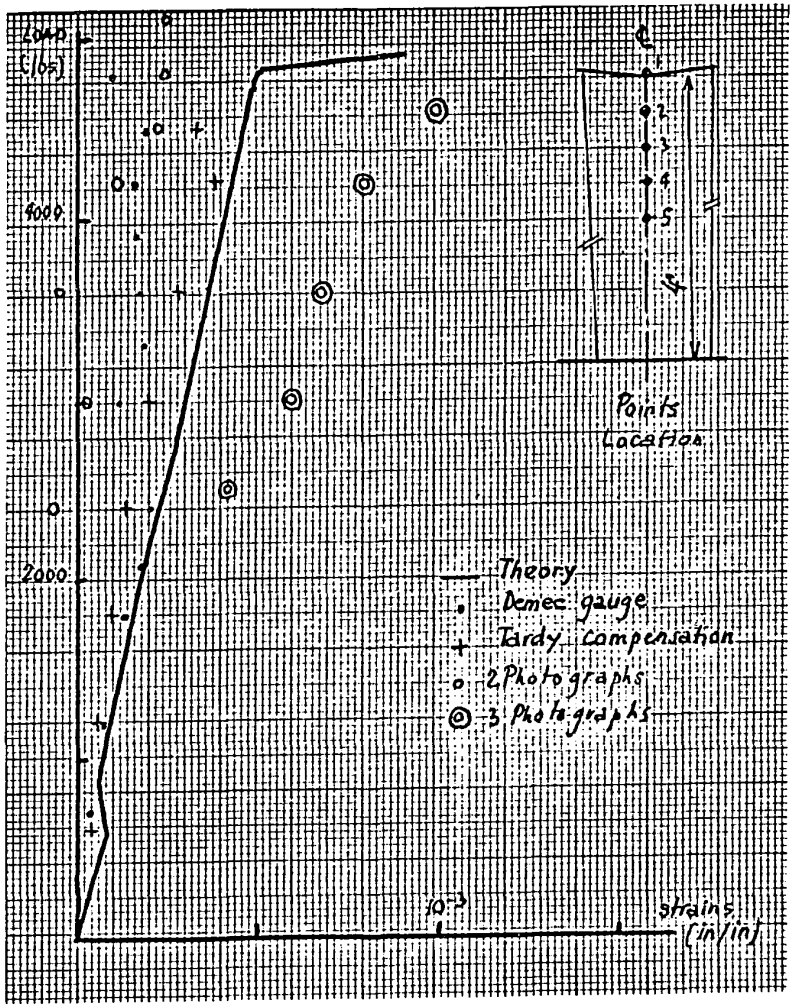

Fig. 3.35 Point 3 .

Beam 3 . Load - strain curves.

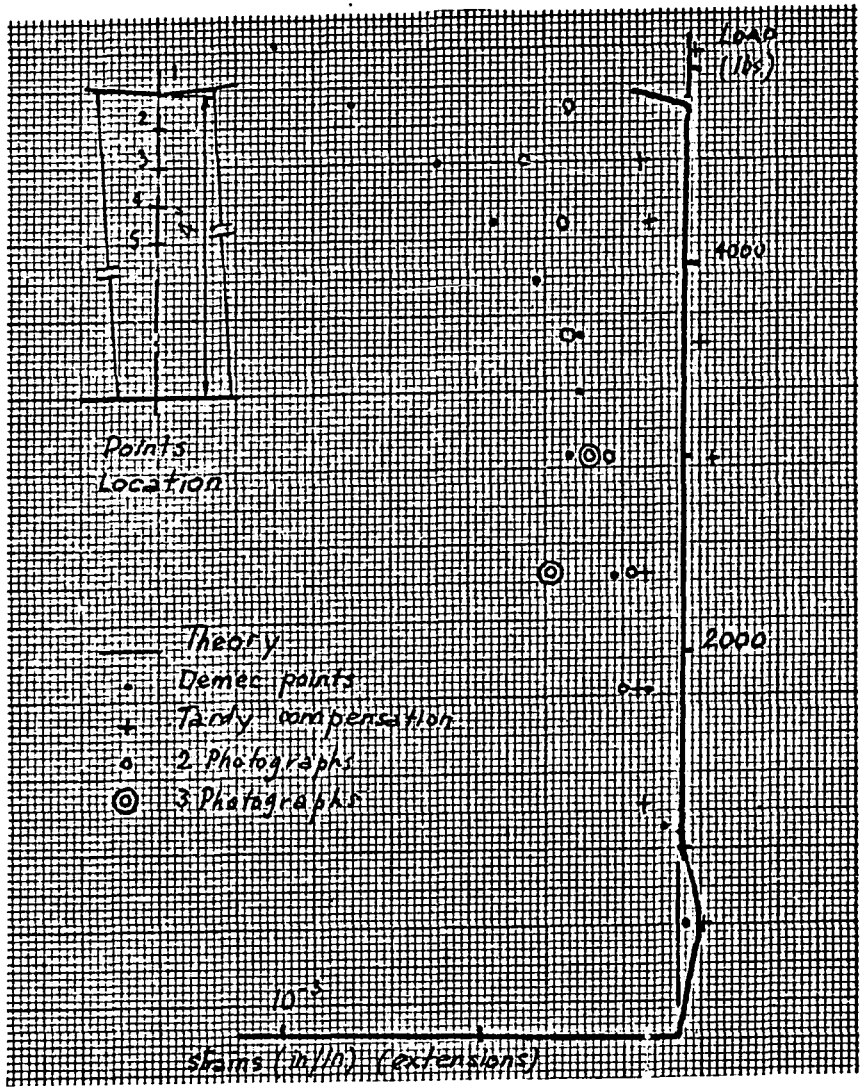

Fig. 3.36 Point 4.

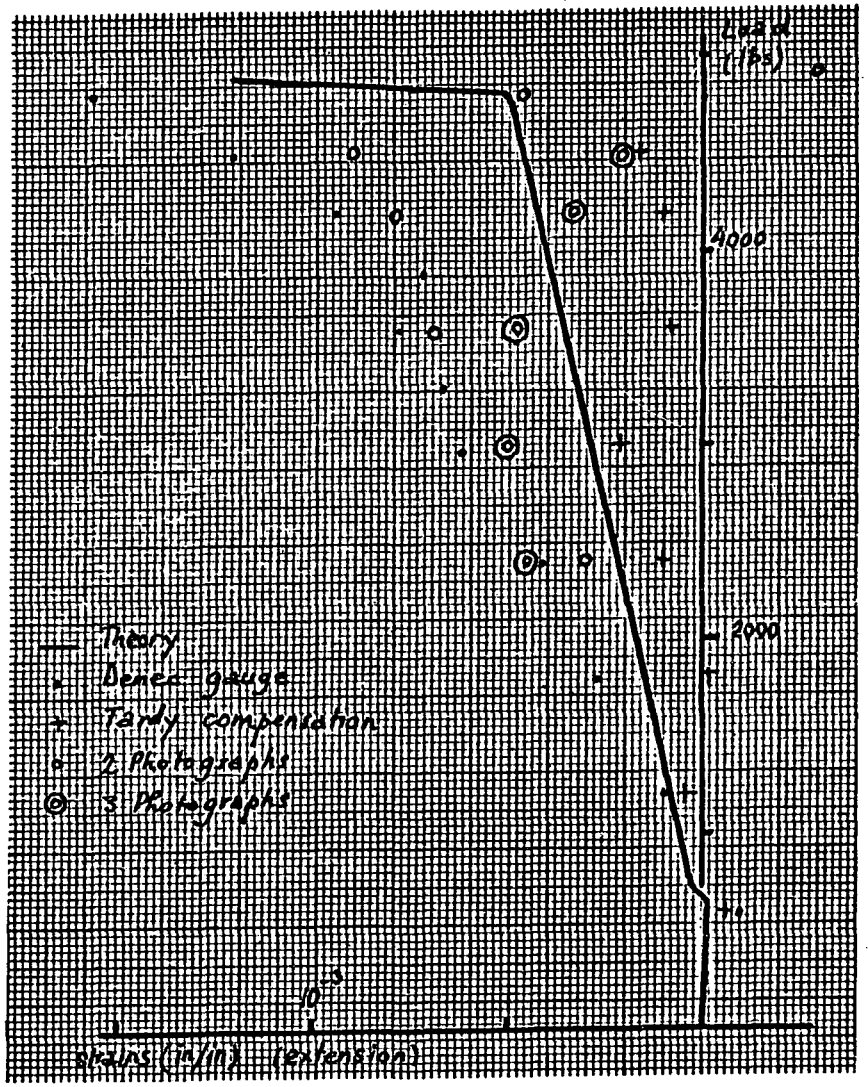

Fig. 3.37 Point 5.

Beam 3 - Load-strain curves.

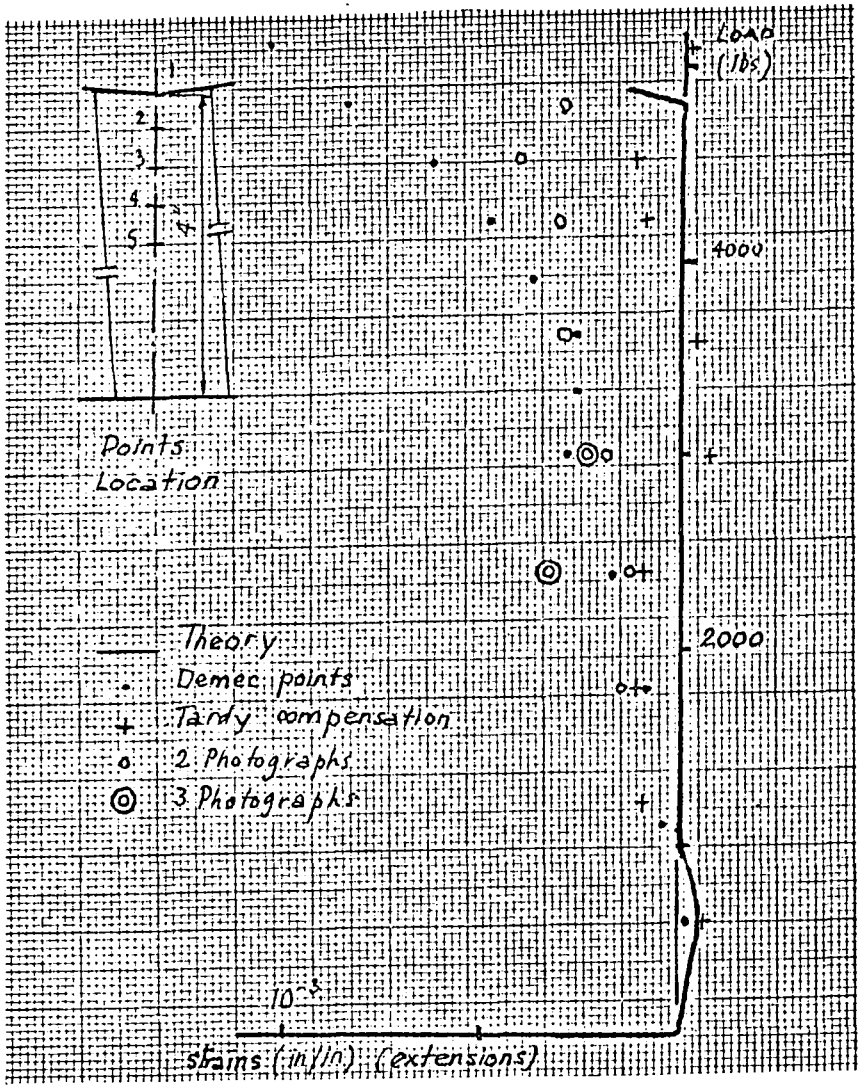

Fig. 3.36 Point 4.

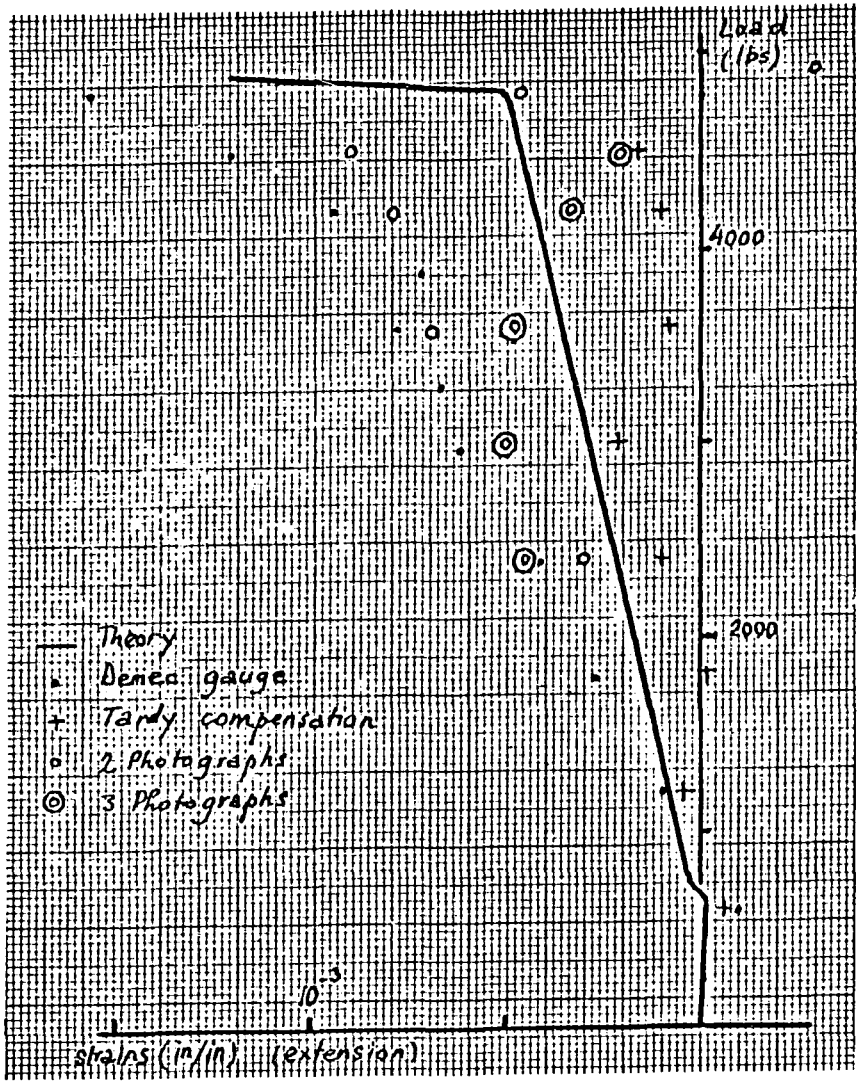

Fig. 3.37 Point 5.

Beam 3 - Load-strain curves.

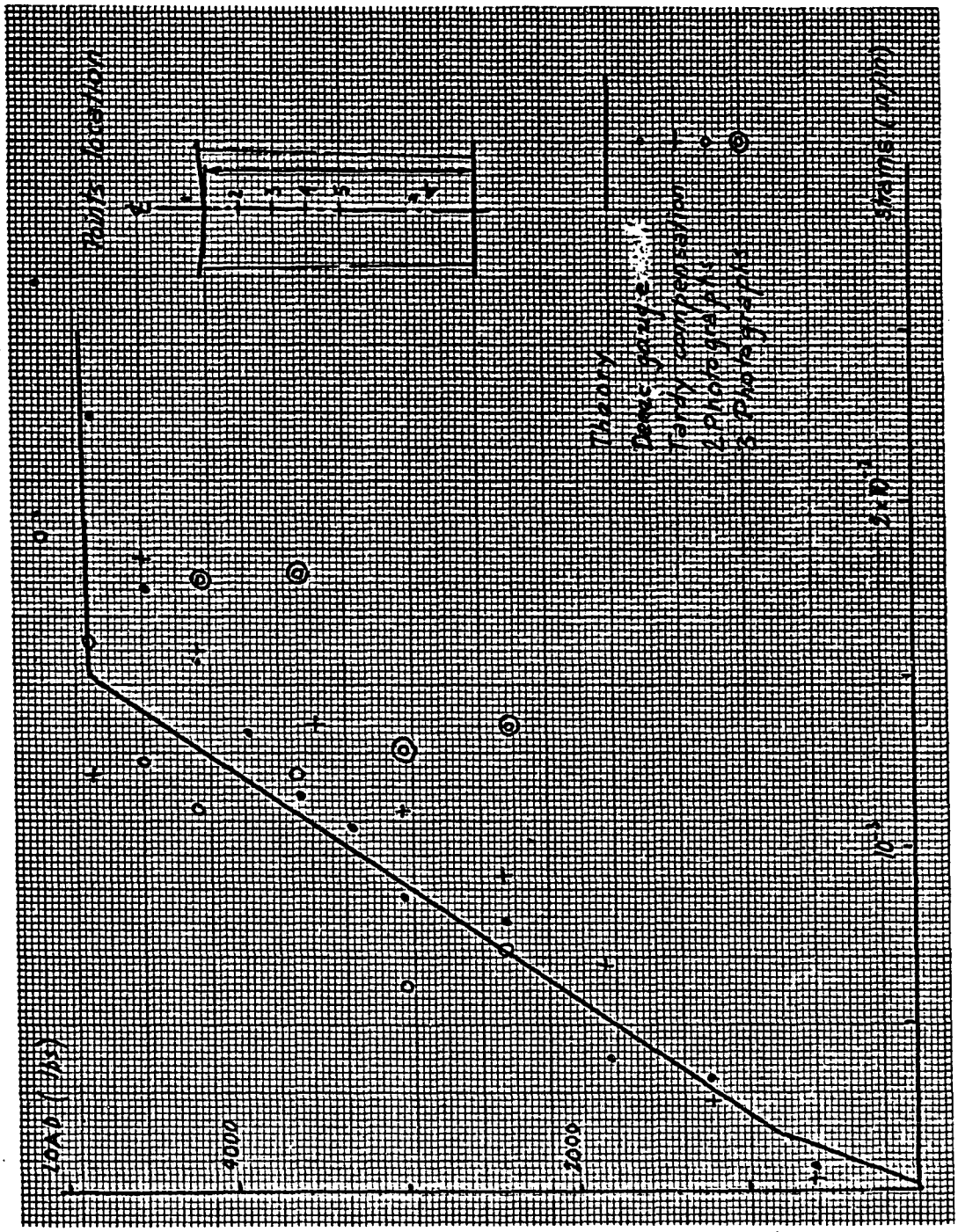

Fig. 3.36 Beam 4 - Point 1 . Load-strain curve.

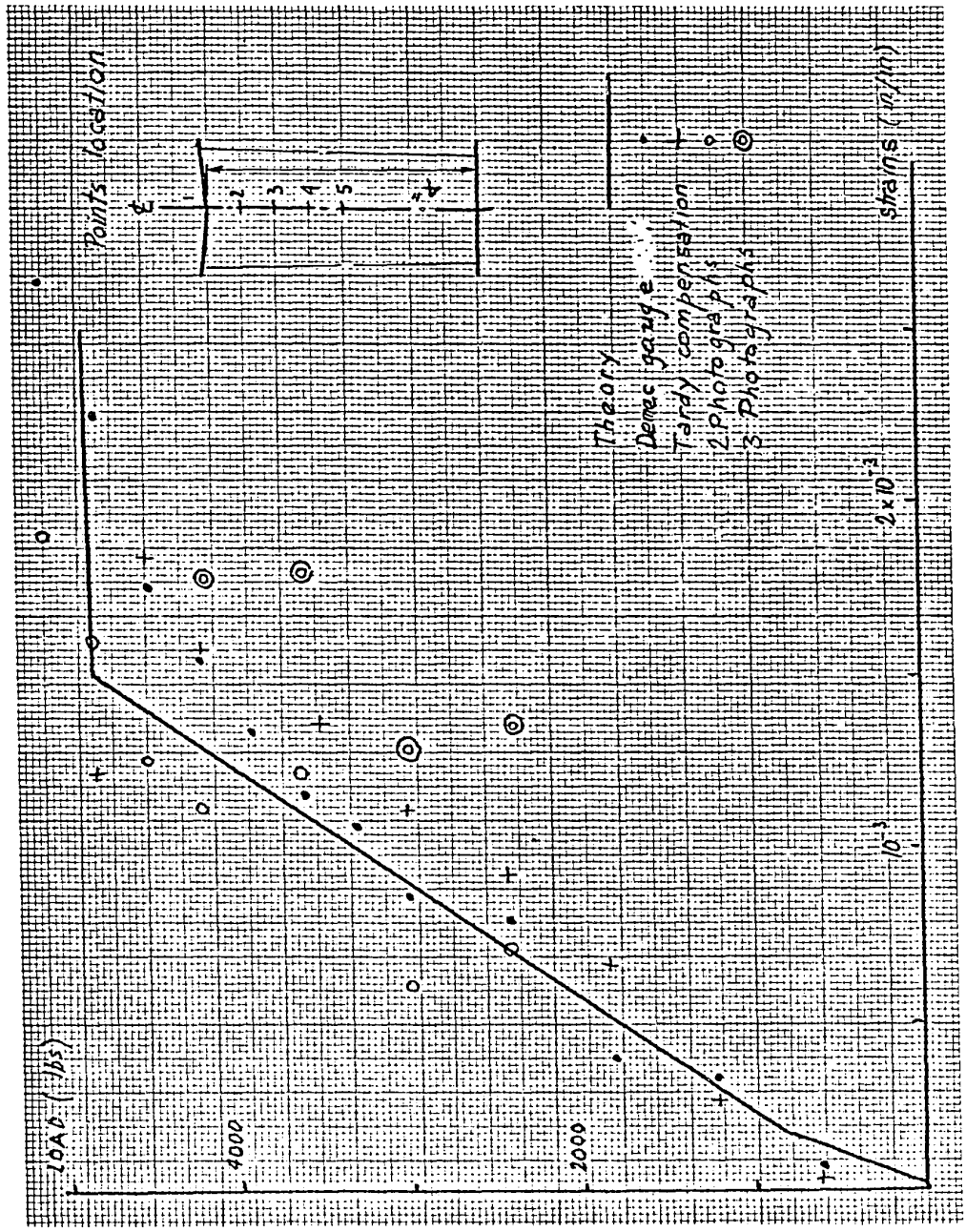

Fig. 3.38 Beam 4 - Point 1 . Load-strain curve.

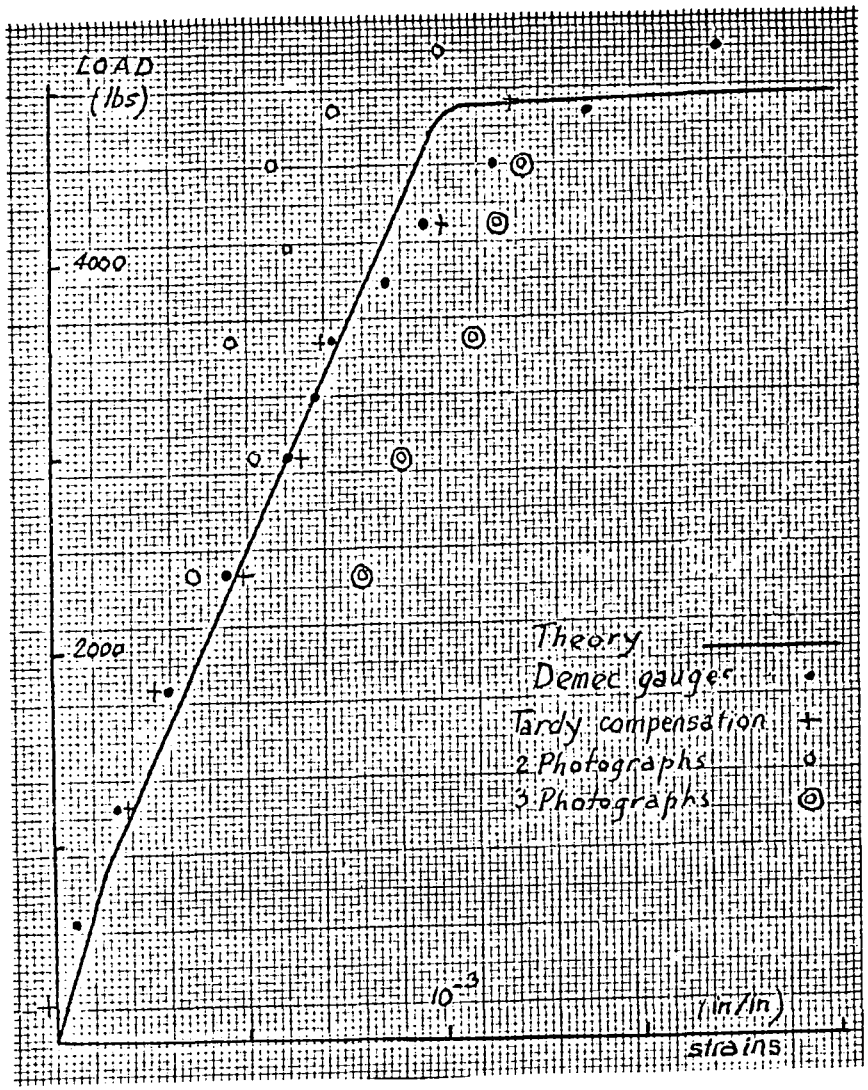

Fig. 3.39 Point 2.

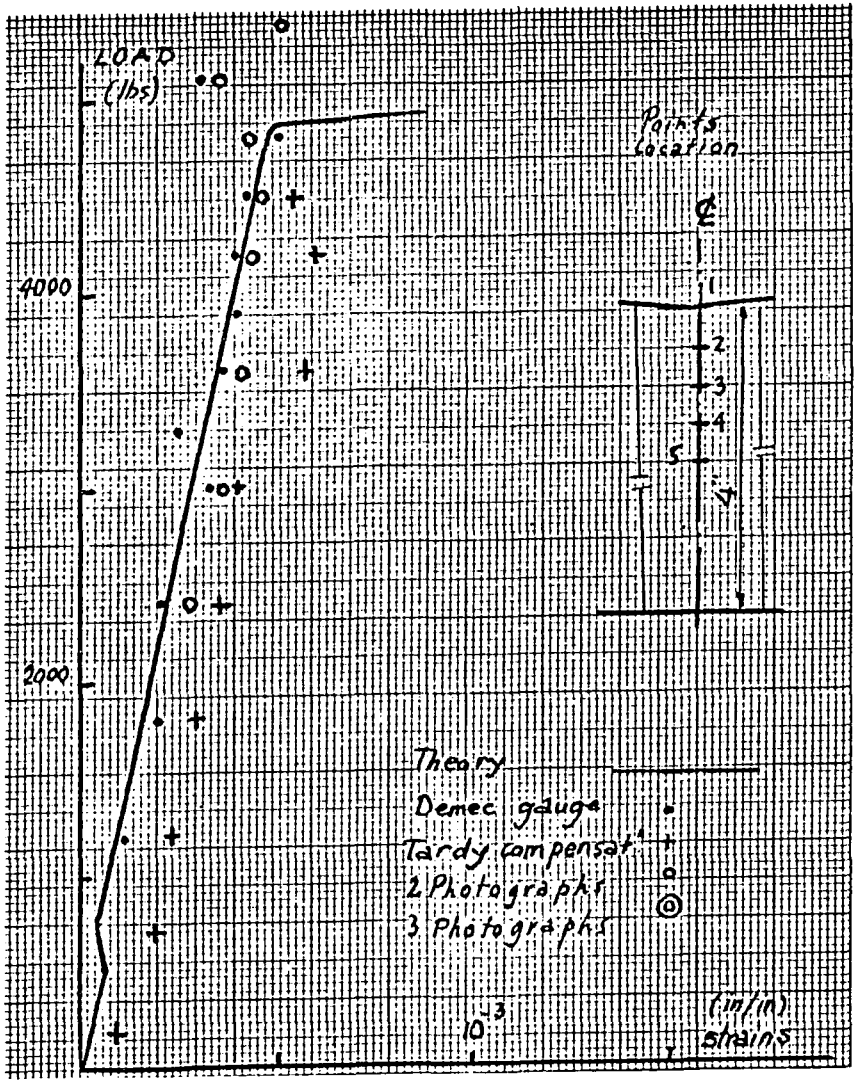

Fig. 3.40 Point 3 .

Beam 4 - Load-strain curves.

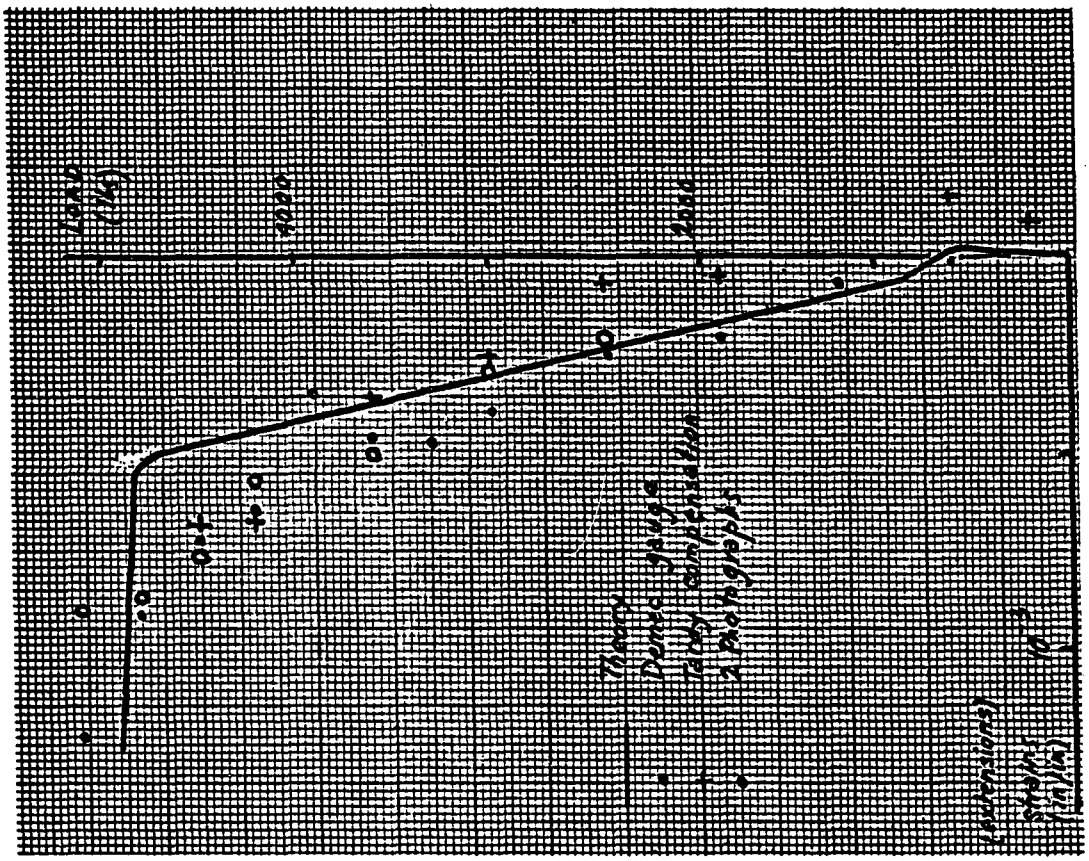

Fig. 3.41 Point 4.

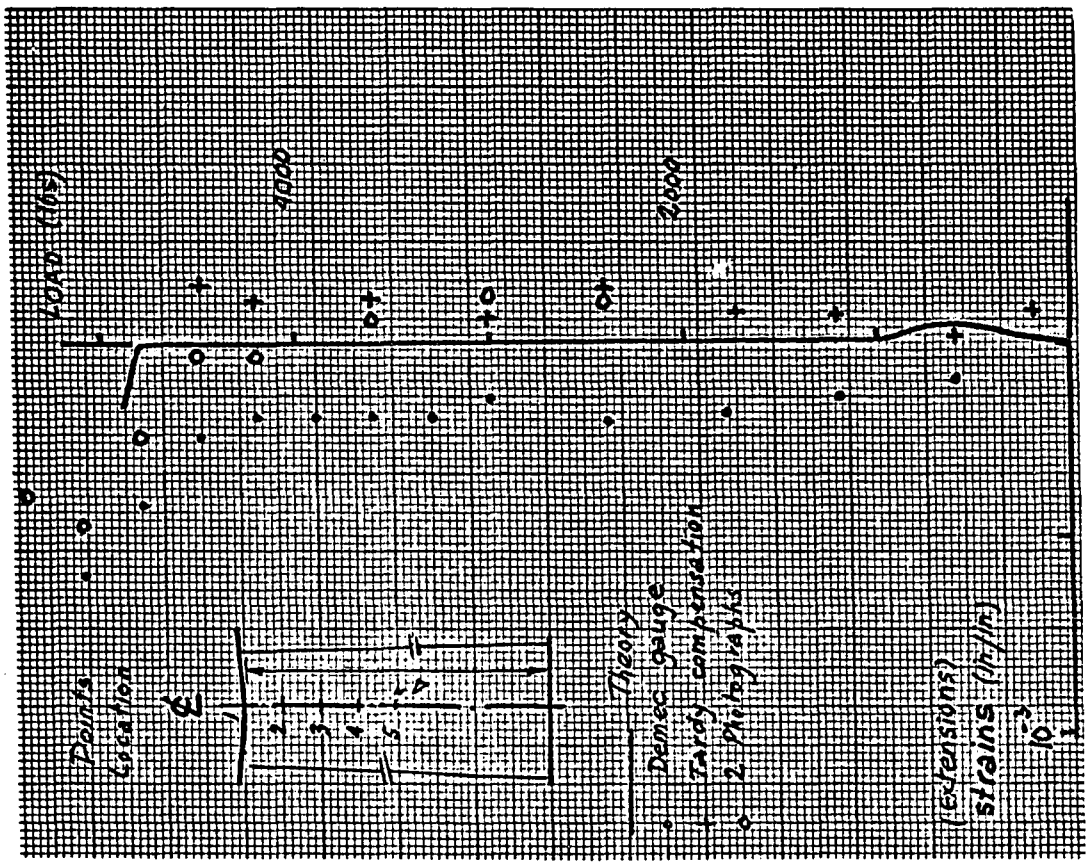

Fig. 3.42 Point 5.

Beam 4 - Load strain curves.

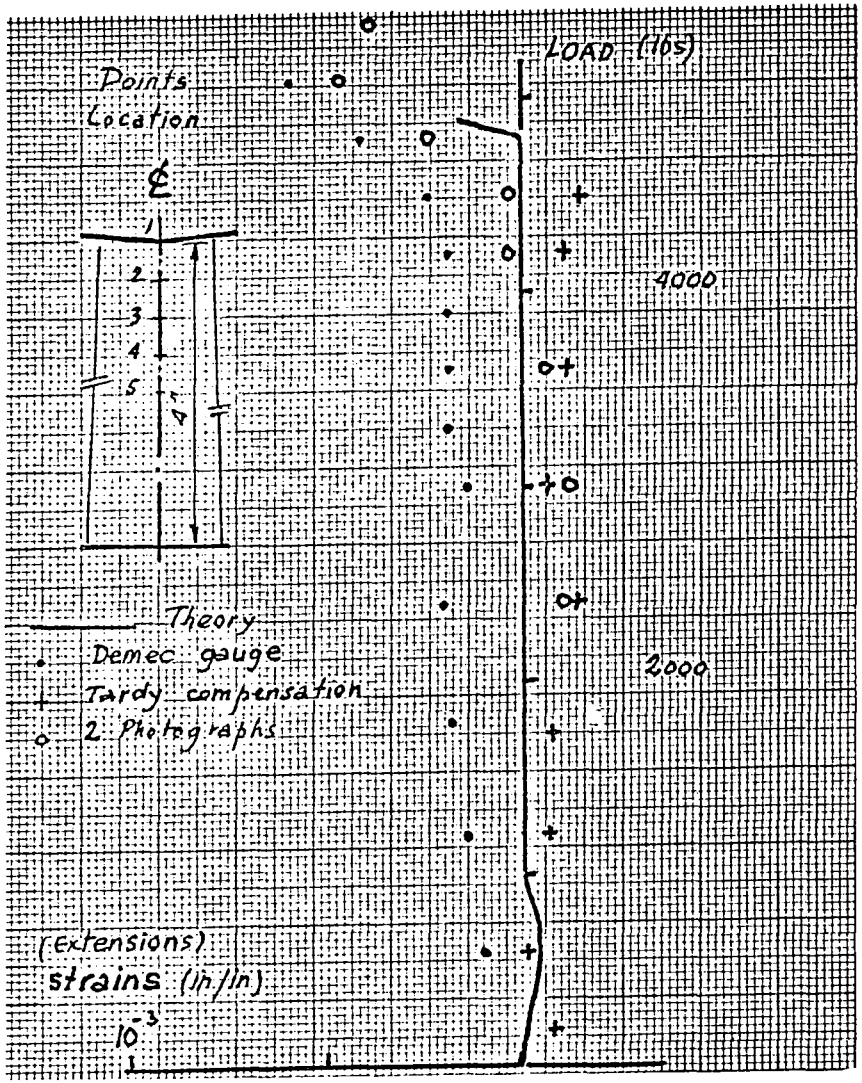

Fig. 3.41 Point 4.

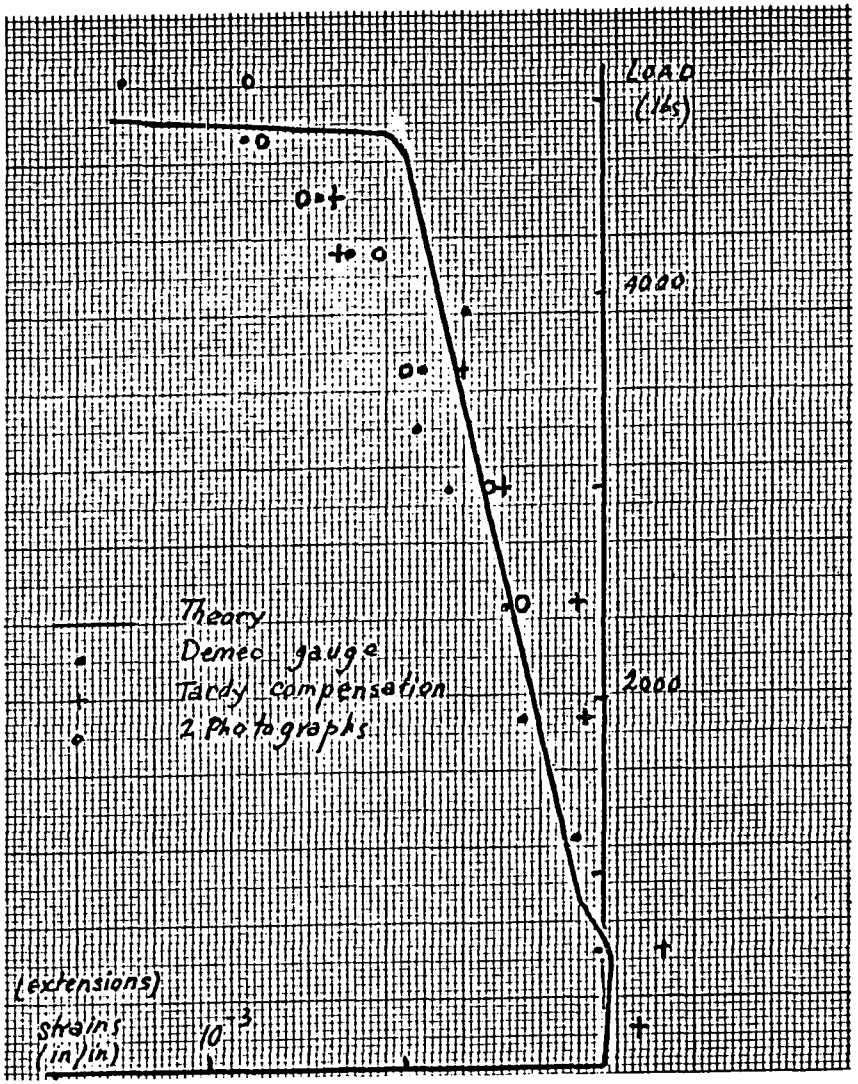

Fig. 3.42 Point 5.

Beam 4 - Load strain curves.

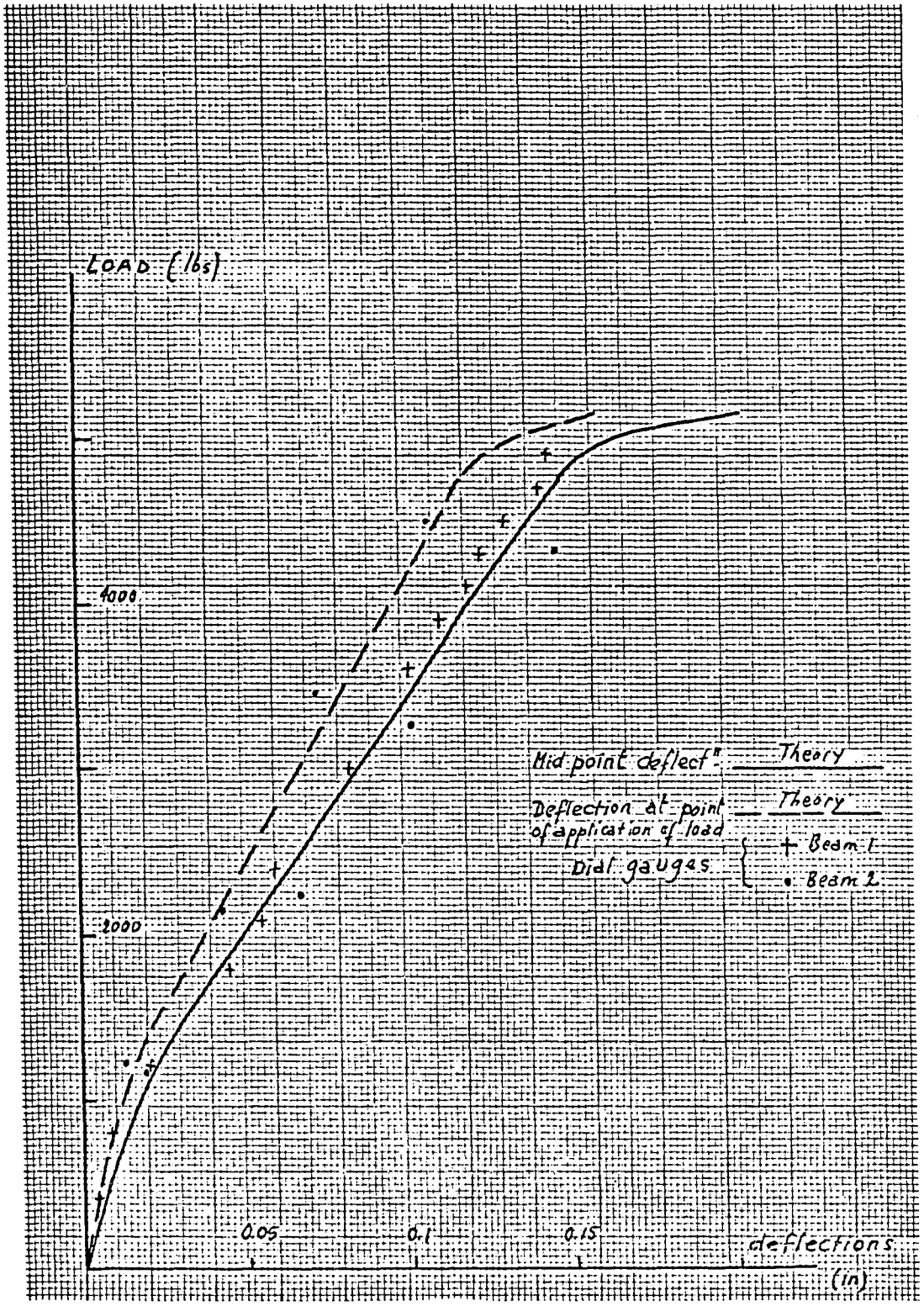

Fig. 3.43 Beams 1 - 2 . Load-deflection curves.

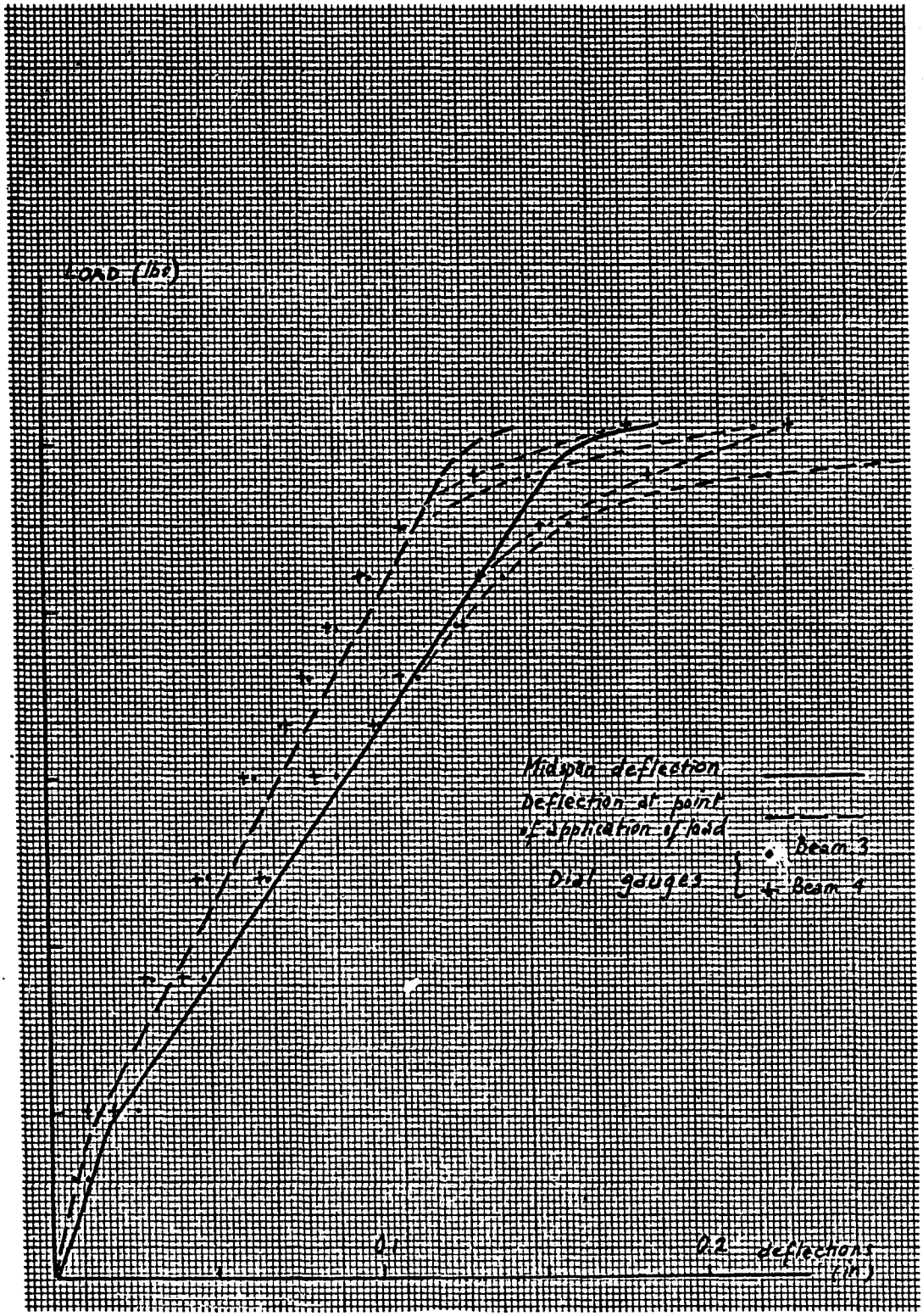

Fig. 3.44 Beams 3 - 4 . Load-deflection curves.

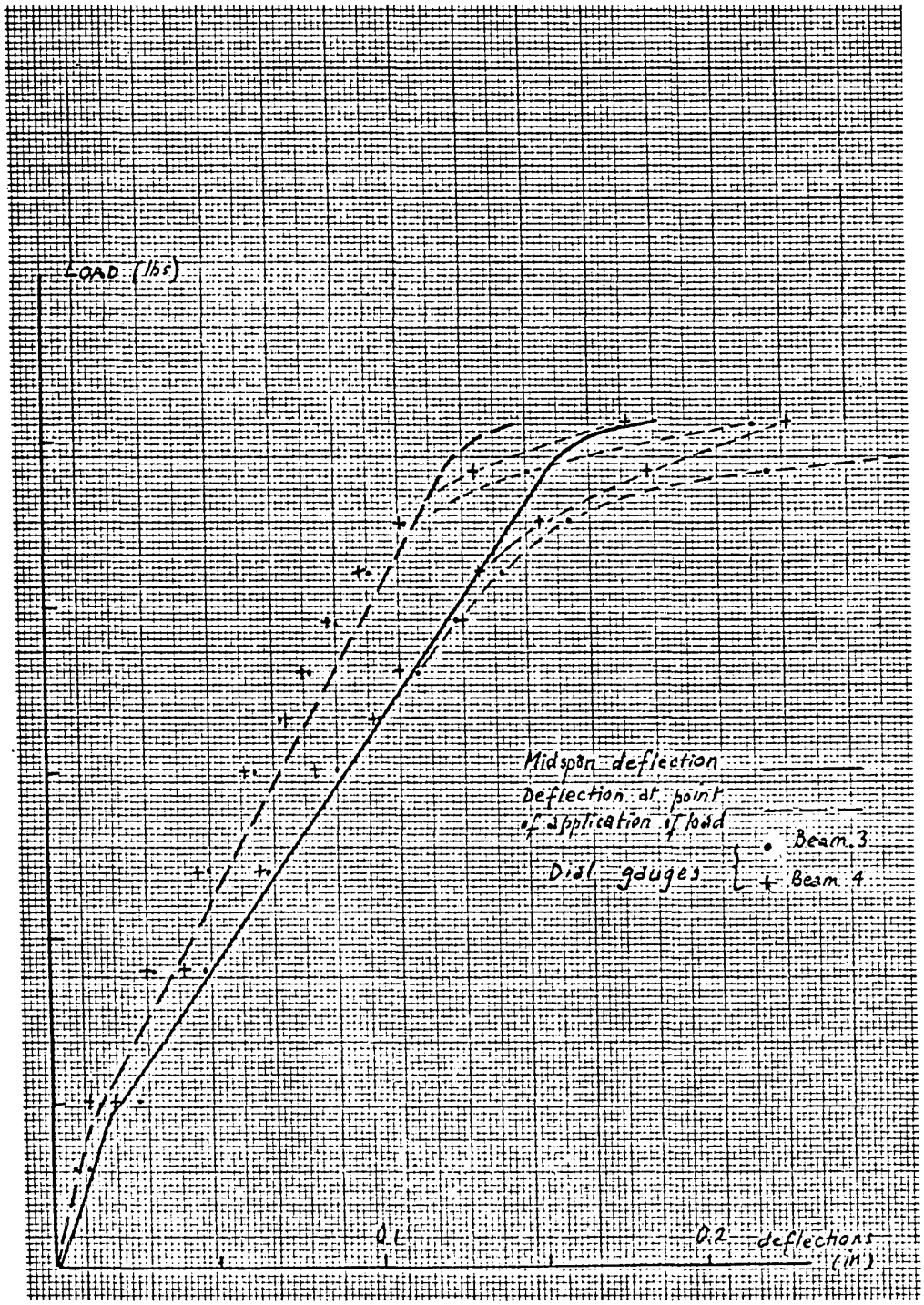

Fig. 3.44 Beams 3 - 4 . Load-deflection curves.

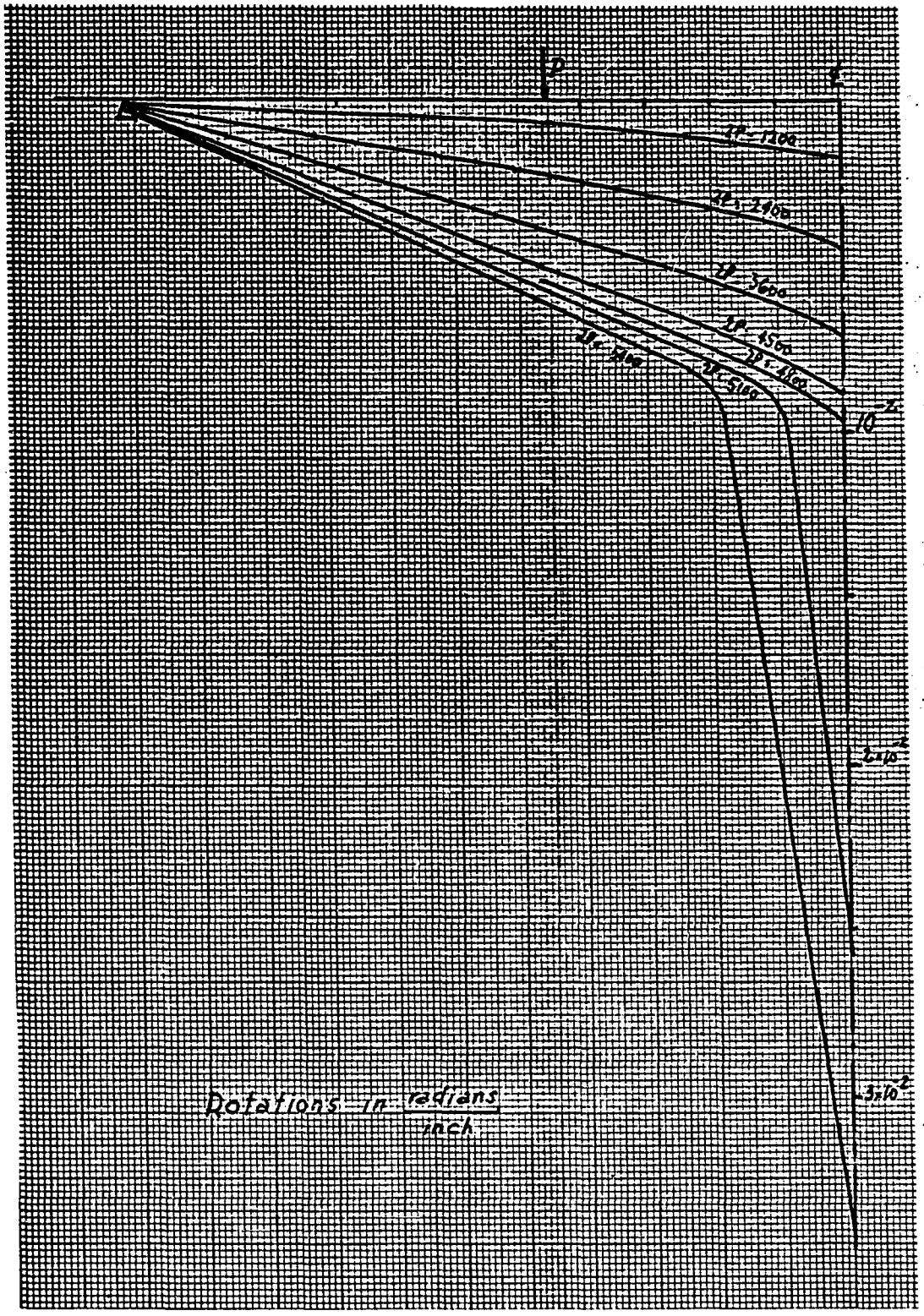

Fig. 3.45 Beams 1 - 2 . Rotations along the beams.

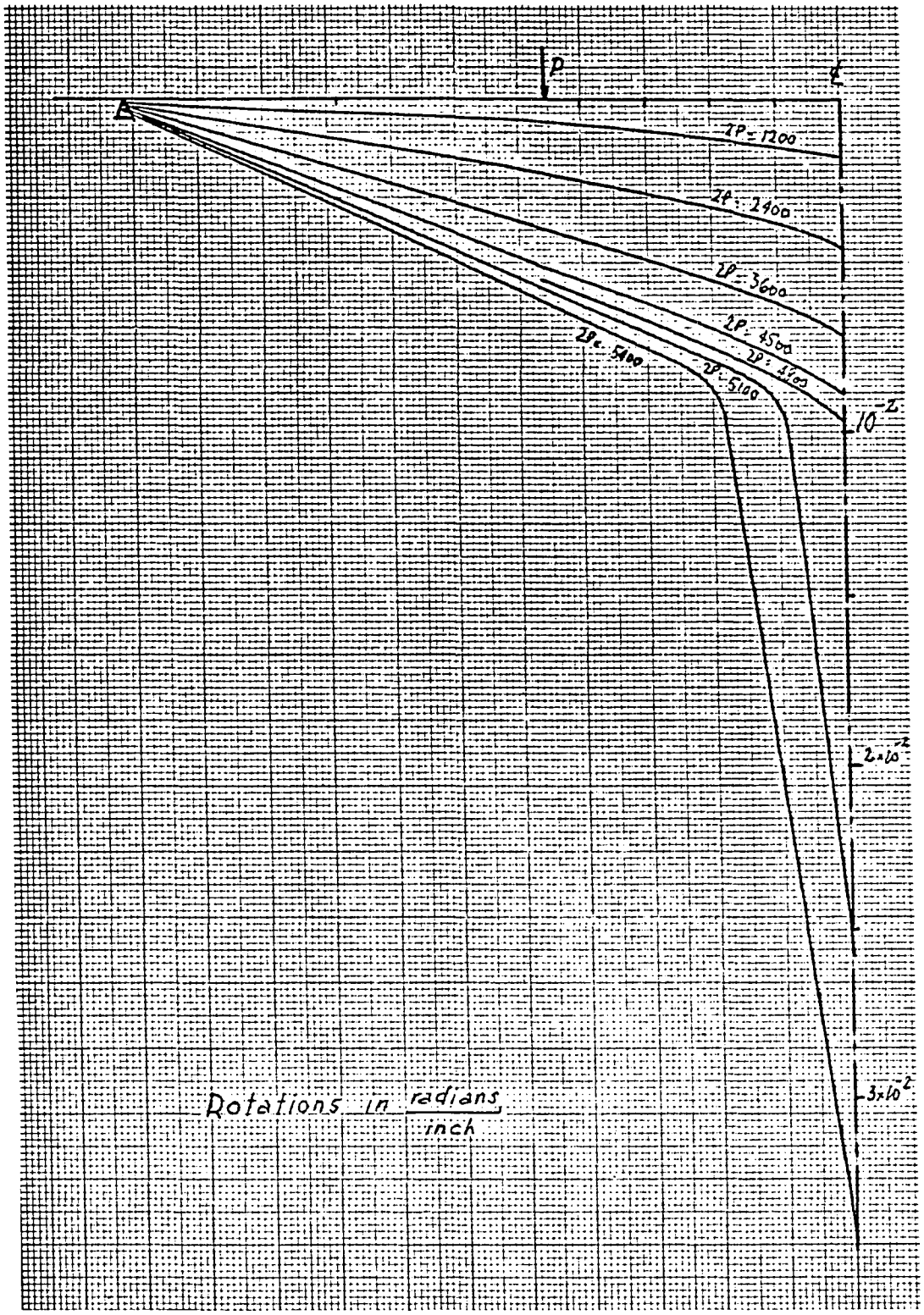

Fig. 3.45 Beams 1 - 2 . Rotations along the beams.

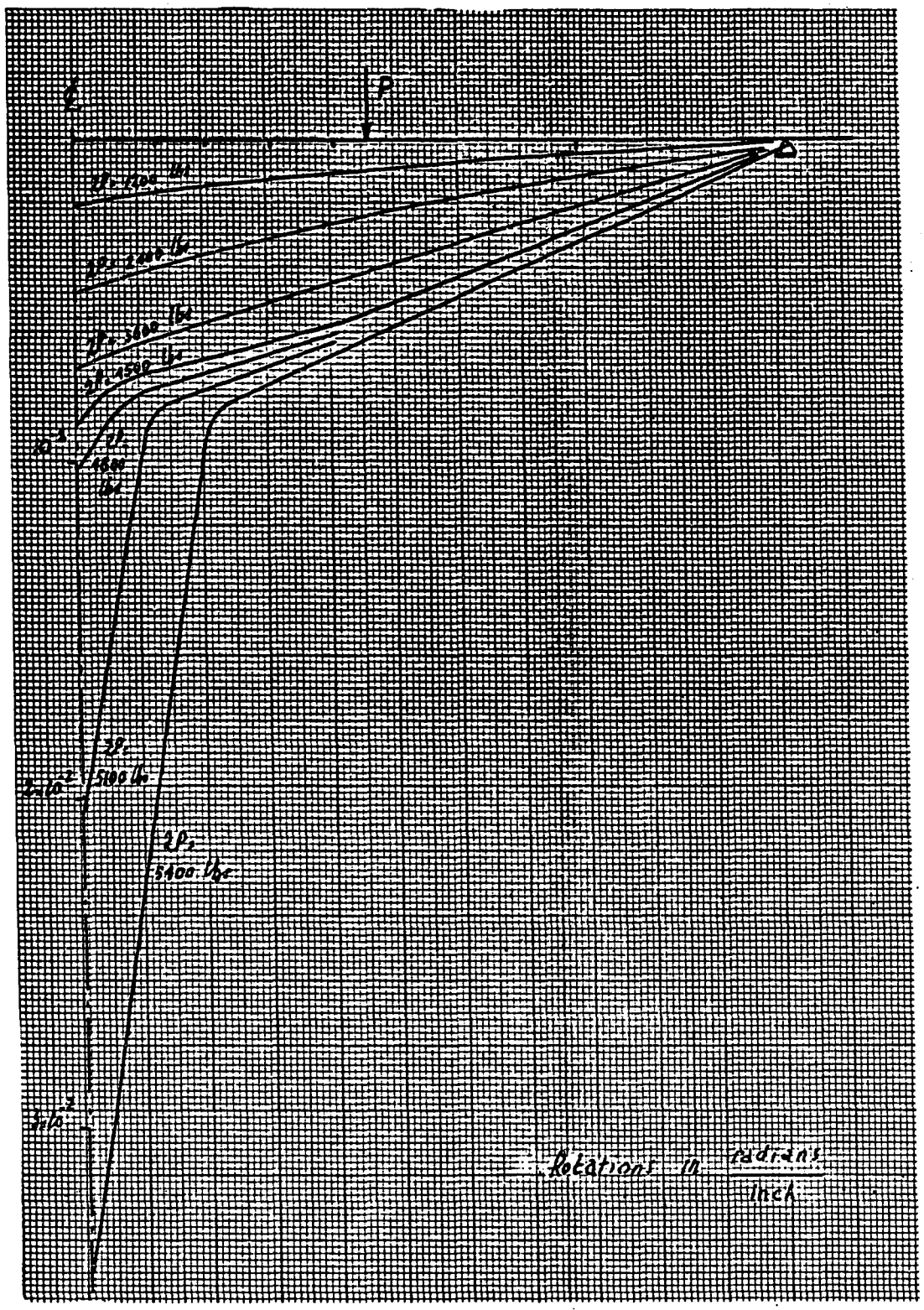

Fig. 3.46 Rotations along the beams.

Beams 3 - 4.

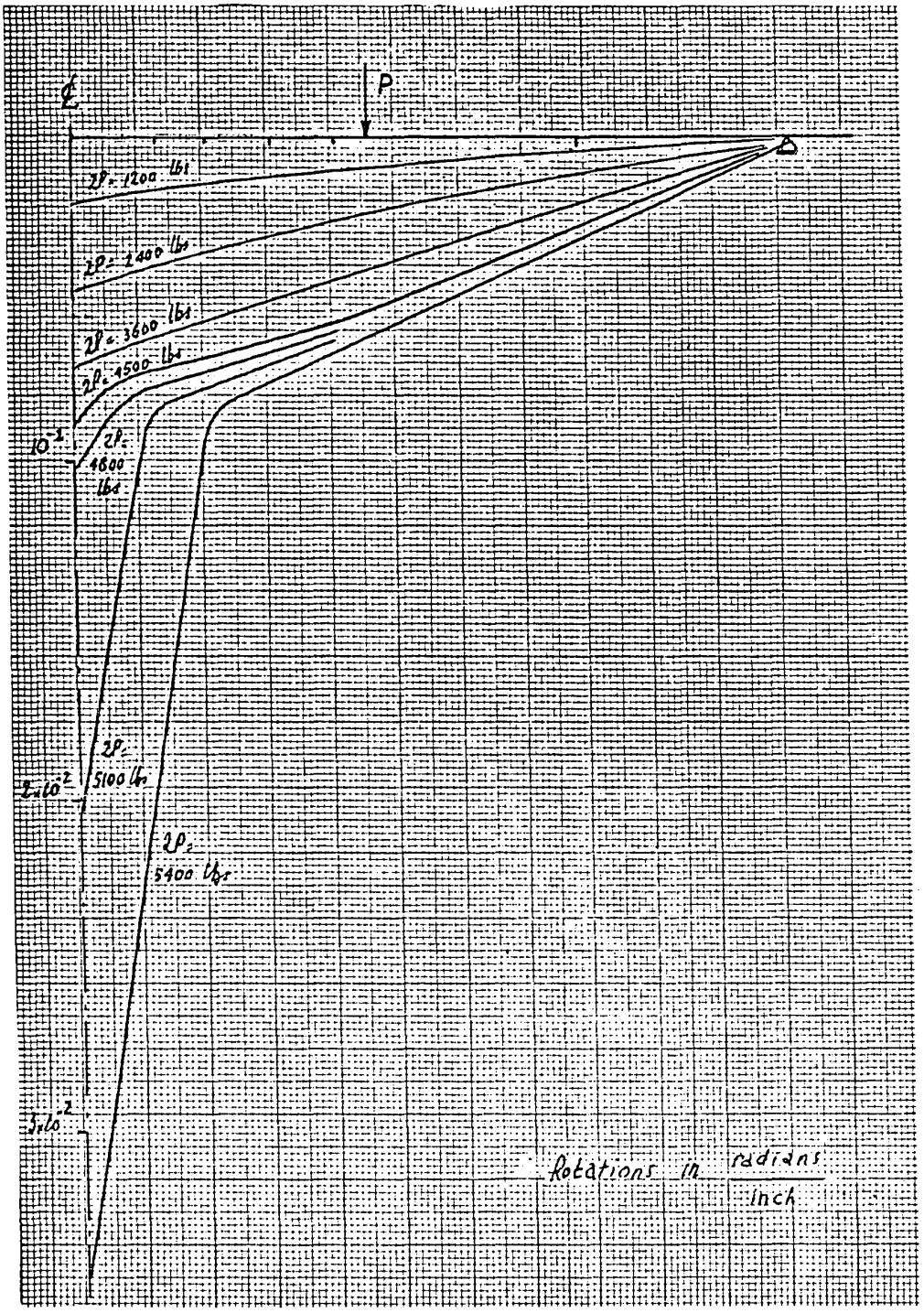

Fig. 3.46 Rotations along the beams.

Beams 3 - 4.

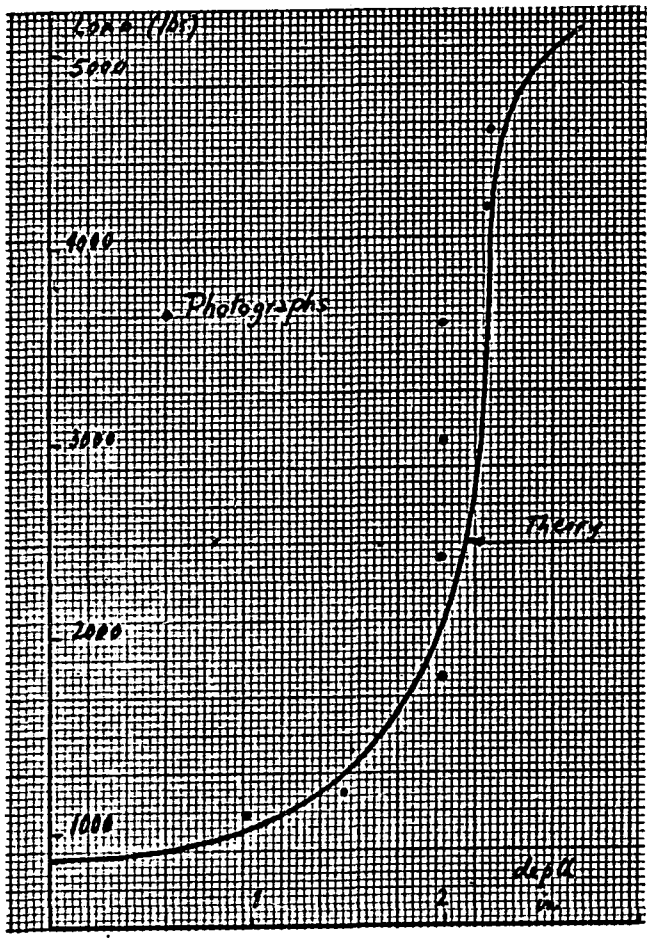

Fig. 3.47 Beams 1 and 2 .

Load-depth of cracks curves.

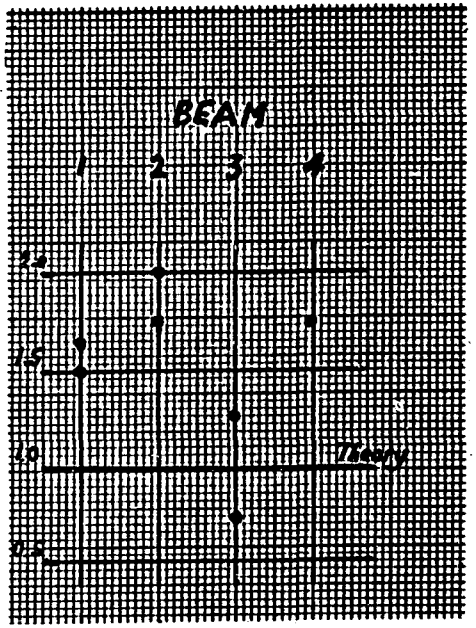

crack spacing

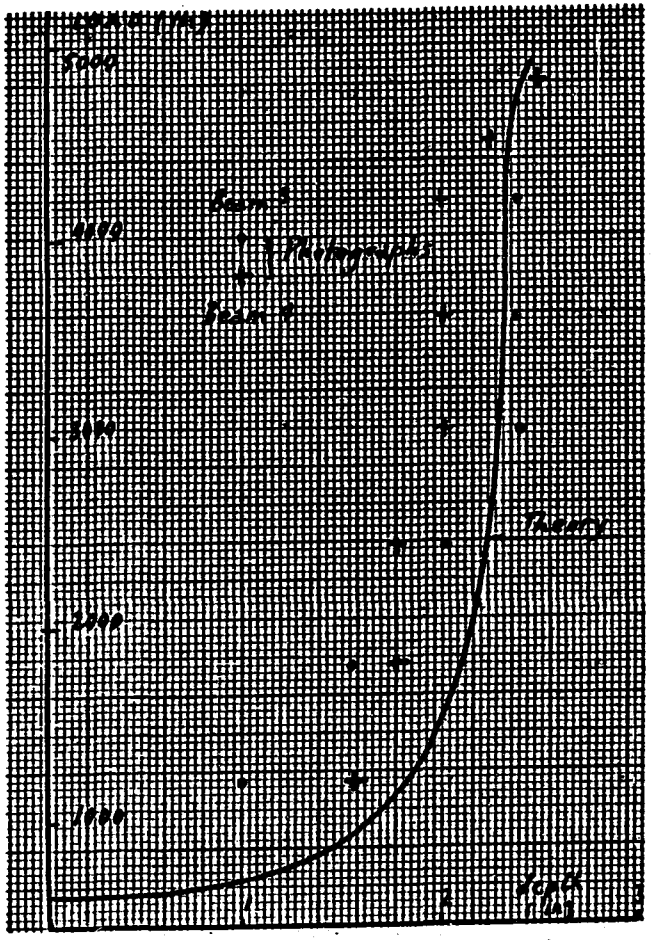

Fig. 3.48 Beams 3 - 4 .

Load depth of cracks curves.

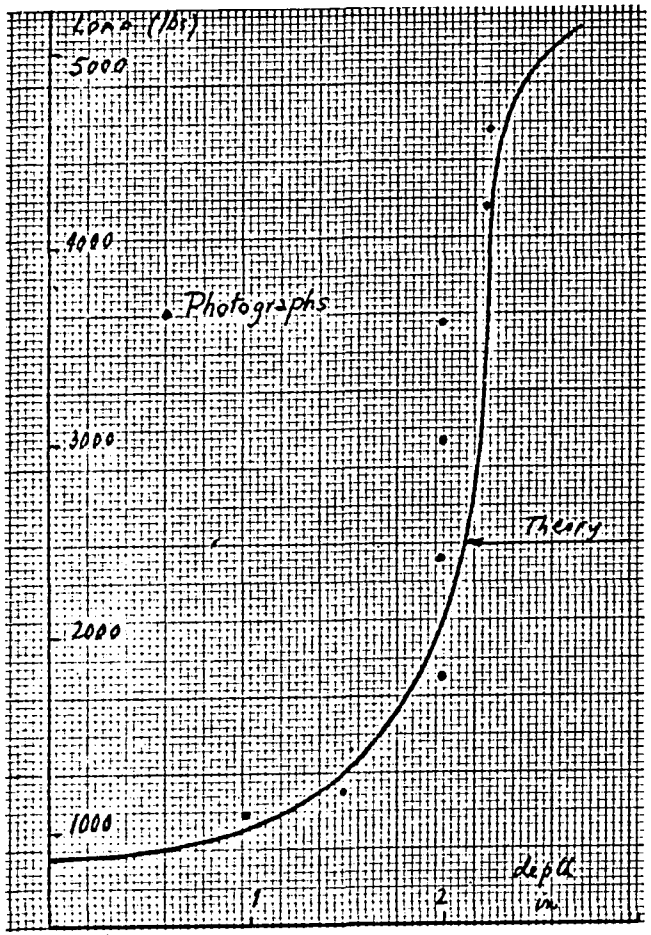

Fig. 3.47 Beams 1 and 2 .

Load-depth of cracks curves.

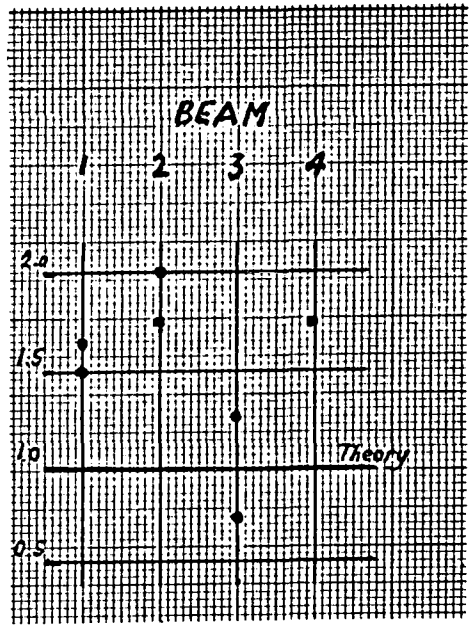

crack spacing

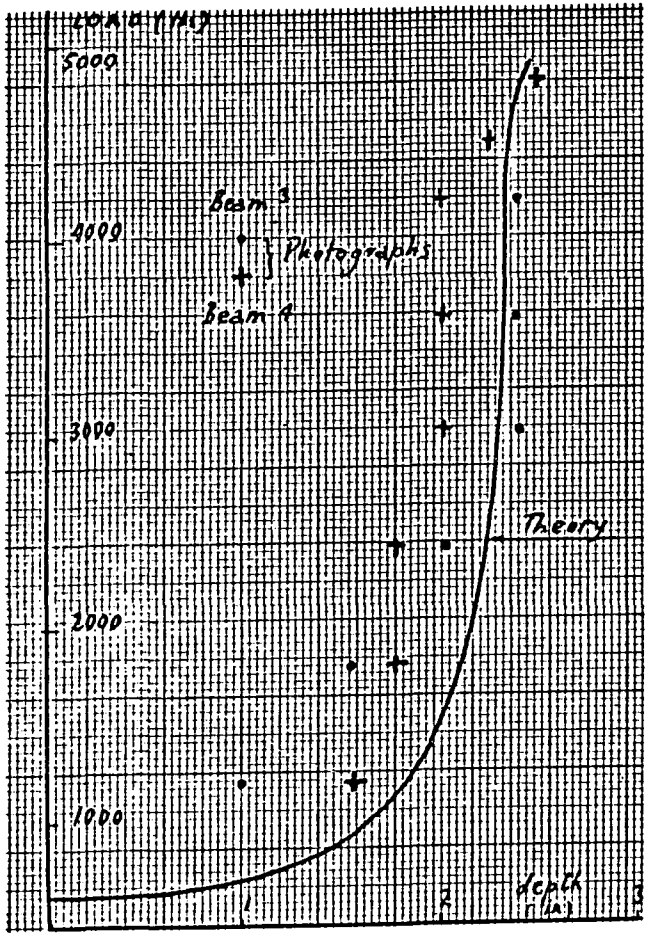

Fig. 3.48 Beams 3 - 4 .

Load depth of cracks curves.

3.5.4 Experimental set up.

The measuring devices used in the experiments were the following: dial gauges, Demec gauges, strain gauges, and Photostress equipment. The testing machine was a Riehle hydraulic machine, Beam No. 1 had the set up shown on fig 3.49 .

A wide flange member, 6 inches deep, was laid skew across the plateau of the machine; steel blocks and rollers supported the beam and provided a clearance of about 5 inches under the beam, for the dial gauges.

These were located at mid-span, at three inches on either side, and near the supports; a smaller member, 3 inches high, distributed the applied load to two points situated 18 inches apart.

Two small plaster pads were cast at these points; when dry, they were filed to provide good contact to the 1/2" rollers which transmitted the loads.

The application of the Photostress plastic to the beams included the following operations:

- roughening of the surface with sand paper,
- probing with a chisel in order to open subjacent cavities,

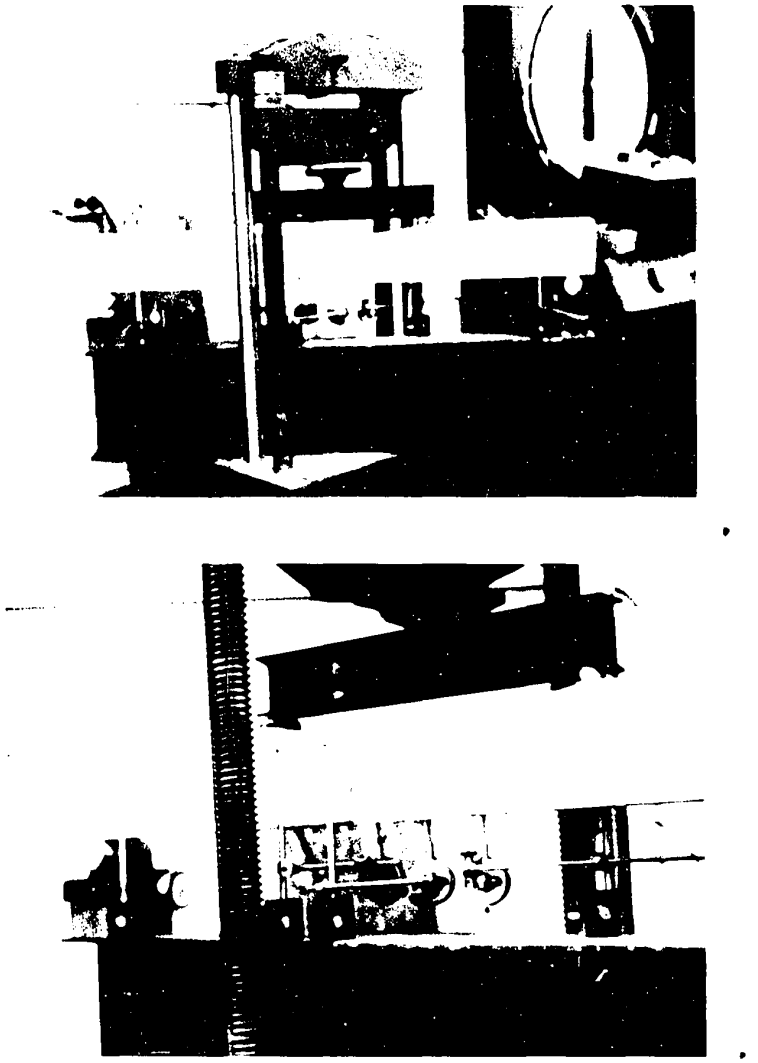

Fig. 3.49 Beam 1 . Experimental set up.

- filling all cavities with a mix of silica sand and epoxy resin,
- curing of that precoat;
- application of the plastic, as for the prisms.

A reference grid, made of diagonals in order not to interfere with the fringes was traced on the plastic with a felt marker.

Five strain gauges were applied, but they failed to give accurate results.

The Photostress readings were made in normal and oblique incidence, using the Budd oblique incidence attachment.

Photographs were taken at each load stage; it took not less than four different shots through the oblique incidence attachment to cover a reasonable area of the hinging region.

These operations took considerable time, so that, when the beam began to creep, it became quasi impossible to obtain simultaneous records of the fringe pattern, in normal and oblique incidence.

This led to the design of the larger oblique incidence attachment. described and shown in section 3.2 . In order to accomodate this new piece of equipment, the beam had to be moved 5 inches from the vertical

axis of the machine, hence the additional cantilever beam, tension rods and rollers that are visible on fig 3.50 .

This new set up was used for beams 2,3 and 4. No more strain gauges were used, but 8 pairs of Demec points were glued to the back of the beam, across the section of symmetry, in order to record the average strains at 8 equidistant levels of the beam.

Also, dial gauges were placed under the points of application of the load, near the supports and at mid-span.

They had to be removed shortly before failure occurred.

The camera used was an Asahi Pentax fitted with the Takumar 135 lens, and an extension tube; it was supported by the Camera attachment described in section 3.2 .

Kodachrome II films were used for beam I; however these films are compensated for natural light, and yielded pictures with a brownish colour.

Ektachrome High speed, type B films, for artificial light ($3200^{o}k$), were used for beams 2,3, and 4.

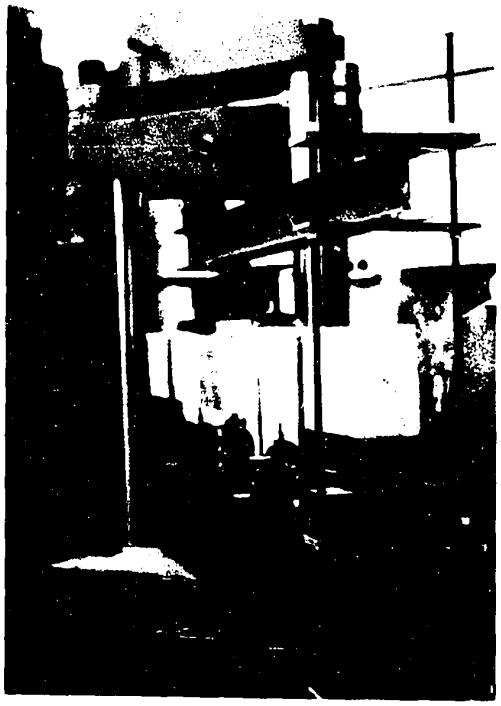

Fig. 3.50 Beams 2 to 4 :
Experimental set up.

An Asahi Pentax lightmeter with through vision of the subject and double sensitivity scales was used, with excellent results.

3.5.5 Experimental results.

The results of the experiments may be divided in two classes, according to whether they have been obtained from mechanical gauges, or the Photostress method.

3.5.5.1 Behaviour of the beams - Results of mechanical gauges.

A) The ultimate loads calculated for beams 1-2 and 3-4 were 5170 lbs. and 4900 lbs. respectively. The actual failure loads were 5790 (+ 14%), 5380 (+ 4%), 5250 (+ 7%) and 5270 lbs. (+ 7%)

In all cases, the beams resisted beyond the above calculated load; Figure 3.52 shows that in all cases, the crack that led to the failure of the beam developed just outside the section of minimum resistance.

B) The strain distribution, as averaged over 4 inches by the Demec gauge may be found on figs. 3.28 to 3.44 , and on fig. 3.51, where a sample strain profile is given (beam no. 4).

Figure 3.51 shows that the strains, so obtained, are in accordance with the assumptions made: their distribution is linear, and the ultimate strain recorded is 3.1×10^{-3} in./in. (at 95% of ultimate).

The correlation between measured and calculated strains is good, with a tendency to measure larger strains in the tensile zone.

This may be due to the shape of the beam itself, and to the position of the neutral axis.

C) The deflections measured (fig 3.43 - 44) are in good accordance with those calculated, at least up to yield.

The necessity to remove the gauges before failure, and the presence of creep made measurements very difficult, past that point, with the instrumentation used.

Due to the reinforcing effect which seems to have taken place due to the presence of the plastic and its backing of epoxy the deflections recorded near ultimate were above those expected (beams 3 and 4) .

It is felt however, that the results obtained are sufficient to establish the validity of the assumptions and procedures adopted to develop the CONTBEAM program.

The repetitive use of CONTBEAM was, in fact, the only practical means of predicting the deflections and rotations of the tapered beams.

D) Figure 3.51 shows good correlation between the values of k calculated, and those obtained from the strain distribution profile.

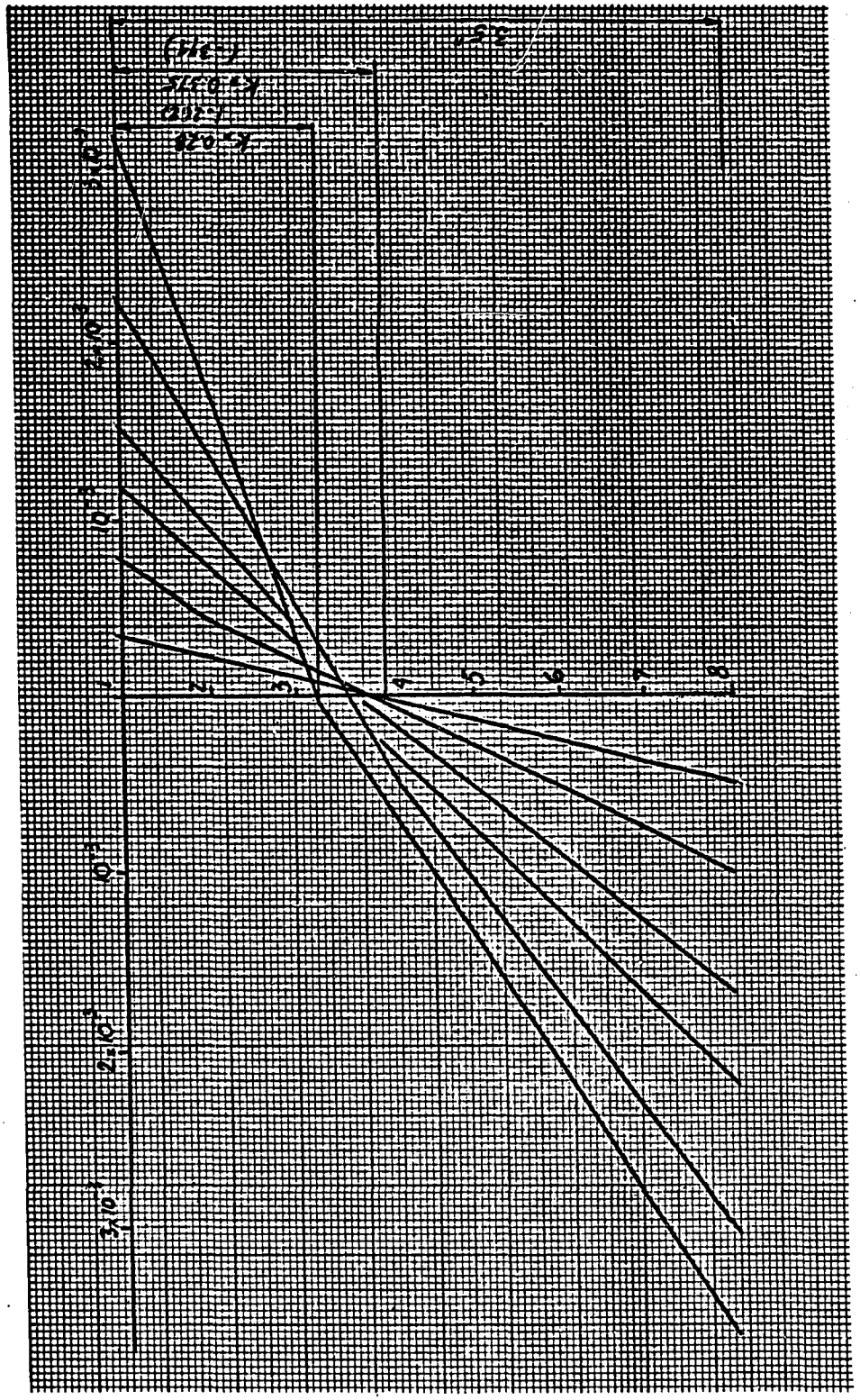

Fig. 3.51 Beam 4 . Strain distribution at section of symmetry.

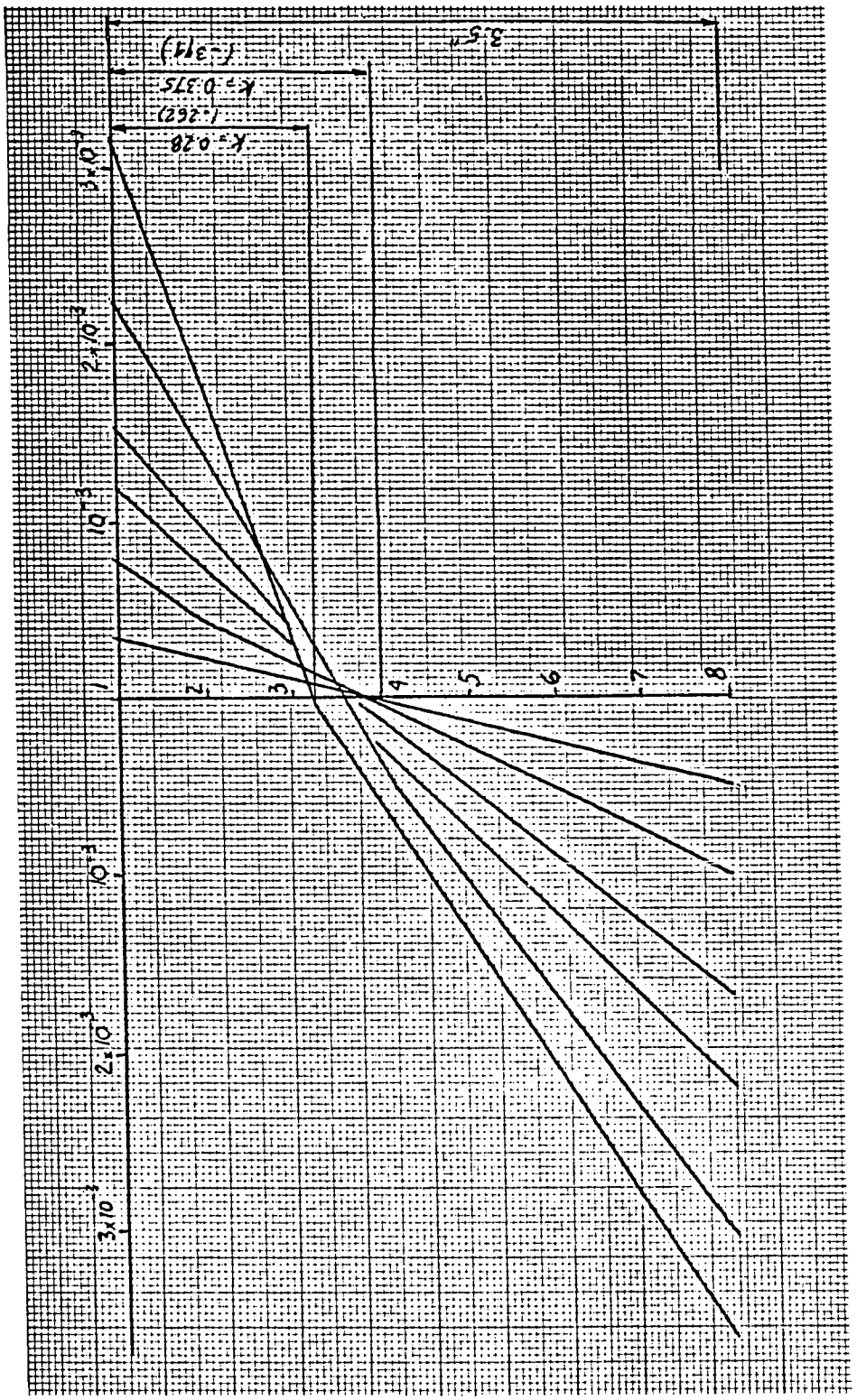

Fig. 3.51 Beam 4 . Strain distribution at section of symmetry.

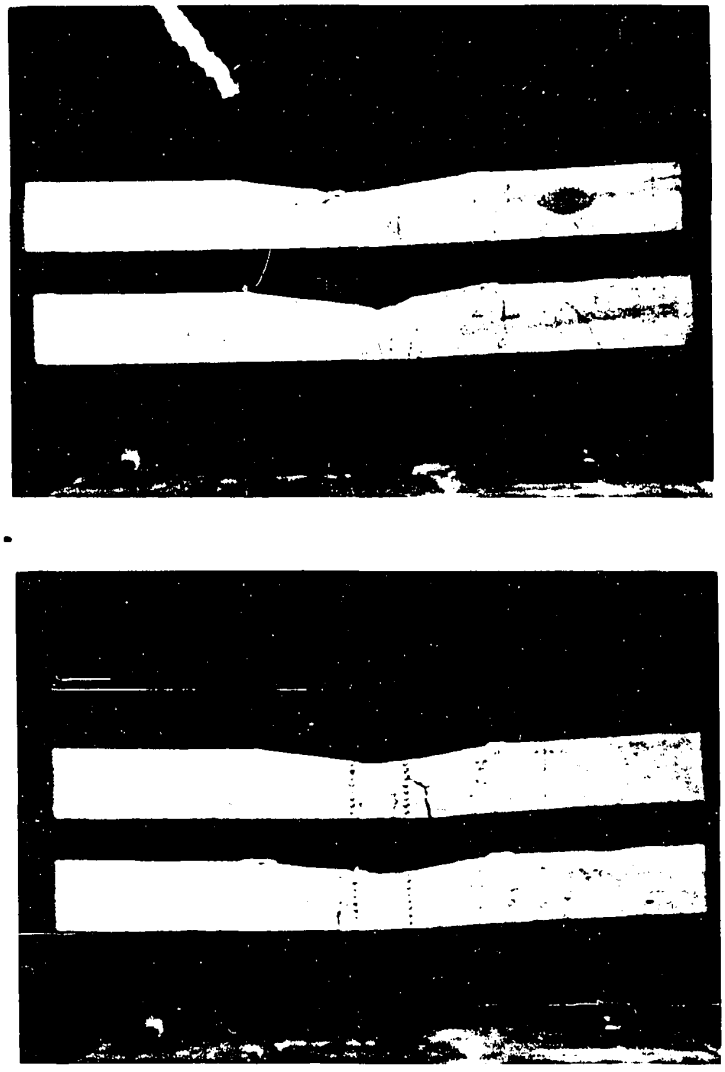

Fig. 3.52 Beams 1 to 4 after failure.

3.5.5.2 The results obtained by the Photostress Technique.

3.5.5.2.1 Beam No. 1.

In section 3.5.4 above, the procedure for the collection of data from the test on beam No. 1 has been digressed upon. It consisted of taking photographs of the fringe pattern in normal and oblique incidences, at various loads.

These photographs were processed into transparencies (see Appendix 2) which were projected on sheets of tracing paper, stuck to the clear glass of a viewing frame.

For normal incidence photographs, the fringe contours were traced directly on the paper, as well as the image of the grid; for those taken in oblique incidence, the fringe pattern had to be reconstructed on the paper from four or five slides taken through the Budd oblique incidence attachment.

This was made possible by the close grid marked on the plastic, and by the camera support that enabled successive shots to be taken from exactly the same position, relative to the subject.

From these tracings, fringe order profiles in normal and oblique incidence were drawn for the central section of the beam, at each load, and the fringe order at the five points 1 to 5 was determined.

Figs3.53 to 3.55:show sample mappings, in both normal and oblique incidence, and their corresponding fringe order profiles.

When such fringe order values were processed by the FOTSTRES programs large scatter, if not erratic principal strains, were obtained.

This is due to the nature of equations (1.50) and (1.51), used in the program, and which calls for differences of numbers of almost the same order of magnitude; any error made at any stage of the calculations is carried forward, due to the incremental procedure used.

It was thus necessary to plot a load-fringe order curve in each case (fig 3.56), and to revise the values of the fringe orders accordingly.

Transversal strains were not recorded, the values of the longitudinal strains were plotted on figs 3.28 to 3.32 .

The fringe order profiles were very difficult to determine for loads below 1800 lbs. due to the wide spacing of the fringes, although some slides were taken with the analyser at the 0.5 mark; locating the accurate points of zero fringe order was by no means easier.

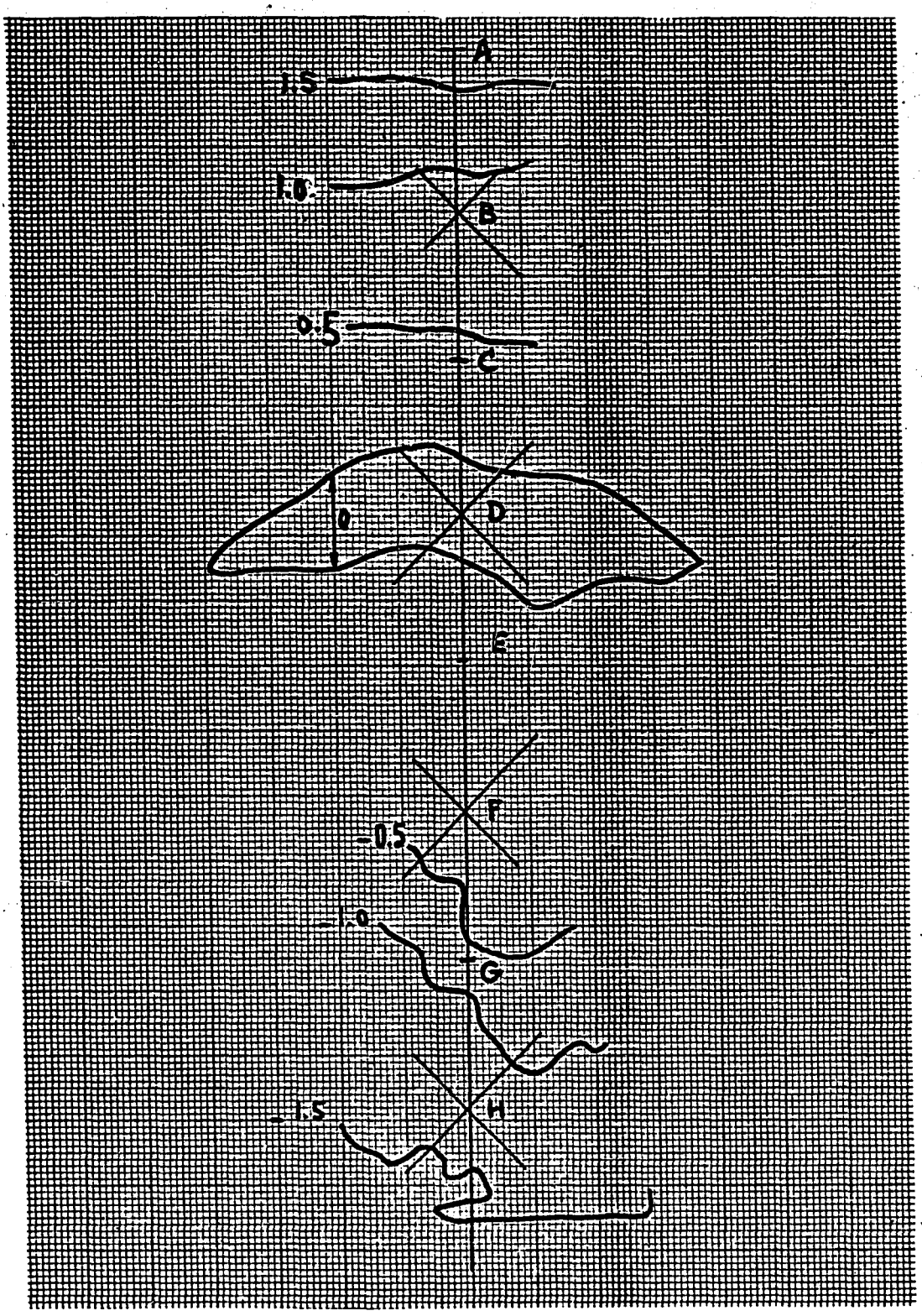

Fig. 3.53 Fringe contours in normal incidence Beam 3 . Applied load 2400 lbs.

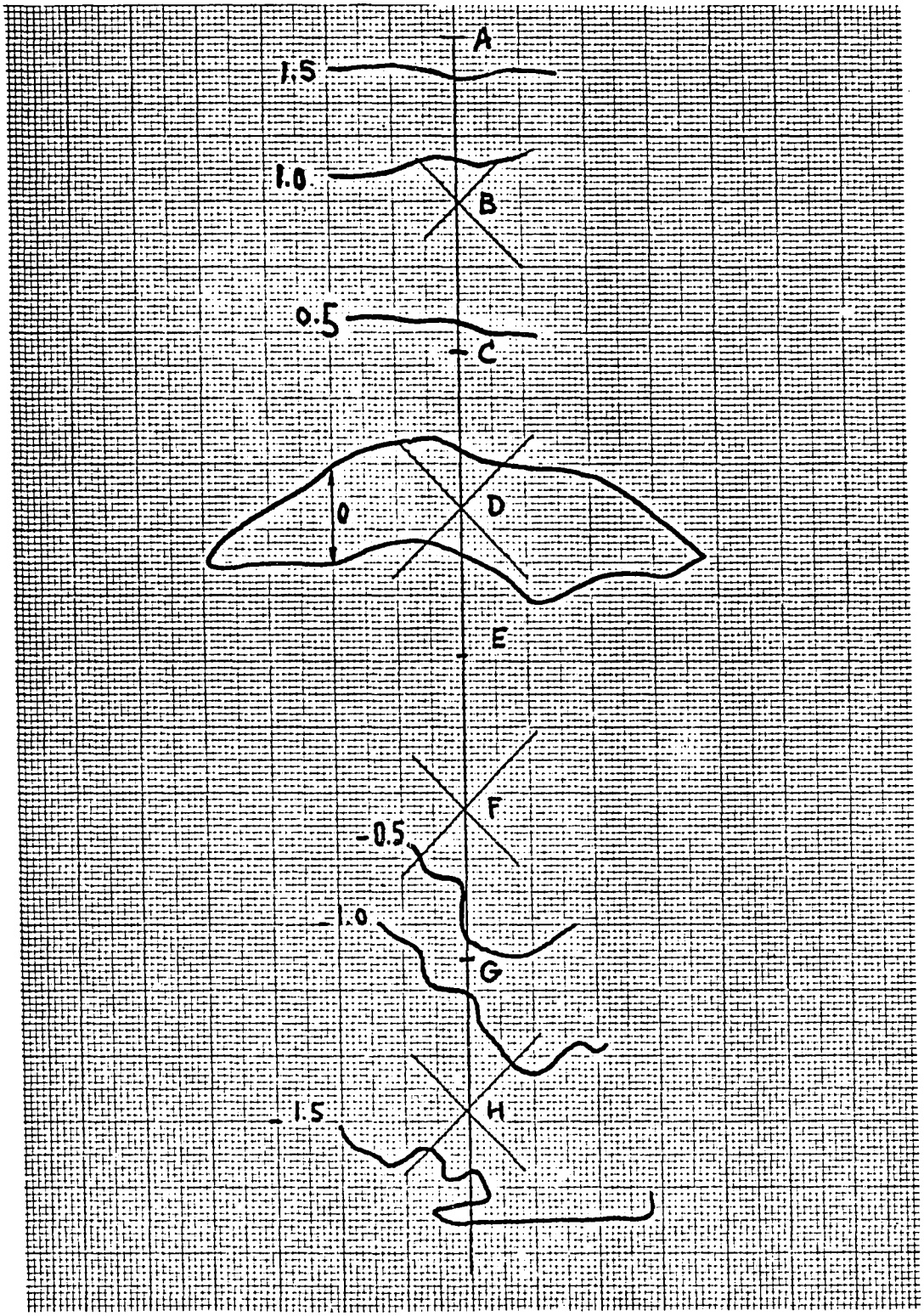

Fig. 3.53 Fringe contours in normal incidence
Beam 3 . Applied load 2400 lbs.

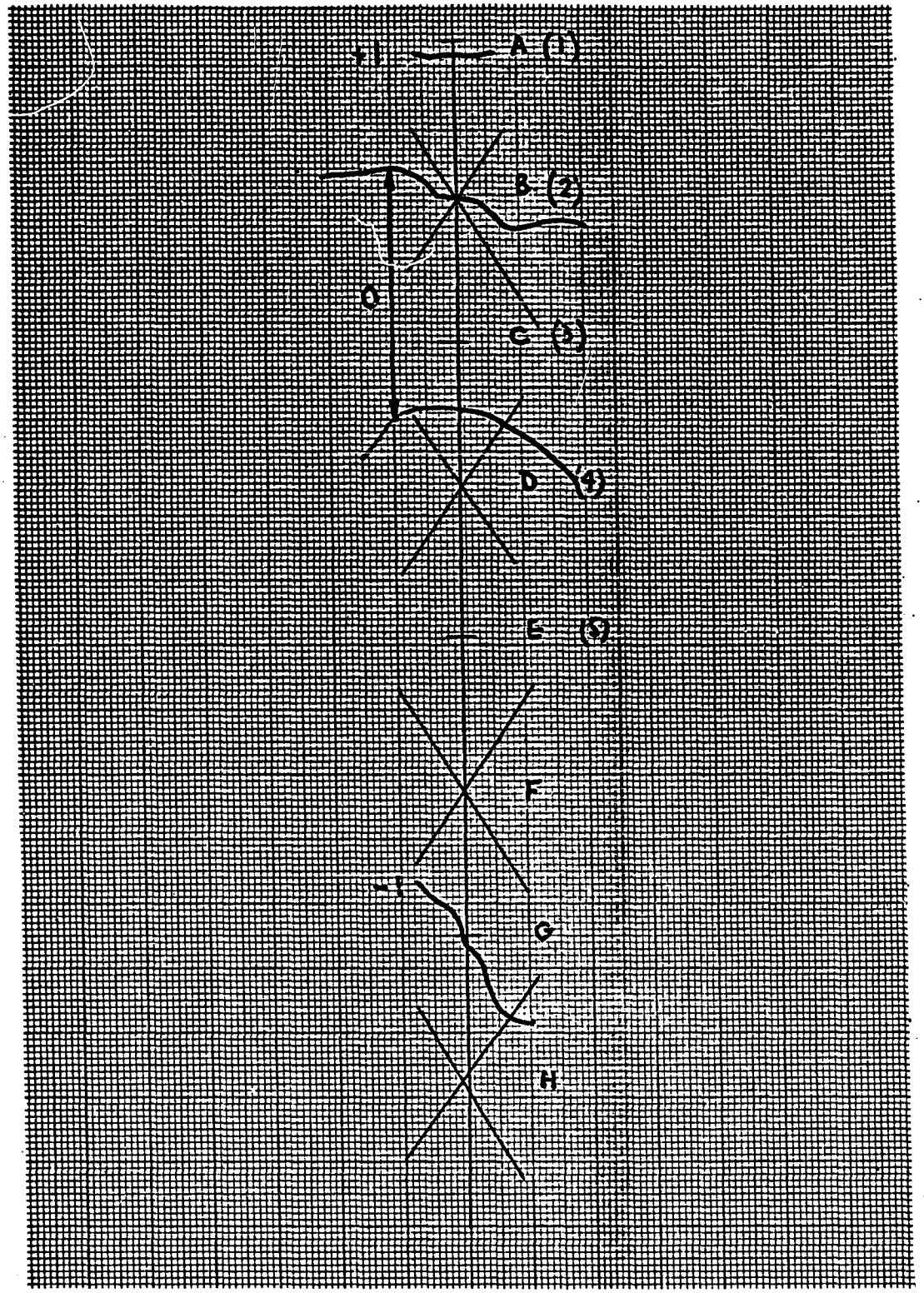

Fig. 3.54 Fringe contours in oblique incidence (45°).

Beam 3 . Applied load 2400 lbs.

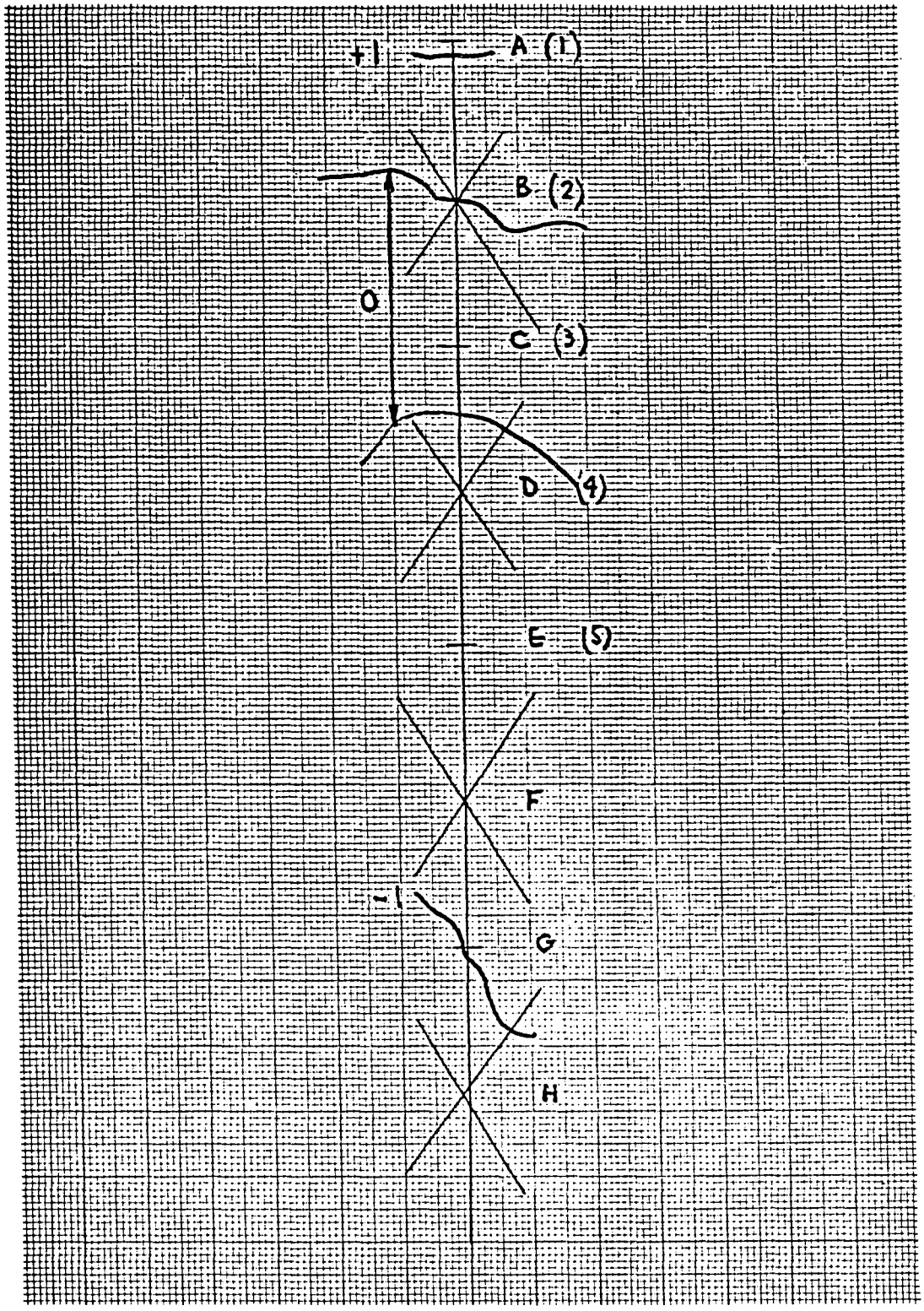

Fig. 3.54 Fringe contours in oblique incidence (45°).

Beam 3 . Applied load 2400 lbs.

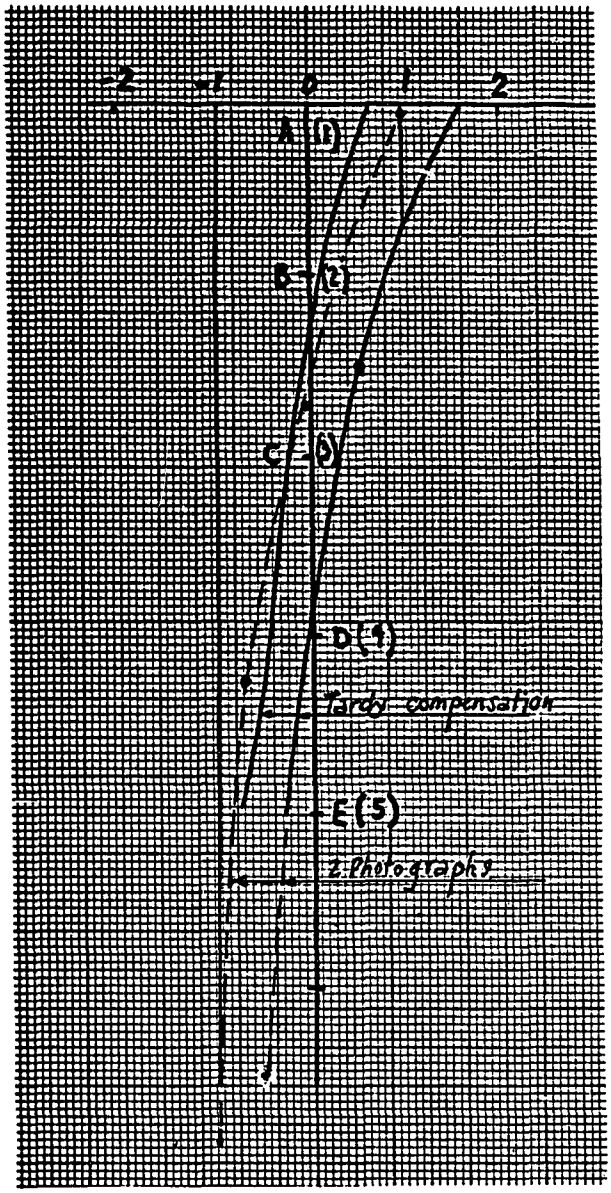

Fig. 3.55 Beam 3 - 2400 lbs.
Fringe order profiles.

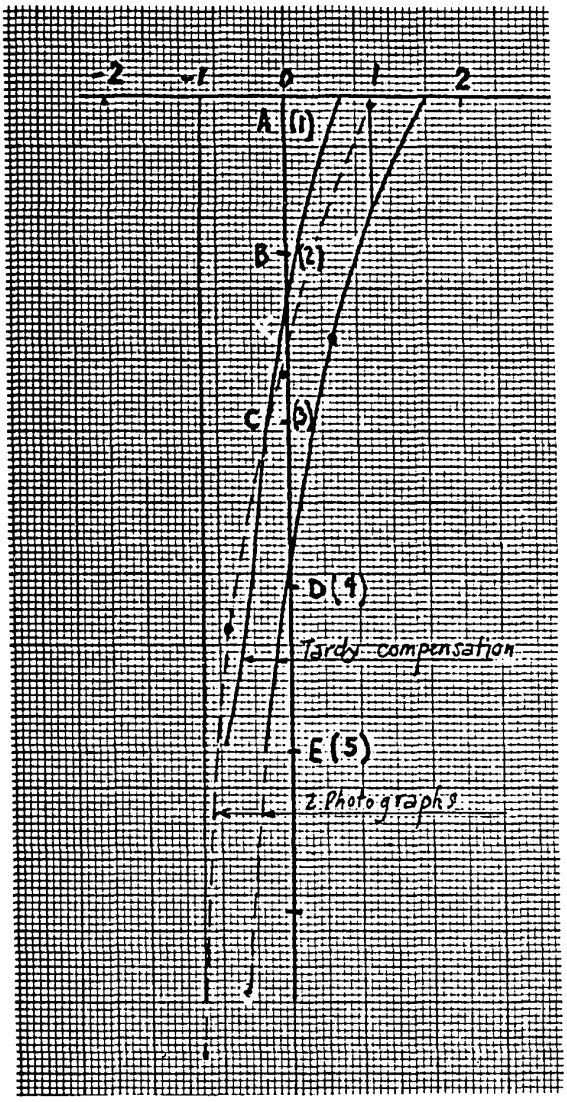

Fig. 3.55 Beam 3 - 2400 lbs.
Fringe order profiles.

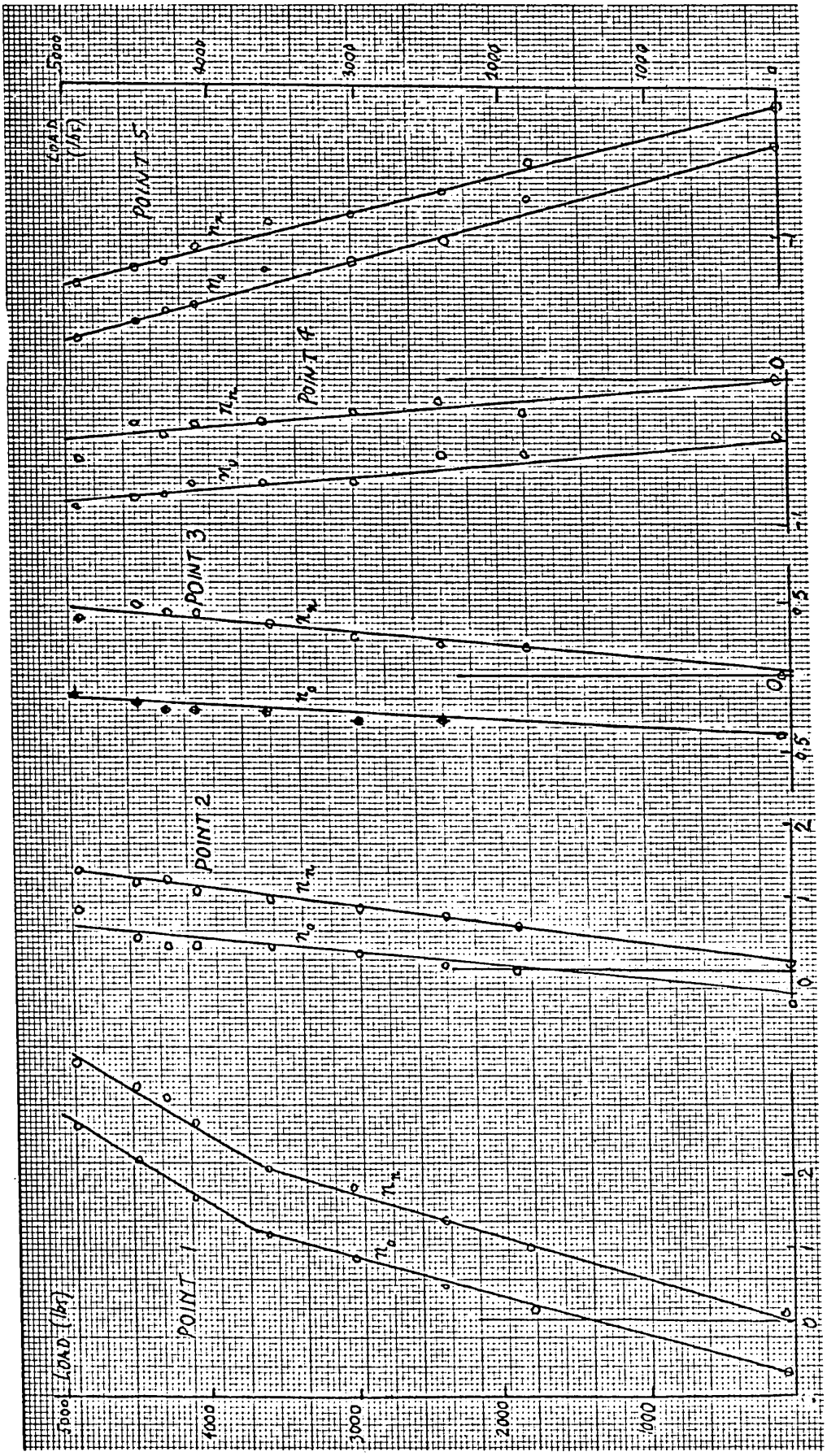

Fig. 3.56 Beam 1 . Load-fringe order curves.

3.5.5.2.2 Beams No. 2 to 4

A similar procedure was used for beams Nos. 2 to 4, except that the Budd oblique incidence attachment was replaced by a larger one which enabled the record of the whole fringe pattern in one photograph.

Three shots were taken, at angles of incidence of 30, 45 and 0 degrees, i.e. normal incidence.

In addition, fringe orders obtained by goniometric compensation at each point were also recorded, for comparison purposes.

The strains were computed in both cases, and plotted on the same graph for comparison (figs 3.28 to 3.42) .

Even then, some minor adjustments of the values had to take place.

Figures 3.57 to 3.59 give the load-fringe order curves for each beam; they show that the values of n_n are very close, whether obtained by interpolation of the fringe order profiles, or point by point compensation.

This is not the case with n_o, (angle of 45^o); the correlation is still good for beam No. 2, it is not so for beams Nos. 3 and 4, especially when the fringe order is positive.

A consistent shift appears then, the angle of the mirrors contained in the attachment were thus checked: they were found to be within one degree of the required angle.

The source of error might rather be found in the fact that the incident beam is not a perfectly parallel one, in spite of the Fresnel lens fitted to the polariscope.

In terms of the longitudinal strains, plotted on figs 3.28 to 3.42, the correlation with the theoretical values is fairly good, if one remembers that the actual shape of the neutral axis in the cracked stages of a reinforced concrete beam is a sagging curve subtended between the extremities of the cracks, rather than a straight line.

This may account for some readings which depart from the theoretical load-strain curve, in a very consistent way. Nevertheless, some large scatter remains.

So far, only the simple case when the principal directions at the points under consideration are aligned with the axes of polarization has been treated.

In order to make the method applicable to all cases, a second reading must be made in oblique incidence, with a different angle (section 1.3.4), and formulae 1.42 (a), (b), (c) must be used.

In order to demonstrate the feasibility of this approach, with the available equipment, these formulae have been used for beams 3 and 4.

When $\sigma_{xy} = 0$, they read:

$$(n_n \times F_n)^2 = (\sigma_x - \sigma_y)^2$$

$$(n_{01} \times F_{01})^2 = (\sigma_x - \sigma_y \cos^2 \theta_1)^2$$

$$(n_{02} \times F_{02})^2 = (\sigma_x - \sigma_y \cos^2 \theta_2)^2$$

where $$F_n = \frac{\lambda}{2\,t\,C\,R} = \frac{\lambda\,E_p}{2\,t\,K(1+\nu_p)R}$$

$$F_{01} = \frac{\lambda \cos\theta_1\,E_p}{2\,t\,K\,R(1+\nu_p)} \quad \text{and} \quad F_{02} = \frac{\lambda \cos\theta_2\,E_p}{2\,t\,K\,R(1+\nu_p)}$$

For $E_p = 480{,}000$ psi, [Ref 1.11], $\theta_1 = 45^\circ$

$\nu_p = 0.38$ [Ref 1.7] $\theta_2 = 30^\circ$

$K = 0.110$ $t = 0.121$,

the system of equations above may be put in matrix form into:

$$\begin{bmatrix} n_n^2 \times 297^2 \\ n_{45}^2 \times 209^2 \\ n_{30}^2 \times 257^2 \end{bmatrix} = \begin{bmatrix} 1 & 1 & -2 \\ 1 & 1/4 & -1 \\ 1 & 9/16 & -3/2 \end{bmatrix} \times \begin{bmatrix} \sigma_x^2 \\ \sigma_y^2 \\ \sigma_x \sigma_y \end{bmatrix}$$

Hence, by premultiplying each side by the inverse of the 3 x 3 matrix,

$$\begin{bmatrix} \sigma_x^2 \\ \sigma_y^2 \\ \sigma_x\sigma_y \end{bmatrix} = 10^4 \times \begin{bmatrix} 3 & 6 & -8 \\ 8 & 8 & -16 \\ 5 & 7 & -12 \end{bmatrix} \times \begin{bmatrix} 8.87 \times n_n^2 \\ 4.37 \times n_{45}^2 \\ 6.60 \times n_{30}^2 \end{bmatrix}$$

From σ_x^2 and σ_y^2, one will derive σ_x, σ_y and ϵ_y. The check consists of multiplying σ_x by σ_y and to compare the product to the value $\sigma_x\sigma_y$ yielded by the system of equations above.

Also, ϵ_y has been plotted on figures 3.33 to 3.37 for beam No. 3, and 3.38 - 3.39 for beam No. 4.

These calculations have been limited to the cases when the quadratic form was applicable, i.e. when $\sigma_x^2 > 0$ and $\sigma_y^2 > 0$.

One should note, however that the signs of σ_x and σ_y may not be obtained from these equations.

Here also, the values of n_{30} were adjusted, according to the load-fringe order curve of fig 3.60 .

Tables 3.10 and 3.11 give the principal values of that calculation.

Finally, the depth and spacing of the cracks, as apparent on normal incidence photographs was plotted on figures 3.47 and 3.48 .

Sample prints of some of the transparencies are given in Appendix No. 2 .

TABLE 3.10

Double oblique incidence measurements.

Beam No. 3.

Pt	load	n_n	n_{45}	n_{30}	σ_x	σ_y	$\sigma_x x \sigma_y$	$\sigma_x \sigma_y$	% diff.	ϵ_y
1	2400	1.55	1.00	1.05	565	940	53.2	49.4	7.15	1.51
	3000	1.90	1.40	1.55	460	852	39.2	29.6	13.40	1.40
	3600	2.35	1.00	2.10	388	758	29.5	12.5	57.5	1.27
	4200	3.10	2.30	2.60	594	1210	72.0	50.0	30.5	2.00
	4500	3.60	2.80	3.00	830	1500	124.0	91.0	37.5	2.47
2	2400	0.84	0.35	0.30	415	791	32.8	27.8	15.2	1.30
	3000	1.00	0.55	0.55	431	704	30.4	33.5	10.2	1.12
	3600	1.32	0.80	0.85	498	835	41.6	39.2	6.0	1.32
	4200	1.65	0.97	1.10	570	982	56.0	50.7	9.5	1.59
	4500	1.92	1.20	1.25	525	870	45.6	39.9	12.5	1.40
3	2400	0.32	-0.10	-0.10	154	252	3.88	3.92	0.1	0.41
	3000	0.45	0.00	0.00	222	362	8.10	8.20	1.2	0.58
	3600	0.50	0.10	0.10	252	411	10.70	10.52	0.7	0.65
	4200	0.62	0.16	0.20	296	488	14.40	13.47	0.6	0.78
	4500	0.70	0.20	0.25	451	648	29.3	29.00	0.1	0.99
4	2400	0.00	0.45	0.10	217	244	5.30	5.36	0.1	0.34
	3000	0.00	0.40	0.20	144	117	1.68	1.72	0.02	0.23
5	2400	0.30	0.60	0.30	266	310	8.25	7.86	4.7	0.43
	3000	0.45	0.65	0.40	282	348	9.80	8.5	13.3	0.50
	3600	0.60	0.70	0.55	258	331	8.55	7.1	1.7	0.49
	4200	0.70	0.80	0.70	202	141	4.90	2.5	49.0	0.34
	4500	0.80	0.90	0.80	158	145	2.30	-0.3	——	0.18

TABLE 3.11

Beam No. 4.

P_t	load	n_n	n_{45}	n_{30}	σ_x	σ_y	$\sigma_x x \sigma_y$	$\sigma_x \sigma_y$	% diff.	ϵ_y
1	2400	1.30	0.65	0.70	547	855	47	48.6	3.1	1.35
	3000	1.50	1.00	1.10	455	790	36.4	33.8	7.15	1.30
	3600	2.10	1.30	1.55	581	1080	62.5	55.6	11.0	1.79
	4200	2.40	1.80	2.00	592	1080	64	48.0	25.0	1.78
2	2400	0.60	0.0	0.10	300	493	14.8	15.0	0.01	0.79
	3000	0.70	0.0	0.20	350	550	19.2	18.43	0.04	0.87
	3600	0.85	0.25	0.30	398	660	26.2	25.37	0.03	1.06
	4200	1.00	0.35	0.40	460	764	35.0	35.10	0.00	1.22
	4500	1.10	0.50	0.50	504	828	41.6	41.03	0.01	1.32

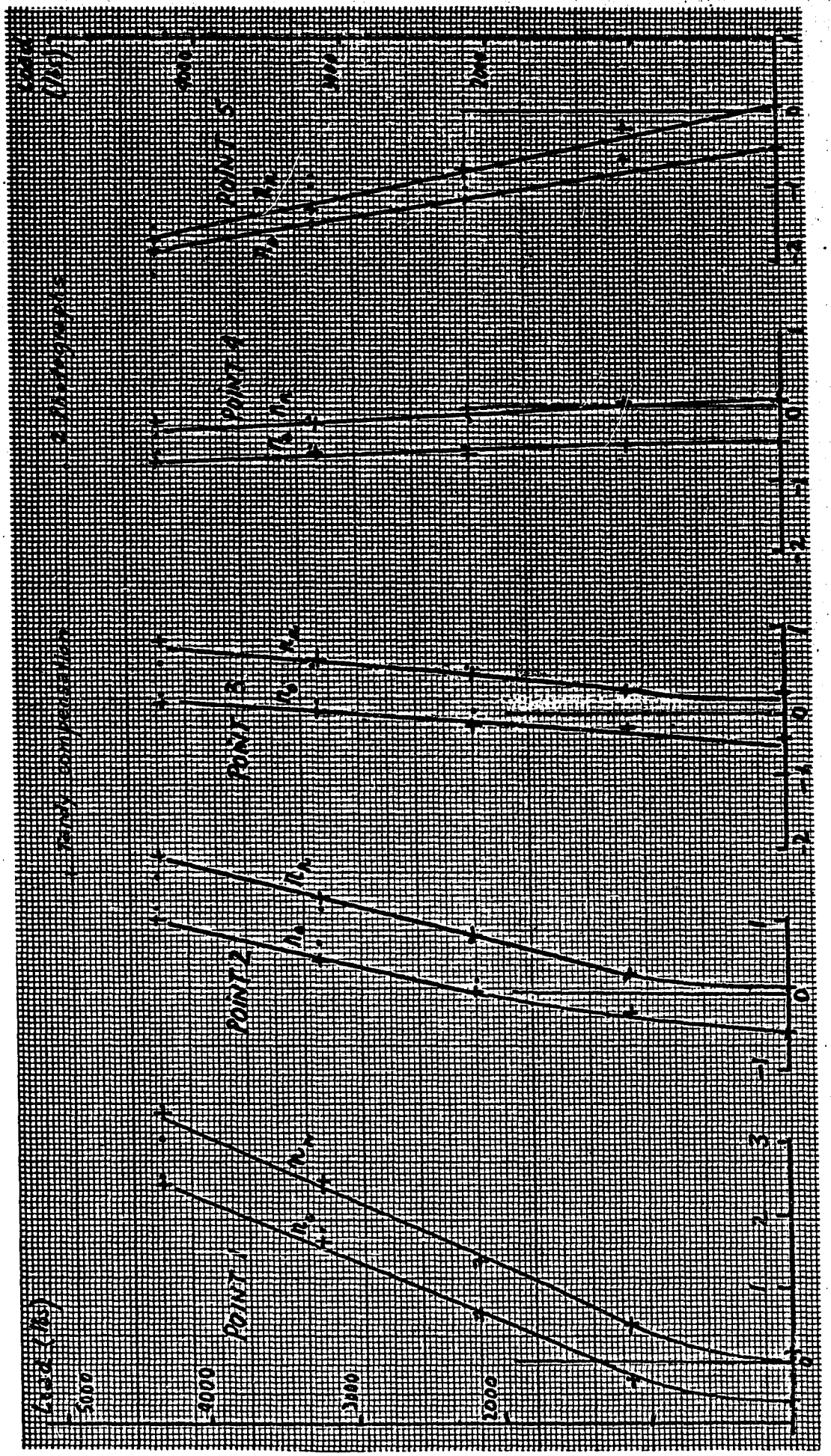

Fig. 3.57 Beam 2. Load-fringe order curves.

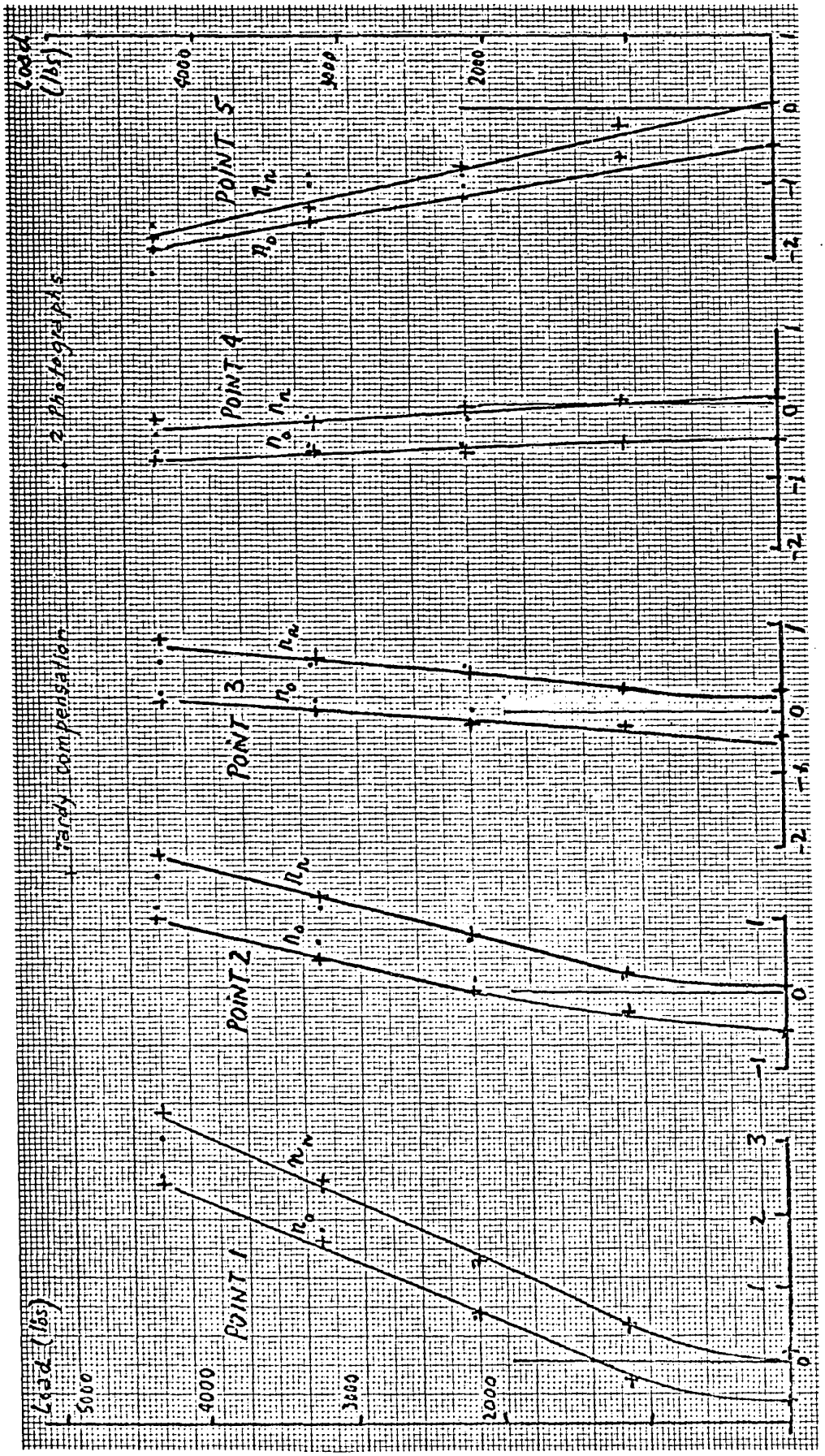

Fig. 3.57 Beam 2 . Load-fringe order curves.

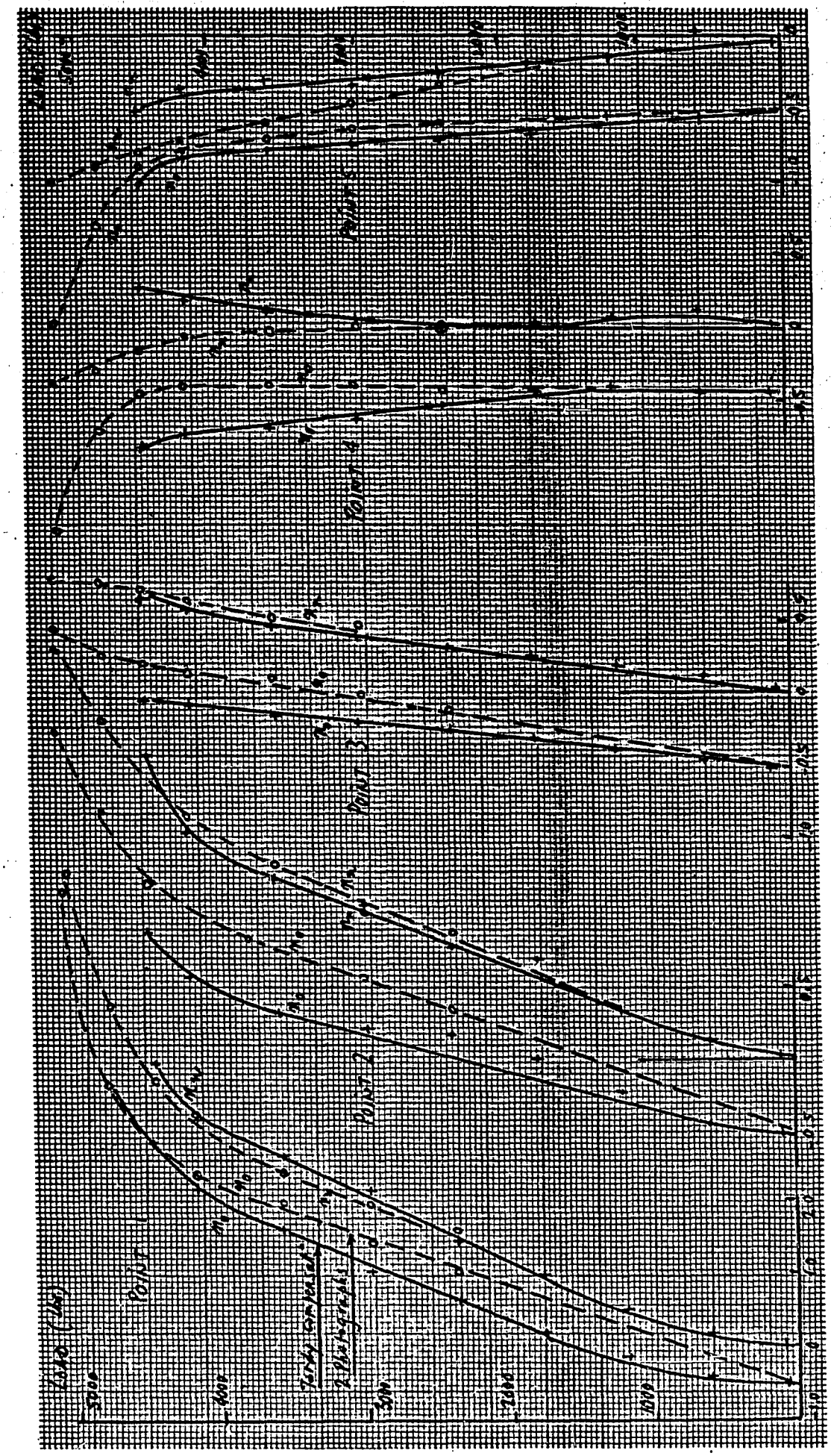

Fig. 3.58 Beam 3 . Load-fringe order curves.

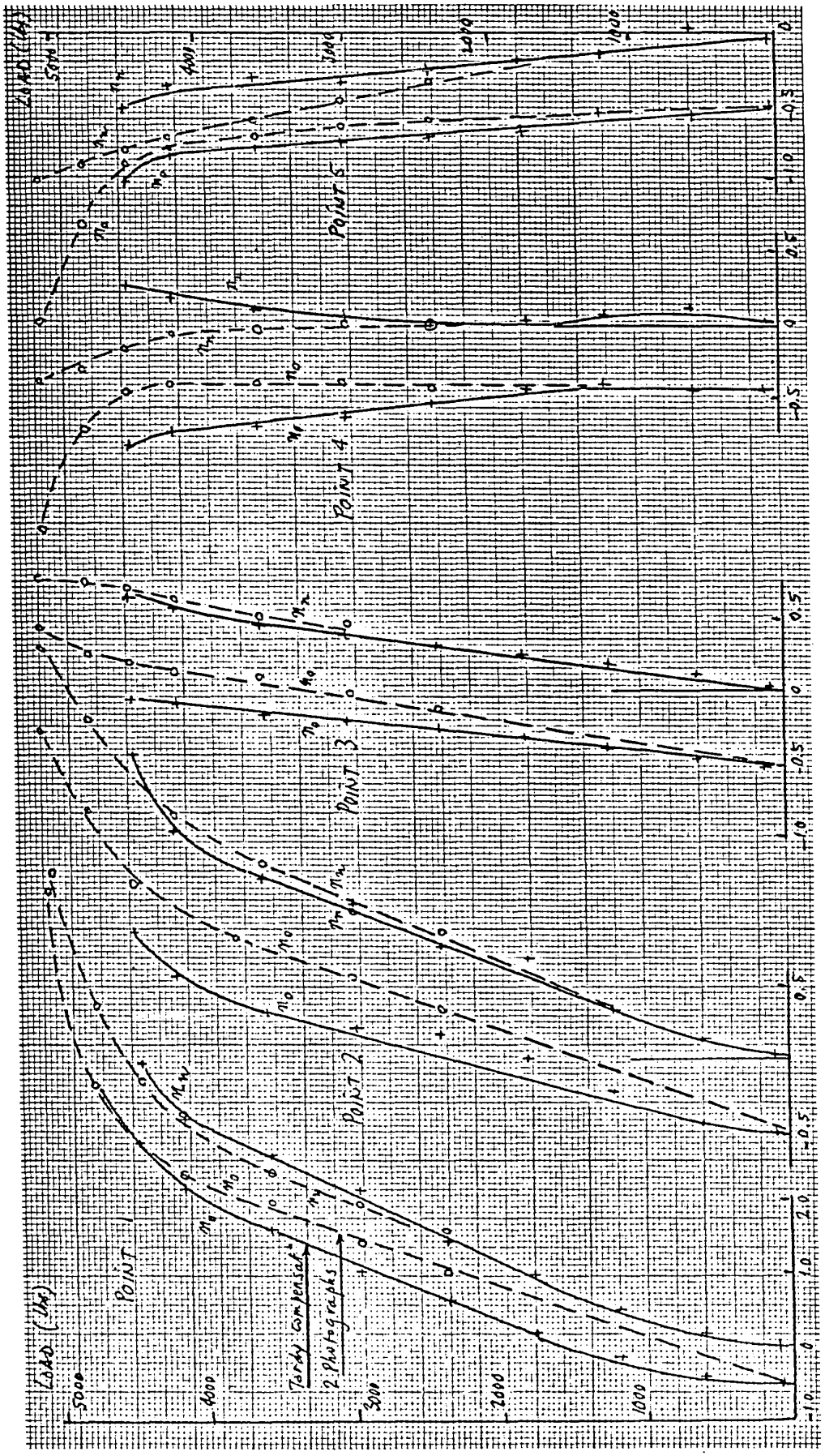

Fig. 3.58 Beam 3 . Load-fringe order curves.

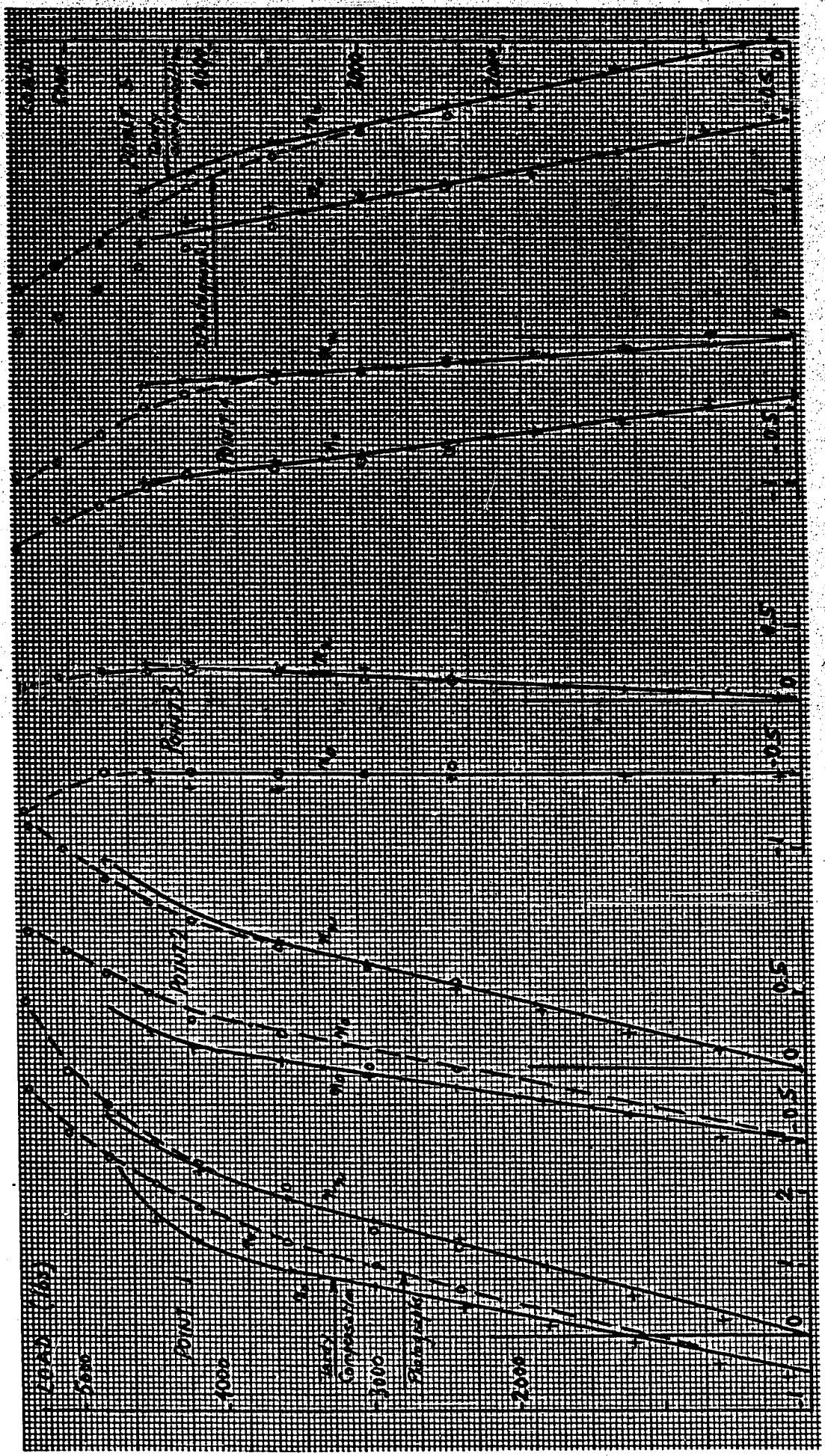

Fig. 3.59 Beam 4 - Load-fringe order curves.

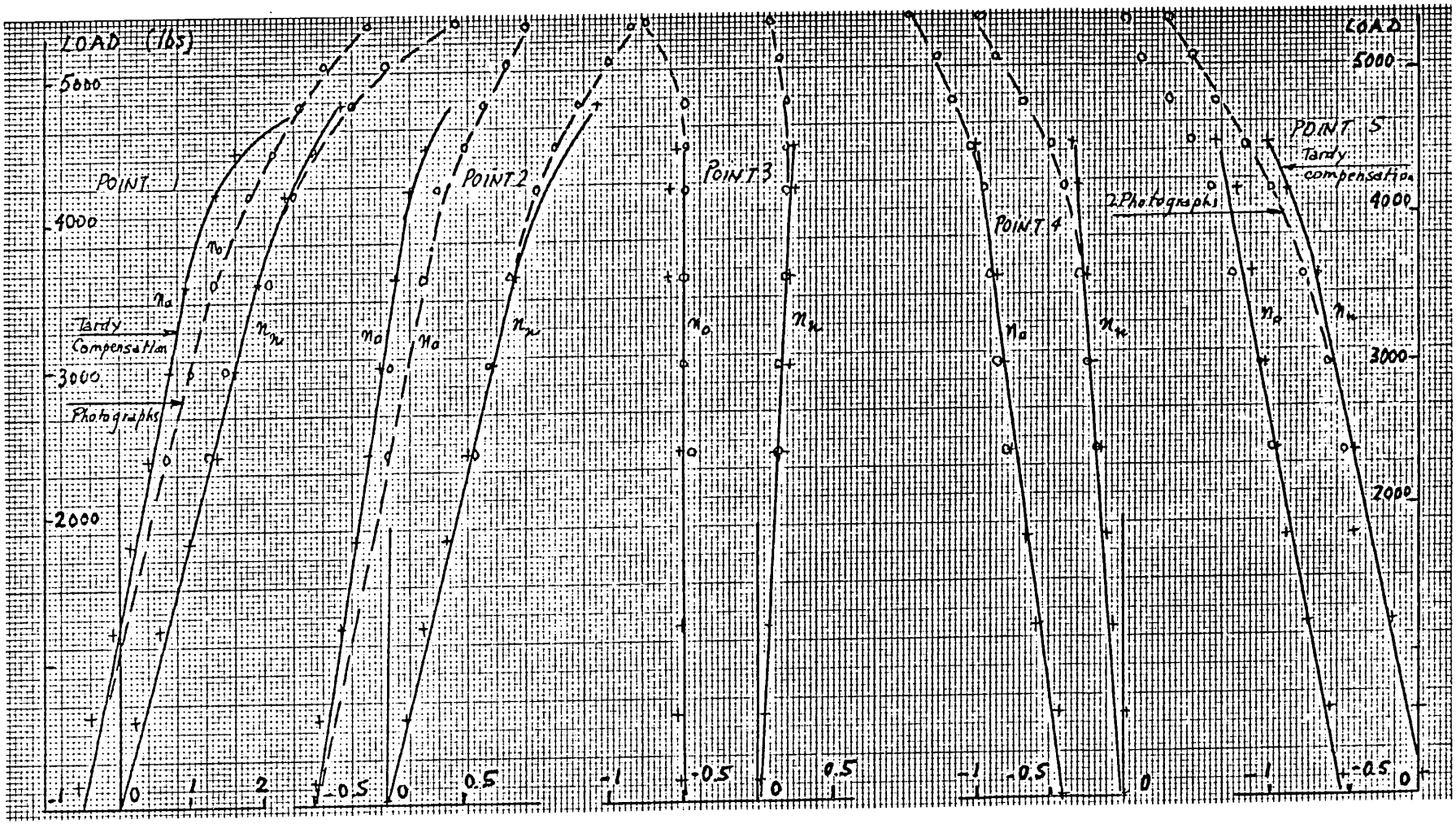

Fig. 3.59 Beam 4 - Load-fringe order curves.

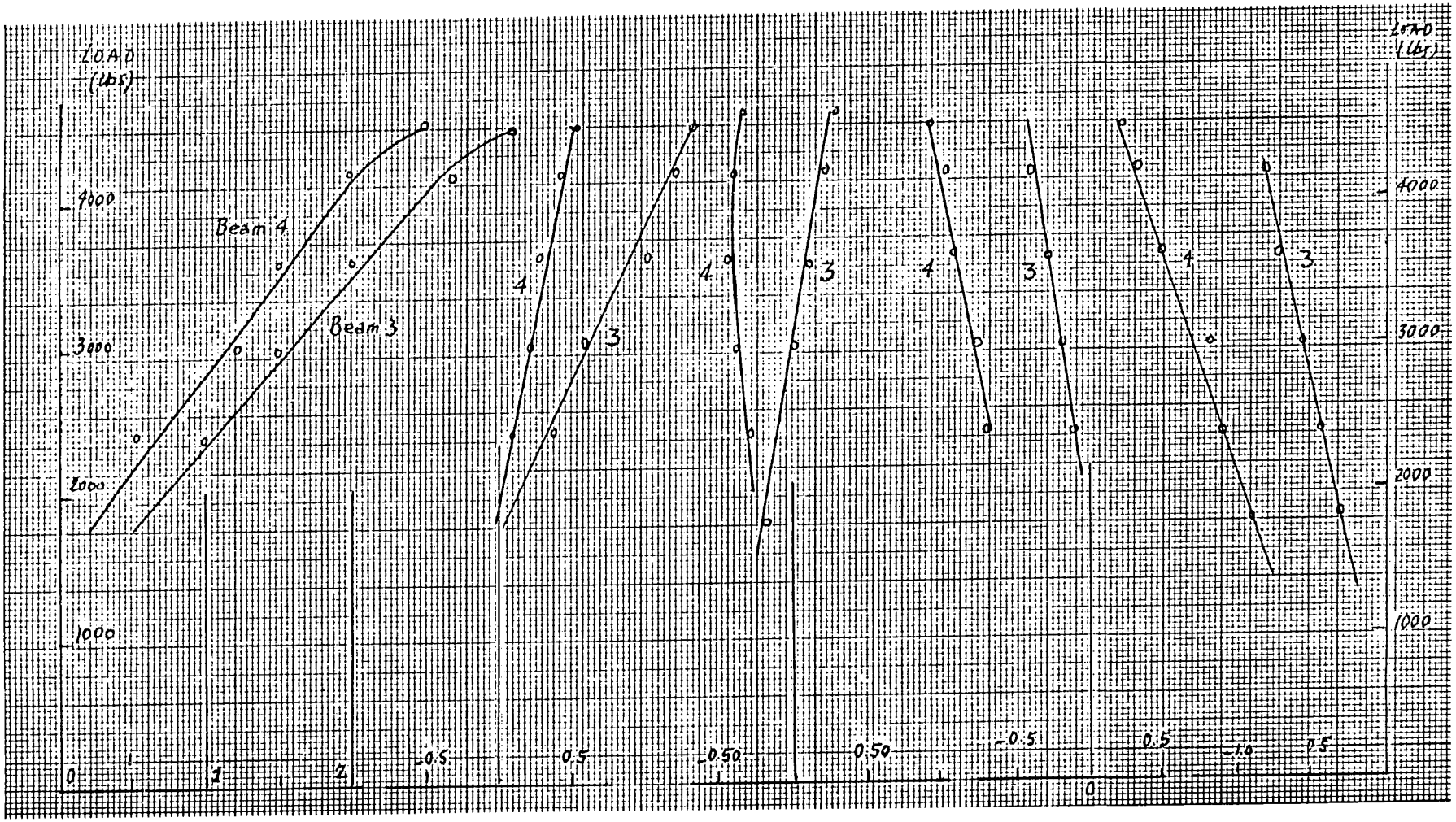

Fig. 3.60 Beams 3 and 4 . Load-fringe order curves in oblique incidence (30^{o}).

Chapter IV.

Conclusions and recommendations.

In the first two chapters, a summary of the background needed to carry the work has been given, with references.

A computer method for the complete determination of deflections and rotations of reinforced concrete beams up to failure has been developed, for beams of non uniform cross section.

In the third chapter, the experimental aims and procedures have been explained in detail.

The aims are twofold:

First, to test the validity of the deflections and rotations obtained from the computer calculations, and to check the assumptions made for the analysis of the beams.

Secondly, to examine the possibility of determining the strains at the surface of a microconcrete member, by means of the photostress technique, up to ultimate loads.

The first part of these objectives has been met with excellent accuracy.

Although only few measurements could be taken in the inelastic range of behaviour of the beams, the deflections observed have followed the theoretical curves very closely, proving the validity of the approach.

As far as the strains at the surface of the beams are concerned good correlation was established between direct measurements made with a Demec gauge and the calculated strains at the section of symmetry of the beams.

Photographs of the fringe patterns confirmed that the strains in the compressive zone were almost constant over the gauge length of the measurements, i.e. about 4 inches.

As regards the Photostress technique, the experiments have established beyond doubt the feasibility of obtaining the strain distribution at the surface of members.

The results obtained in axial compression were excellent.

In bending, the emphasis was placed on the approximation of the strains at five points of one cross section, by means of two techniques of measurement, and two procedures for the separation of the principal strains.

The techniques of measurement were:

a) a point by point observation in normal and oblique incidence, with goniometric compensation, and

b) the determination of the fringe orders from photographs taken through a larger oblique incidence attachment, built especially for the experiments.

The strains were derived from the two following procedures:

a) the solution of a system of two equations obtained from two readings in normal and oblique incidence, with proper alignment of the polariscope,

b) the solution of a system of three equations, obtained from the reading in normal incidence, and two in oblique incidence.

Although some scatter remained, emphasizing the difficulties inherent in photoelastic techniques, good progress was made during the experiments to reduce it. On the whole, good data were obtained, and the various procedures proved themselves to be quite reliable.

Clearly, point by point observation can only be used when creep of the beam is not an important factor.

However, it has been shown that good results can be obtained with only two or three photographs of a fringe pattern, thus greatly reducing the time needed.

This points the way to many further uses of the photostress technique in the field of structural concrete.

It had been hoped that such a simple procedure could be used to record the fringe pattern in the hinging region of the beams, up to ultimate.

The experiments have shown, however that the manipulation of the existing equipment was still too time consuming to permit the simultaneous recordings needed.

Progress in this direction could be achieved by the development of compact, automatic instruments that would bring three configurations of the optical system in the path of light, within fractions of a second, and be coupled with a movie camera.

The photographs obtained could then be projected on a screen, and analysed by an automatic scanning system containing a sensitive photo cell, and coupled to a digital computer.

The second part of the equipment exists, and is available commercially, the first part remains to be built.

REFERENCES

Chapter I.

1.1 L.G.Jaeger Cartesian Tensors in Engineering Science - Pergamon Press.

1.2 S. Timoshenko and J.N.Goodier: Theory of Elasticity - McGraw-Hill.

1.3 M.M.Frocht: Photoelasticity, Vol. I - Wiley.

1.4 M.M.Frocht: Photoelasticity, Vol. II - Wiley.

1.5 L.N.G.Filon: A Manual of Photoelasticity for Engineers - Cambridge University Press

1.6 A.W.Hendry: Elements of Experimental Stress Analysis - Pergamon Press.

1.7 A.W.Hendry: Photoelastic analysis - Pergamon Press.

1.8 H.T.Jessop and F.C.Harris: Photoelasticity Principles and Methods, Cleaver-Hume Press and Dover.

1.9 M.Hetenyi: Handbook of Experimental Stress Analysis - Wiley

1.10 F.Zandman: Photostress, Principles and Applications - The Budd Company.

1.11 F.Zandman: Basic Questions and Answers concerning the Photostress Technique - The Budd Company, Publication No. PS 5053, 1960.

1.12 P.Dantu: Etude des Contraintes dans les Milieux hétérogenes. Application au Béton-Laboratoire Central des Ponts et Chaussées, Paris - Publication no 57-6, 1957.

1.13 F.Zandman, et al: Reinforcing Effect of Birefringent Coatings - Proceedings of the Society for Experimental Stress Analysis (SESA), Vol XIX (1961).

1.14 R.M.Stephen and D.Priz: Application of Birefringent Coatings to the Study of Strains around Circular Intrusions in Mortar Prisms - Proceedings SESA, Vol XX.

1.15 D.Post: Photoelasticity - Manual on Experimental Stress Analysis - SESA (1965).

1.16 A.L.Carter: Obtaining Stress Maps from Photoelastic Data using a Digital Computer - Experimental Mechanics March 1968

1.17 Instruments Division of the Budd Company: Instruction manual for the Photostress large field meter and its accessories, Publication I - 02 - 2.

Chap.II References (continued).

2.1 A.H.Mattock, Rotational Capacity of hinging regions in reinforced concrete beams; Publication SP-12 of the American Concrete Institute. "Flexural mechanics of reinforced concrete."

2.2 J.D.Davies, Structural Concrete - Pergamon Press.

2.3 A.L.L.Baker, The Ultimate-Load Theory applied to the Design of Reinforced and Prestressed Concrete Frames - Concrete Publications Ltd., London.

2.4 R. Chambaud, Le Calcul du Béton armé a la Rupture-Eyrolles - Paris.

2.5 A.L.L.Baker and A.M.N.Amarakone, Inelastic hyperstatic frames analysis - Publication ACI SP 12.

2.6 Comité Européen du Béton, Recommendations for an International Code of Practice for Reinforced Concrete.

2.7 American Concrete Institute, Building Code Requirements for Reinforced Concrete (ACI 318 - 63).

2.8 E. Hognestad, Ultimate strength of reinforced Concrete in American Design Practice - Proceedings of a Symposium on the strength of Concrete Structures - London, May 1956.

2.9 E. Hognestad, N.W. Hanson and D. McHenry, Concrete Stress Distribution in Ultimate Strength Design, Proceedings of the American Concrete Institute, Vol. 52, December 1955.

2.10 A.H. Mattock, L.B. Kriz and E. Hognestad, Rectangular Concrete Stress Distribution in Ultimate Strength Design - Proceedings of the ACI, Vol. 57, February 1961.

2.11 E. Hognestad, Confirmation of Inelastic Stress Distribution in Concrete. Proceedings of the American Society of Civil Engineers, Vol. 83, No. ST 2, March 1957.

2.12 J.A. Blume, N.M. Newmark, L.C. Corning, Design of Multistorey Reinforced Concrete Buildings for Earthquake Motions - Portland Cement Association.

2.13 Ch. Massonnet and M. Save, Calcul Plastique des Constructions, Vol. I - Centre Belgo-Luxembourgeois d'Information de l'Acier.

2.14 J.M. Gere and W. Weaver Jr., Analysis of framed structures - Van Nostrand.

2.15 H.E.H. Roy and Mete A. Sozen, Ductility of Concrete, Publication ACI SP 12.

2.16 V.V. Bertero and C. Felippa, Discussion of [2.15].

2.17 J.H. Doyen, Non elastic analysis and Design of Reinforced Concrete Structures, M.I.T., 1965, M.Sc. Thesis.

2.18 N.G. Corley, Rotational Capacity of reinforced concrete beams; Journal of the American Society of Civil Engineers, Structural Division, October, 1966.

2.19 P.R. Barnard, The collapse of Reinforced Concrete Beams - Publication ACI SP 12 .

2.20 E. Burnett, Flexural Rigidity, Curvature and Rotation and their significance in Reinforced Concrete, Magazine of Concrete Research, Vol. 16, No. 47, June 1964 .

2.21 Herbert A. Sawyer, Jr., Design of Concrete Frames for two Failure Stages - Publication ACI SP 12 .

2.22 K. Billig, Structural Concrete - McMillan.

APPENDIX 1

```
//CONTBEAM    JOB  (F119,000,005,040,500,01),'.J.C.MAMET.

FORTRAN IV G LEVEL 1, MOD 2            MAIN                DATE = 68225        21/29/49

 0001              WRITE (6,101)
 0002          101 FORMAT (1H1,'ANALYSIS OF CONTINUOUS BEAM'//' STRUCTURE DATA   M N
                  1NR NRJ E')
 0003              ODIMENSION L(24),IZ(24),RL(50),CRL(50),A(50),AML(24,4),AE(50),
                   1SM(4,4),S(50,50),D(50),AR(50),AC(50),AM(24,4)
 0004              REAL L,IZ,A,AML,AE,AC,SM,S,D,AR,AM,E
 0005              INTEGER I,J,JE,J1,J2,K,KE,K1,K2,M,N,NJ,NR,NRJ,NLJ,NLM,RL,CRL,JE1
 0006         1000 READ (5,102) M,NR,NRJ,E
 0007          102 FORMAT (3I8,F14.1)
 0008              NJ=M+1
 0009              N = 2*NJ-NR
 0010              WRITE (6,103) M,N,NR,NRJ,E
 0011          103 FORMAT (1H ,//'      M       N       NR      NRJ          E'//4I8,
                  1F14.0)
 0012              WRITE (6,104)
 0013          104 FORMAT (1H ,//' MEMBER DESIGNATIONS LENGTHSAND MOMENTS OF INERTIA'
                  1//' MEMBER          L          IZ')
 0014              READ (5,105) ((I,(L(I),IZ(I))),I=1,M)
 0015          105 FORMAT (I8,2F10.3)
 0016              WRITE (6,106) ((I ,(L(I),IZ(I))),I=1,M)
 0017          106 FORMAT (1H ,I7,F10.1,F12.3)
 0018              NJ2=2*NJ
 0019              DO 301 K=1,NJ2
 0020              CRL(K) = 0
 0021          301 RL(K) = 0
 0022              WRITE (6,107)
 0023          107 FORMAT (1H ,//' JOINT RESTRAINTS'//' JOINT YRESTRAINT ZRESTRAINT')
 0024              DO 315 J=1,NRJ
```

```
0025                READ (5,108) K,RL(2*K-1),RL(2*K)
0026              108 FORMAT (3I8)
0027              315 WRITE (6,109) K,RL(2*K-1),RL(2*K)
0028              109 FORMAT (1H ,I3,I9,I12)
0029                CRL(1)=RL(1)
0030                DO 307 K=2,NJ2
0031                CRL(K)=CRL(K-1)+RL(K)
0032              307 CONTINUE
                  C
                  C     STRUCTURE STIFFNESS MATRIX
                  C     REARRANGEMENT OF INDICES
                  C
0033                M2P2=2*M +2
0034                DO 302 L1 = 1,M2P2
0035                DO 302 L2 = 1,M2P2
0036              302 S(L1,L2) = 0.0
0037                DO 220 I=1,M
0038                J1 = 2*I-1
0039                J2 = 2*I
0040                K1 = 2*I+1
0041                K2 = 2*I + 2
0042                SCM1=(4.0*E*IZ(I))/L(I)
0043                SCM2=(1.5*SCM1)/L(I)
0044                SCM3=(2.0*SCM2)/L(I)
0045                IF(RL(J1))202,201,202
0046              201 J1=J1-CRL(J1)
```

```
0047                GO TO 203
0048           202  J1=N+CRL(J1)
0049           203  IF(RL(J2))205,204,205
0050           204  J2=J2-CRL(J2)
0051                GO TO 206
0052           205  J2=N+CRL(J2)
0053           206  IF(RL(K1))208,207,208
0054           207  K1=K1-CRL(K1)
0055                GO TO 209
0056           208  K1=N+CRL(K1)
0057           209  IF(RL(K2))211,210,211
0058           210  K2=K2-CRL(K2)
0059                GO TO 212
0060           211  K2=N+CRL(K2)
               C
               C    MEMBER STIFFNESS MATRIX
               C
0061           212  SM(3,3)=SCM3
0062                SM(1,1)=SM(3,3)
0063                SM(3,1)=-SCM3
0064                SM(1,3)=SM(3,1)
0065                SM(4,1)=SCM2
0066                SM(1,4)=SM(4,1)
0067                SM(2,1)=SM(1,4)
0068                SM(1,2)=SM(2,1)
0069                SM(4,3)=-SCM2
0070                SM(3,4)=SM(4,3)
0071                SM(3,2)=SM(3,4)
```

```
0072                SM(2,3)=SM(3,2)
0073                SM(4,2)=SCM1/2.0
0074                SM(2,4)=SM(4,2)
0075                SM(4,4)=SCM1
0076                SM(2,2)=SM(4,4)
                C
                C       STIFFNESS MATRIX
                C
0077                IF(RL(2*I-1))214,213,214
0078              213 S(J1,J1)=S(J1,J1)+SM(1,1)
0079                S(J2,J1)=S(J2,J1)+SM(2,1)
0080                S(K1,J1)=SM(3,1)
0081                S(K2,J1)=SM(4,1)
0082              214 IF(RL(2*I))216,215,216
0083              215 S(J1,J2)=S(J1,J2)+SM(1,2)
0084                S(J2,J2)=S(J2,J2)+SM(2,2)
0085                S(K1,J2)=SM(3,2)
0086                S(K2,J2)=SM(4,2)
0087              216 IF(RL(2*I+1))218,217,218
0088              217 S(J1,K1)=SM(1,3)
0089                S(J2,K1)=SM(2,3)
0090                S(K1,K1)=S(K1,K1)+SM(3,3)
0091                S(K2,K1)=S(K2,K1)+SM(4,3)
0092              218 IF(RL(2*I+2))220,219,220
0093              219 S(J1,K2)=SM(1,4)
0094                S(J2,K2)=SM(2,4)
```

```
0095            S(K1,K2)=S(K1,K2)+SM(3,4)
0096            S(K2,K2)=S(K2,K2)+SM(4,4)
0097          220 CONTINUE
              C
              C     INVERSION OF STIFFNESS MATRIX
              C
0098            CALL DCOMP (N,S)
0099            CALL INVERT (N,S)
0100            WRITE (6,114)
0101          114 FORMAT (1H ,//' LOAD DATA'//'       NLJ     NLM')
0102            READ (5,115) NLJ,NLM
0103          115 FORMAT (2I8)
0104            WRITE (6,116) NLJ,NLM
0105          116 FORMAT (1H ,I9,I8)
0106            DO 303 K=1,M2P2
0107            A(K)=0.0
0108            AC(K) = 0.0
0109          303 AE(K) = 0.0
0110            DO 401 I=1,M
0111            DO 401 K=1,4
0112            AML(I,K) =0.0
0113          401 CONTINUE
0114            WRITE (6,118)
0115          118 FORMAT (1H ,//' ACTIONS APPLIED AT JOINTS'//'     JOINT   Y ACTION
                 1     Z ACTION ')
0116            IF (NLJ)221,222,221
0117          221 DO 310 J=1,NLJ
0118            READ (5,117) K,(A(2*K-1),A(2*K))
```

```
0119          117 FORMAT (I8,2F12.2)
0120          310 WRITE (6,316) K,(A(2*K-1),A(2*K))
0121          316 FORMAT (1H ,16,2F14.3)
0122          222 IF(NLM) 308,225,308
0123          308 WRITE (6,119)
0124          119 FORMAT (1H ,//' ACTIONS AT ENDS OF RESTRAINED MEMBERS DUE TO LOAD'
                 1//' MEMBER    AML1       AML2       AML3       AML4')
0125              DO 309 J=1,NLM
0126              READ (5,120) I,(AML(I,K),K=1,4)
0127          120 FORMAT (I8,F11.3,3F14.3)
0128          309 WRITE (6,121) I,(AML(I,K),K=1,4)
0129          121 FORMAT (I6,F11.3,3F10.3)
              C
              C     CONSTRUCTION OF VECTORS ASSOCIATED WITH LOADS
              C
0130              IF (NLM) 223,225,223
0131          223 DO 224 I=1,M
0132              AE(2*I-1)=AE(2*I-1)-AML(I,1)
0133              AE(2*I)=AE(2*I)-AML(I,2)
0134              AE(2*I+1)=AE(2*I+1)-AML(I,3)
0135          224 AE(2*I+2)=AE(2*I+2)-AML(I,4)
              C
              C     COMBINED JOINT LOADS REARRANGEMENT OF LOAD VECTOR
              C
0136          225 NPNR= N+NR
0137              DO 314 J=1,NPNR
```

```
0138                IF(RL(J))226,227,226
0139              226 K=N+CRL(J)
0140                GO TO 228
0141              227 K=J-CRL(J)
0142              228 AC(K)=A(J)+AE(J)
0143              314 CONTINUE
                  C
                  C     CALCULATION AND OUTPUT OF RESULTS
                  C     JOINT DISPLACEMENTS AND SUPPORT REACTIONS
                  C
0144                DO 304 J=1,M2P2
0145              304 D(J) =0.0
0146                DO 230 J=1,N
0147                DO 229 K=1,N
0148              229 D(J)=D(J)+S(J,K)*AC(K)
0149              230 CONTINUE
0150                DO 305 K=1,M2P2
0151              305 AR(K) = 0.0
0152                NP1=N+1
0153                DO 231 K=NP1,NPNR
0154                AR(K)=-AC(K)
0155                DO 317 J=1,N
0156              317 AR(K)=AR(K)+S(K,J)*D(J)
0157              231 CONTINUE
0158                J=N+1
0159                NPNRP1 = NPNR + 1
0160                DO 234 JF = 1,NPNR
0161                JE = NPNRP1 - JF
```

```
0162            IF(RL(JE))233,232,233
0163        232 J=J-1
0164            D(JE)=D(J)
0165            GO TO 234
0166        233 D(JE)=0.0
0167        234 CONTINUE
0168            K=N
0169            DO 318 KE=1,NPNR
0170            IF(RL(KE)-1.0) 236,235,236
0171        235 K=K+1
0172            AR(KE)=AR(K)
0173            GO TO 318
0174        236 AR(KE)=0.0
0175        318 CONTINUE
0176        237 WRITE (6,125)
0177        125 FORMAT (1H ,//' JOINT DISPLACEMENTS AND SUPPORT REACTIONS'//' JOIN
                1T    YDISPL      ZDISPL      YREACT      ZREACT ')
0178            DO 312 JE=2,NJ2,2
0179            JE1=JE/2
0180        312 WRITE (6,126) JE1,D(JE-1),D(JE),AR(JE-1),AR(JE)
0181        126 FORMAT (1H ,I5,E12.4,E11.4,2F11.3)
0182            DO 238 I=1,M
0183            J1=2*I-1
0184            J2=2*I
0185            K1=2*I+1
0186            K2=2*I+2
```

```
0187                SCM1=(4.0*E*IZ(I))/L(I)
0188                SCM2=(1.5*SCM1)/L(I)
0189                SCM3=(2.0*SCM2)/L(I)
0190                DO 306 J=1,4
0191             306 AM(I,J) = 0.0
0192                AM(I,1)=AML(I,1)+SCM3* (D(J1)-D(K1))+SCM2*(D(J2)+D(K2))
0193                AM(I,2)=AML(I,2)+SCM2*(D(J1)-D(K1))+SCM1*(D(J2)+ D(K2)/2.0)
0194                AM(I,3)=AML(I,3)-SCM3*(D(J1)-D(K1))-SCM2*(D(J2)+D(K2))
0195                AM(I,4)=AML(I,4) + SCM2*(D(J1)-D(K1)) + SCM1*(D(J2)/2.0+D(K2))
0196             238 CONTINUE
0197                GO TO 1000
0198            1001 END
```

TOTAL MEMORY REQUIREMENTS 00487A BYTES

```
FORTRAN IV G LEVEL 1, MOD 2            DCOMP            DATE = 68225      21/29/49

0001                SUBROUTINE DCOMP (N,X)
0002                REAL X(50,50),SUM,TEMP
0003                INTEGER I,J,K,KI
0004                DO 1 I=1,N
0005                DO 1 J=I,N
0006                SUM=X(I,J)
0007                KI=I-1
0008                IF(I-1)10,9,10
0009             10 DO 3 K=1,KI
0010              3 SUM = SUM - X(K,I)*X(K,J)
0011              9 IF(J-I)4,11,4
0012             11 IF(SUM-0.0)5,5,2
0013              5 WRITE (6,6)
0014              6 FORMAT (34H THIS SUBROUTINE HAS NEGATIVE SUM )
0015                GO TO 7
0016              2 TEMP= 1./SQRT(SUM)
0017                X(I,J)=TEMP
0018                GO TO 1
0019              4 X(I,J)=SUM*TEMP
0020              1 CONTINUE
0021              7 RETURN
0022                END

 TOTAL MEMORY REQUIREMENTS 00031C BYTES
```

```
FORTRAN IV G LEVEL 1, MOD 2            INVERT          DATE = 68225        21/29/49

0001                  SUBROUTINE INVERT (N,X)
0002                  REAL X(50,50),SUM
0003                  INTEGER I,J,K,I1,J1,K1
0004                  I1=N-1
0005                  DO 1 I=1,I1
0006                  J1=I+1
0007                  DO 1 J=J1,N
0008                  SUM=0.0
0009                  K1=J-1
0010                  DO 2 K=I,K1
0011                2 SUM=SUM - X(K,I)*X(K,J)
0012                1 X(J,I)=X(J,J)*SUM
0013                  DO 3 I=1,N
0014                  DO 3 J=I,N
0015                  SUM=0.0
0016                  DO 4 K=J,N
0017                4 SUM=SUM +X(K,I)*X(K,J)
0018                  X(I,J)= SUM
0019                3 X(J,I)=SUM
0020                  RETURN
0021                  END

 TOTAL MEMORY REQUIREMENTS 000392 BYTES
```

M	N	NR	NRJ	E
11	22	2	2	3100.

MEMBER DESIGNATIONS LENGTHSAND MOMENTS OF INERTIA

MEMBER	L	IZ
1	13.0	17.9
2	2.0	17.7
3	2.0	15.9
4	2.0	13.5
5	2.0	12.0
6	2.0	10.5
7	2.0	12.0
8	2.0	13.5
9	2.0	15.9
10	2.0	17.7
11	13.0	17.9

JOINT RESTRAINTS

JOINT	YRESTRAINT	ZRESTRAINT
1	1	0
12	1	0

LOAD DATA

NLJ	NLM
2	0

ACTIONS APPLIED AT JOINTS

JOINT	Y ACTION	Z ACTION
2	-2.250	0.0
11	-2.250	0.0

JOINT DISPLACEMENTS AND SUPPORT REACTIONS

JOINT	YDISPL	ZDISPL	YREACT	ZREACT
1	0.0	-0.9397E-02	2.220	0.0
2	-0.1075E 00	-0.6016E-02	0.0	0.0
3	-0.1185E 00	-0.4963E-02	0.0	0.0
4	-0.1272E 00	-0.3796E-02	0.0	0.0
5	-0.1335E 00	-0.2422E-02	0.0	0.0
6	-0.1368E 00	-0.8842E-03	0.0	0.0
7	-0.1368E 00	0.8806E-03	0.0	0.0
8	-0.1335E 00	0.2419E-02	0.0	0.0
9	-0.1273E 00	0.3794E-02	0.0	0.0
10	-0.1185E 00	0.4961E-02	0.0	0.0
11	-0.1075E 00	0.6015E-02	0.0	0.0
12	0.0	0.9400E-02	2.222	0.0

APPENDIX 2

Beam 1 - Load 5500 lbs. normal incidence.

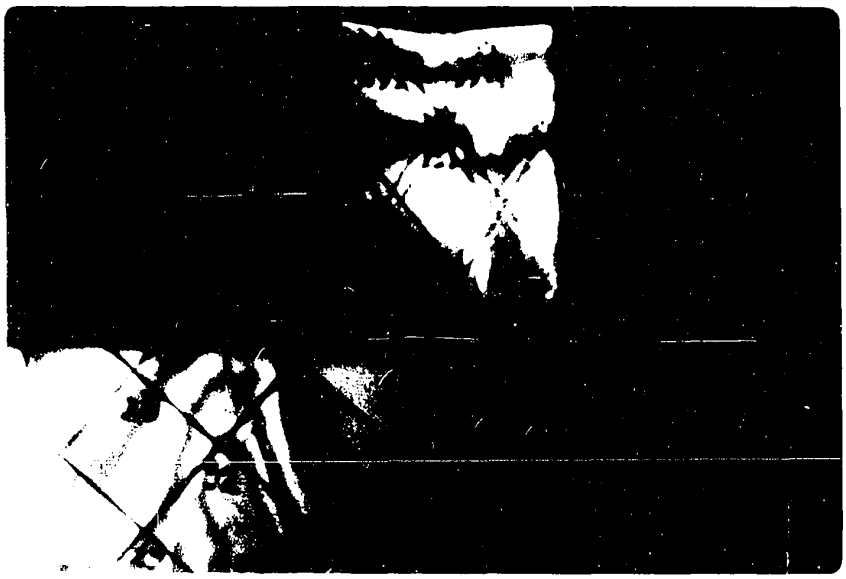

Beam 1 - Load 4100 lbs. oblique incidence 45^{o}.

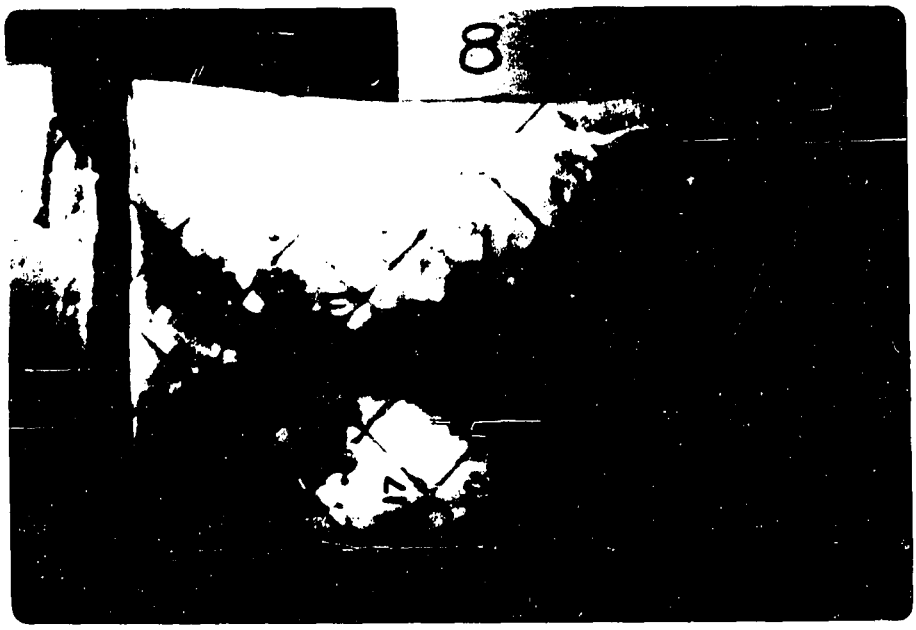

Beam 3 - 1200 lbs. Normal incidence.

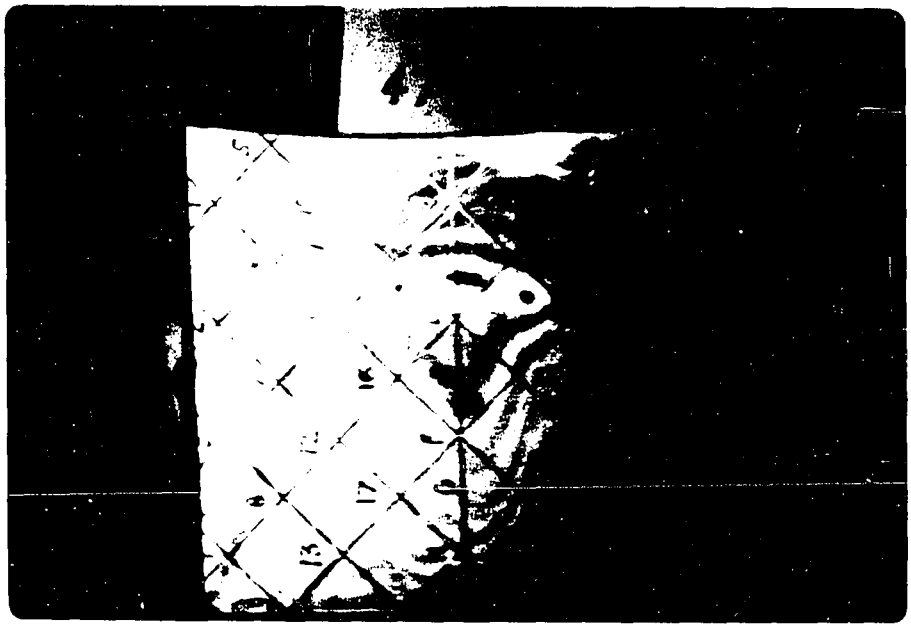

Beam 3 - 5100 lbs. Normal incidence.

Beam 3 - 5230 lbs. (ultimate).

Beam 4 - 5260 lbs. (ultimate).

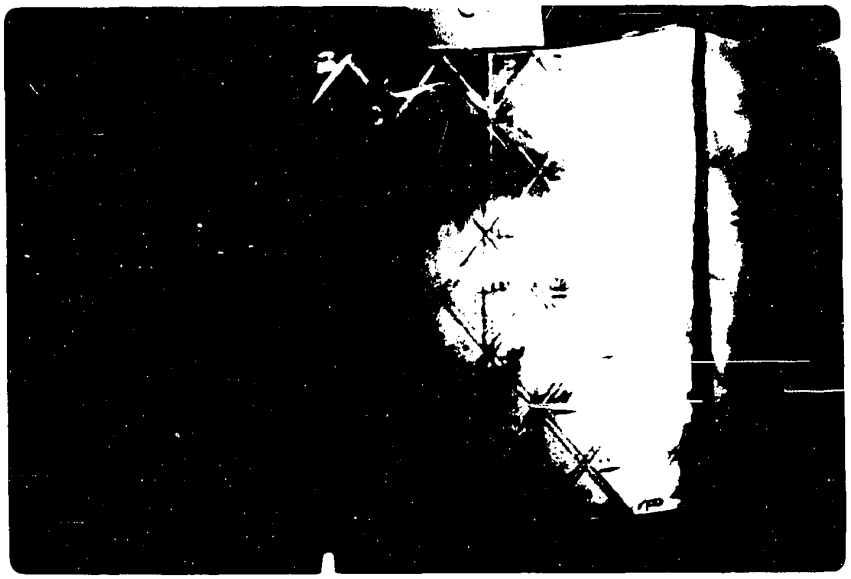

Beam 3 - 2400 lbs. oblique incidence 30°.

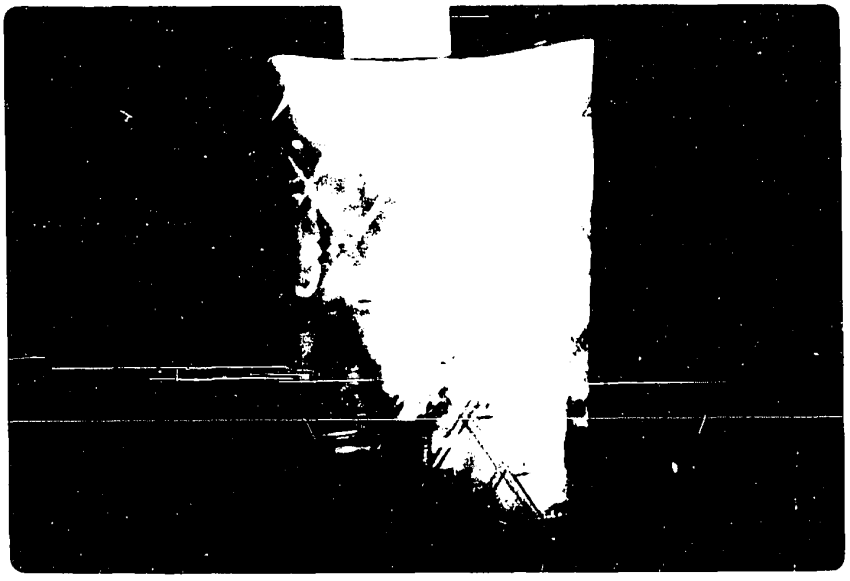

Beam 3 - 2400 lbs. oblique incidence 45°

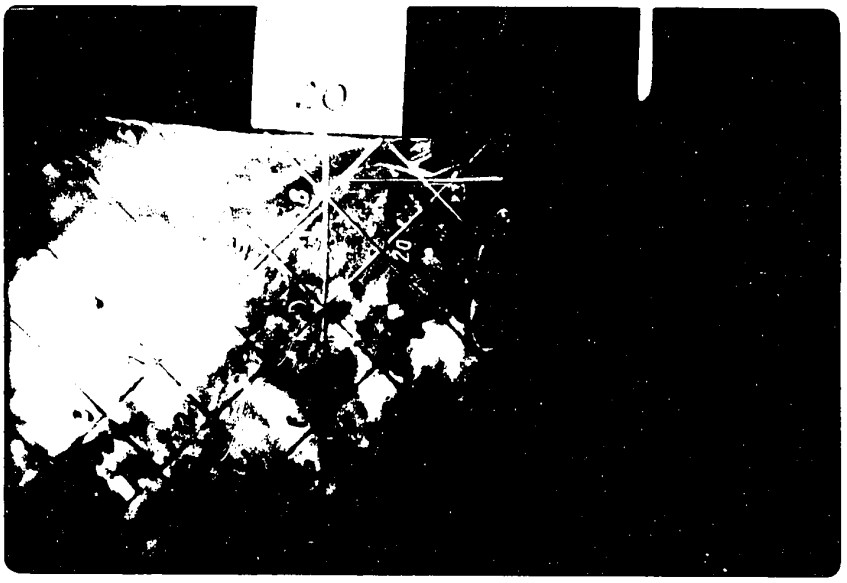

Beam 3 - 2400 lbs. isoclinic + 15°.

Beam 3 - 2400 lbs. isoclinic - 15°.